Understanding and tailoring laser ablation processes for thin film and nanostructure growth
with in situ diagnostics

David B. Geohegan [1]
Research Professor
[1]Dept. of Materials Science and Engineering, University of Tennessee, Knoxville, TN, USA

featuring work over the years performed with ORNL staff and UTK faculty

Alex A. Puretzky, Chris M. Rouleau, Sumner B. Harris,
Gerd Duscher[1], Mina Yoon, Gyula Eres, Kai Xiao
Center for Nanophase Materials Sciences, Oak Ridge National Laboratory, Oak Ridge, TN, USA

And talented students and postdocs, now all over the world

Masoud Mahjouri-Samani (Auburn Univ.,USA)
Yu-Chuan Lin (NYCU-Taiwan)
Chenze Liu (Georgia Tech, USA)
Yiling Yu (Wuhan U., – Physics, China)
Henrik Schittenhelm (Bosch, Germany**)**

SLIMS 24   San Servolo

2

Oak Ridge
National Laboratory

University of
Tennessee - Knoxville

Tennessee

SLIMS 24 San Servolo

3

Tennessee — The Volunteer State — Welcomes You

ELVIS

COUNTRY MUSIC HALL OF FAME AND MUSEUM NASHVILLE — HONOR THY MUSIC

KENTUCKY — VIRGINIA — Norfolk — TENNESSEE — NORTH CAROLINA — Raleigh — Knoxville — Charlotte
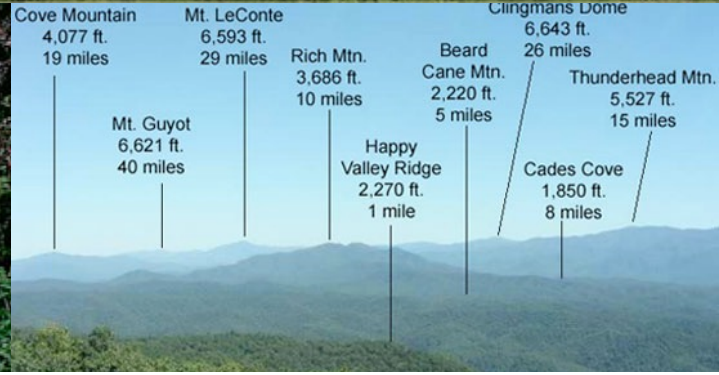
OAK RIDGE National Laboratory

UT THE UNIVERSITY of TENNESSEE
Knoxville, Chattanooga, Martin, Tullahoma, Memphis

Knoxville
area pop. ~ 800,000

Great Smoky Mountains National Park

SLIMS 24   San Servolo

Cove Mountain 4,077 ft. 19 miles
Mt. LeConte 6,593 ft. 29 miles
Rich Mtn. 3,686 ft. 10 miles
Clingmans Dome 6,643 ft. 26 miles
Beard Cane Mtn. 2,220 ft. 5 miles
Thunderhead Mtn. 5,527 ft. 15 miles
Mt. Guyot 6,621 ft. 40 miles
Happy Valley Ridge 2,270 ft. 1 mile
Cades Cove 1,850 ft. 8 miles

The Center for Nanophase Materials Sciences (CNMS) is a national user facility with a mission to advance nanoscience

About CNMS:

cnms.ornl.gov

- **Free access to laboratories, equipment and expertise if you agree to publish**

- **Simple 2-page proposal**

- **Two calls per year: early May and mid-October**

- **Joint proposals with neutron sources (SNS, HFIR)**

- **Rapid access proposals also.**

Research areas:

- **Synthesis –** 2D materials, nanotubes, polymers,

- **Nanofabrication –** direct-write, microfluidics, cleanroom

- **Advanced Microscopy –** AFM, STM, aberration-corrected TEM/STEM, atom-probe tomography

- **Functional Characterization –** laser spectroscopy, transport, magnetism, electromechanics

- **Theory and Modeling –** including gateway to leadership-class high performance computing
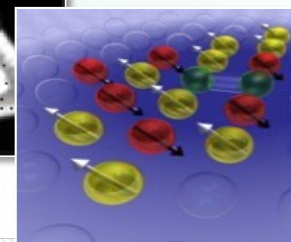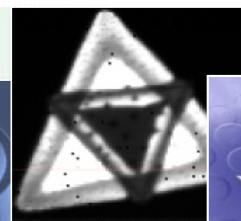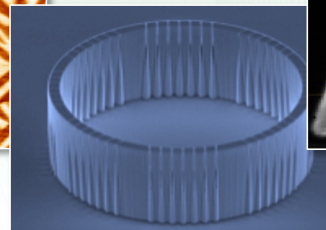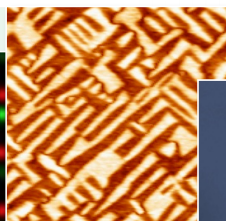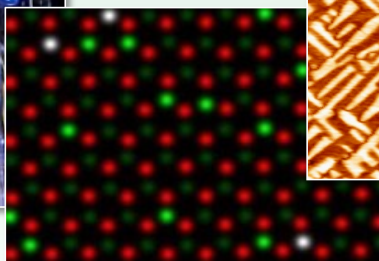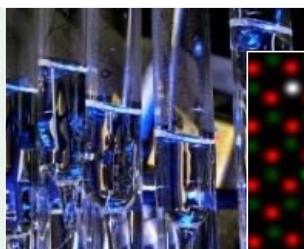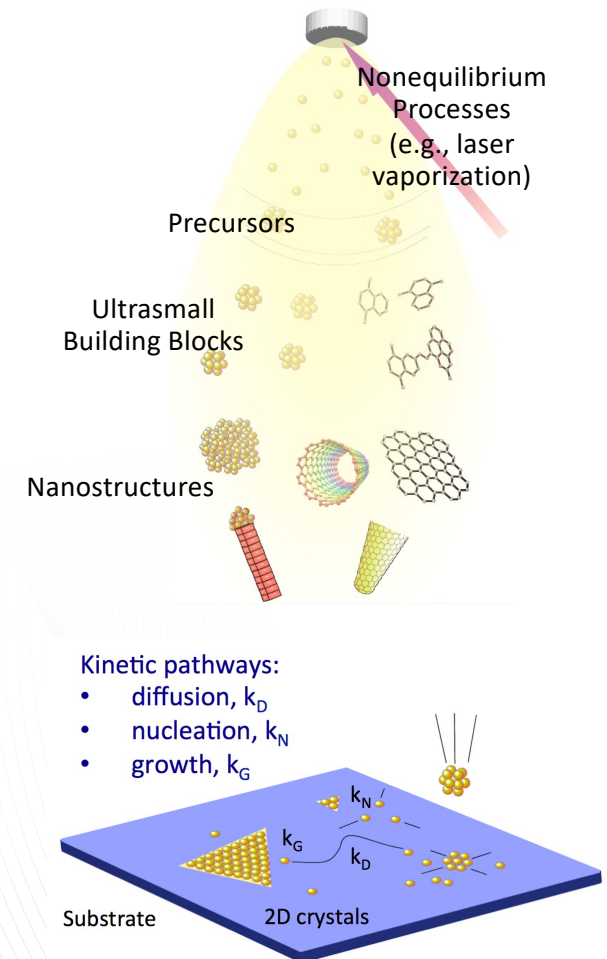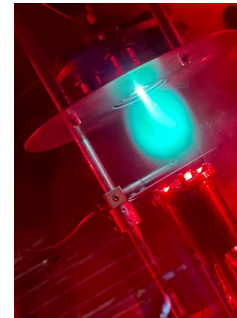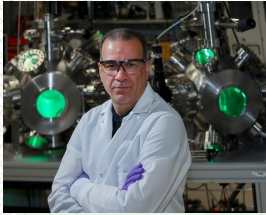
CNMS is a Nanoscale Science Research Center supported by the U.S. Department of Energy, Office of Science, Scientific User Facilities Division

Outline – Laser synthesis of nanomaterials and *in situ* diagnostics

- **Unique aspects of laser ablation for synthesis**
  - **Kinetic energy** – unique range, how to tune
  - Different '**building blocks**'
  - **Confinement** in time and space

- **Some synthesis principles**
  - Ostwald's rule of stages – metastable states
  - Crystallization by particle attachment – 'sintering'

- **Materials**
  - Gas phase synthesis of nanoparticles, tubes, horns.
  - Films to precision synthesis of atomically thin 2D materials

- **In situ diagnostics**
  - Simple ion probe, optical spectroscopy, imaging
  - Spatio-temporal, remote
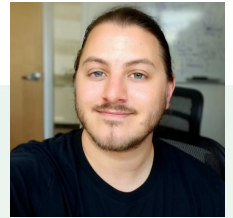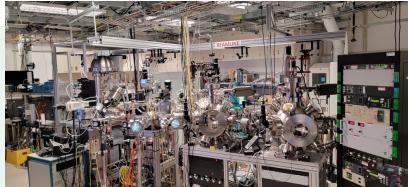 - Combined with automated synthesis for AI/ML

Nonequilibrium Processes (e.g., laser vaporization)

Precursors

Ultrasmall Building Blocks

Nanostructures

Kinetic pathways:
- diffusion, k_D
- nucleation, k_N
- growth, k_G
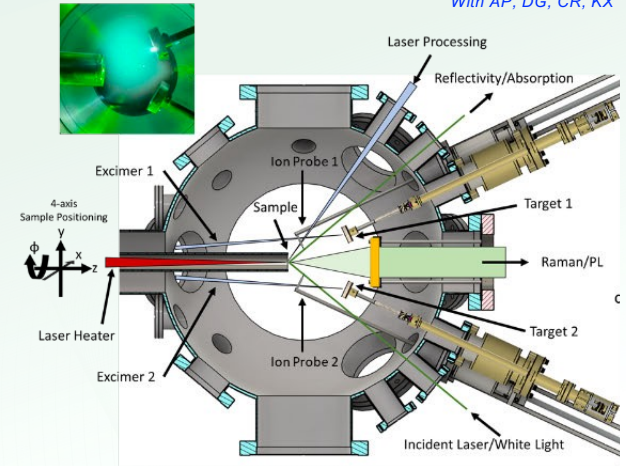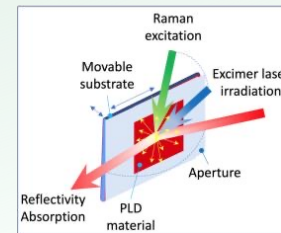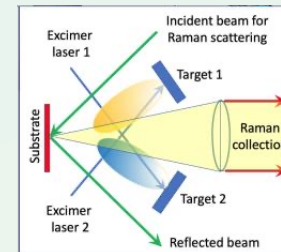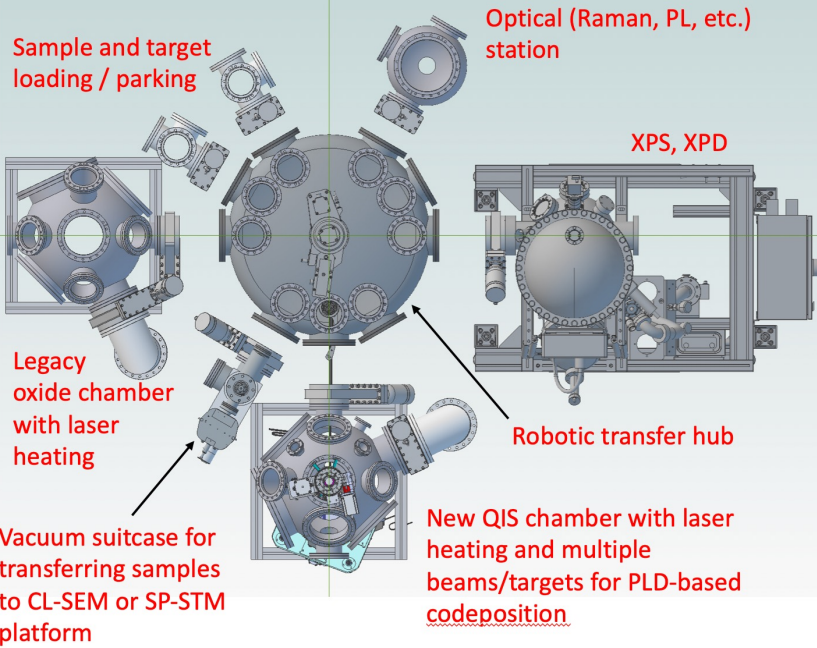
k_N

k_G

k_D

Substrate   2D crystals

New PLD instruments at CNMS/ORNL

Rapid, AI-guided PLD platform for Rapid Prototyping of Novel Materials for QIS

Chris Rouleau

In situ diagnostic PLD Platform to understand growth mechanisms

Sumner Harris

With AP, DG, CR, KX

Sample and target loading / parking

Optical (Raman, PL, etc.) station

XPS, XPD

Legacy oxide chamber with laser heating

Robotic transfer hub

Vacuum suitcase for transferring samples to CL-SEM or SP-STM platform

New QIS chamber with laser heating and multiple beams/targets for PLD-based codeposition

Substrate

In situ Raman, PL, reflectivity ~ deposition rate, structure, 'quality'

Plasma

Gated imaging and spectroscopy, ion probe ~ species, flux, kinetic energy

User instrument at the CNMS
- *Automation with AI and ML learning*

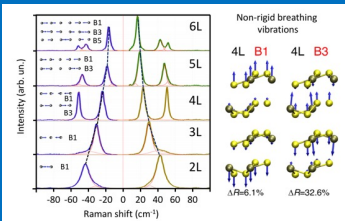Real-time diagnostics of plasma <u>and</u> substrate
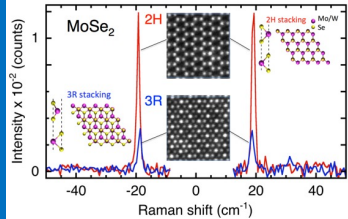– *Fully automated acquisition and control*

Laser spectroscopy to characterize atomically-thin quantum materials
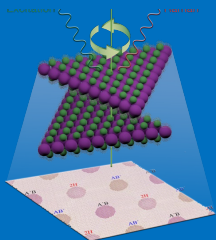
Low-frequency Raman spectroscopy

Number of layers and phases in 2D materials (PdSe$_2$)

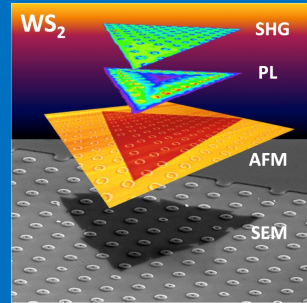### Stacking configurations of 2D crystals
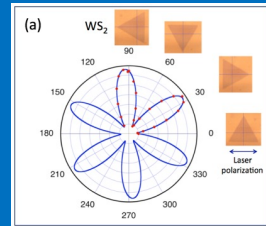
Coupling in twisted bilayers

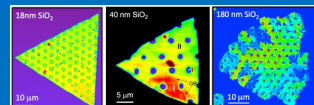## Photoluminescence (PL), Second harmonic generation (SHG)

Understanding conformal growth over curved features

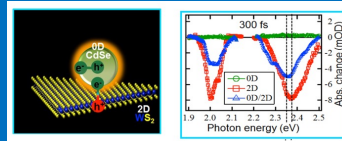### Revealing crystal orientation and strain in 2D crystals

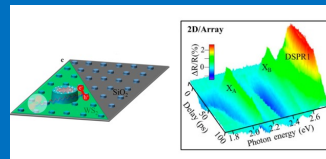### Understanding changes in growth mode: from single- to poly-crystals

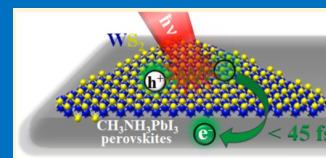## Ultrafast pump-probe spectroscopy of 2D materials and heterostructures

Revealing ultrafast charge transfer from WS$_2$ monolayer to CdSe QDs

Understanding ultrafast dynamics in 2D-WS$_2$/Al array
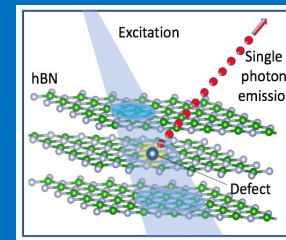
Understanding ultrafast exciton dissociation at 2D-WS$_2$ monolayer/perovskite interface

Single quantum emitters (SPEs) in 2D materials
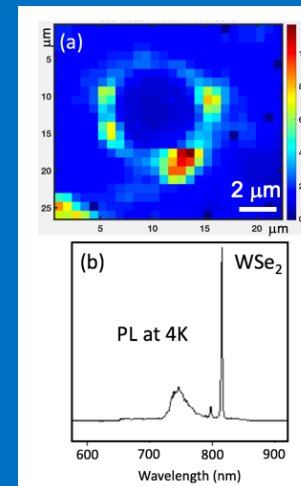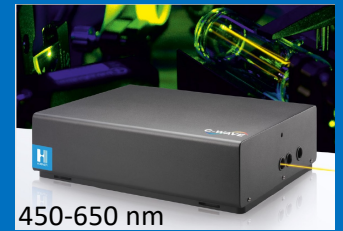
Defect induced generation of SPEs in 2D layered materials

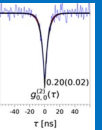### Understanding how strain in 2D materials creates SPEs

New capabilities
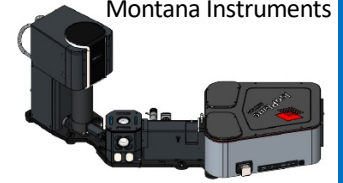
Unique tunable low- and high frequency Raman spectroscopy

450-650 nm

- Cryo-Raman, PL, SHG
- Photon statistics using SNSPD

Montana Instruments

Time-resolved CL SEM

- fs-laser driven FEG
- Laser/electron pump-probe spectroscopy

Kinetic Assembly of Building Blocks Controls the Dimensionality of Nanostructures

Oxides
(e.g., TiO$_2$)

vacuum — 200nm — *crystalline films*

150 Torr — 500 nm — *nanorods*
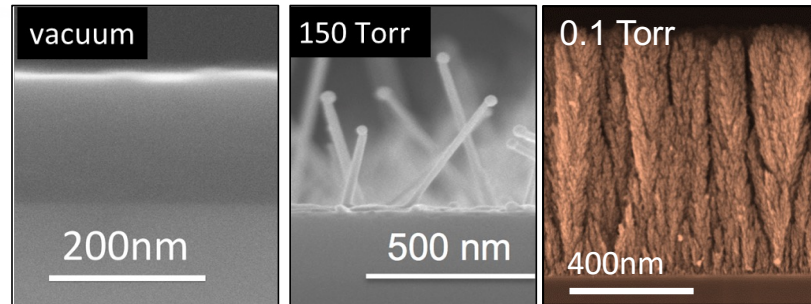
0.1 Torr — 400nm — *nanoparticle assemblies*

- *nanostructures for batteries*

- *mesoporous electrodes for dye-sensitized solar cells and photocatalytic water splitting*

2D Crystals
(e.g. GaSe)
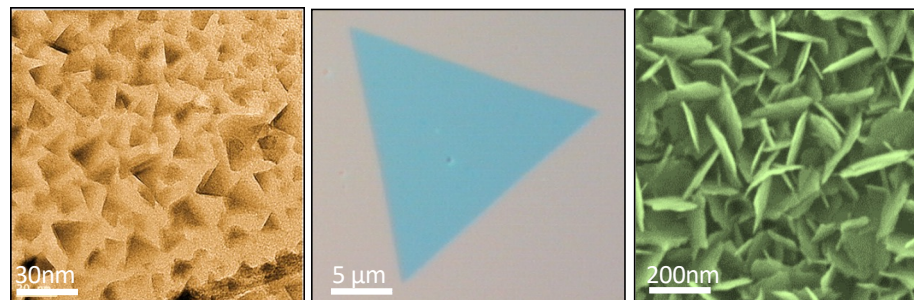
30nm — *nanosheet networks*

5 µm — *large single crystals*

200nm — *vertical nanoflakes*

- *photodetectors*
- *optoelectronics*
- *catalysis*

nanoscale building blocks – assembled differently

A crosscutting challenge: Understanding how dimensionality evolves in nanostructures

Pulsed Laser Deposition: 1. Tunable Kinetic Energy vs. P, d

High KE→
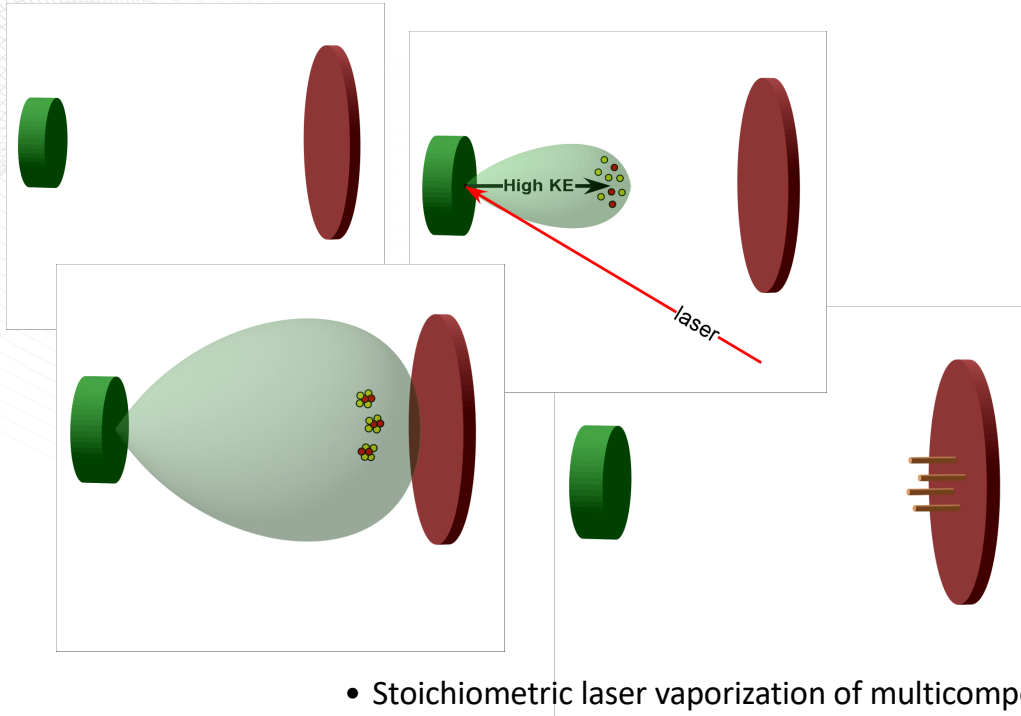
laser

What your eye sees (it integrates)
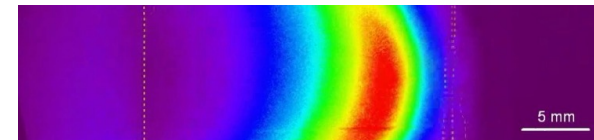
What a sequence of ICCD images sees

5 mm

- Stoichiometric laser vaporization of multicomponent targets
- Plasma expansion - v~10^6 cm/s, KE ~ to 100 eV.
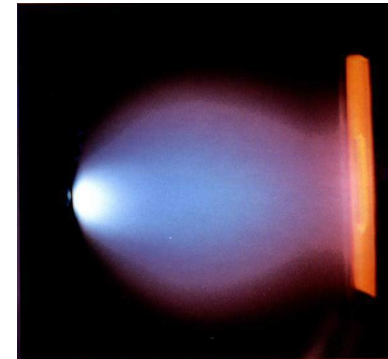- PLD plasmas can push through background gases up to ~200 mTorr to ~ 5-10 cm
- Adjustable confinement by background gas produces variable KE and times for reactive chemistry, and nanostructure (or thin film) formation.

Kinetic energy in the laser ablation process enables the formation of metastable phases

Advantages of PLD: 2. Non-equilibrium conditions for Metastable Nanostructure Formation due to Reactant Confinement vs. T, t, d

• Spatial confinement of reactants provides the time, temperature, and fluxes required for metastable nanostructure formation.

• The product distribution is a result of the competition between kinetic and thermodynamic pathways.

• Note advantage over PLAL: Inert gas

laser 1

Nonequilibrium
(pulsed) process

Atoms, molecules

Nanoparticles

Crystalline
Nanorods

Ultrasmall
Building Blocks

Nano-
horns / tubes
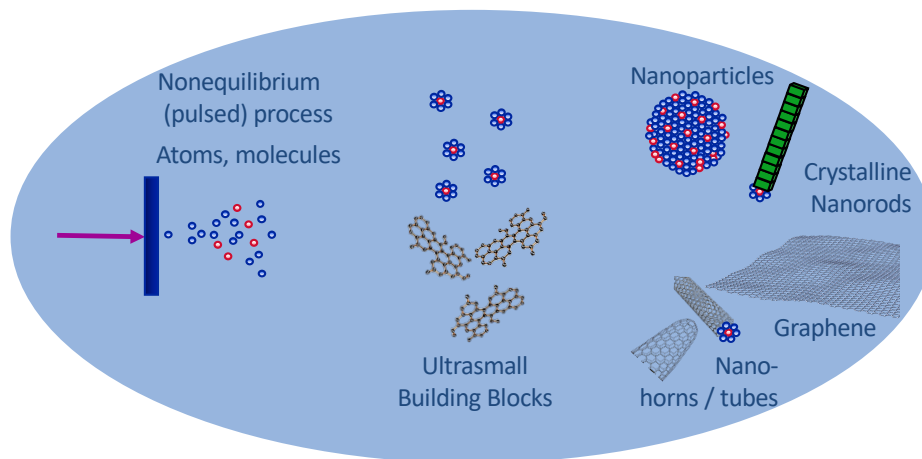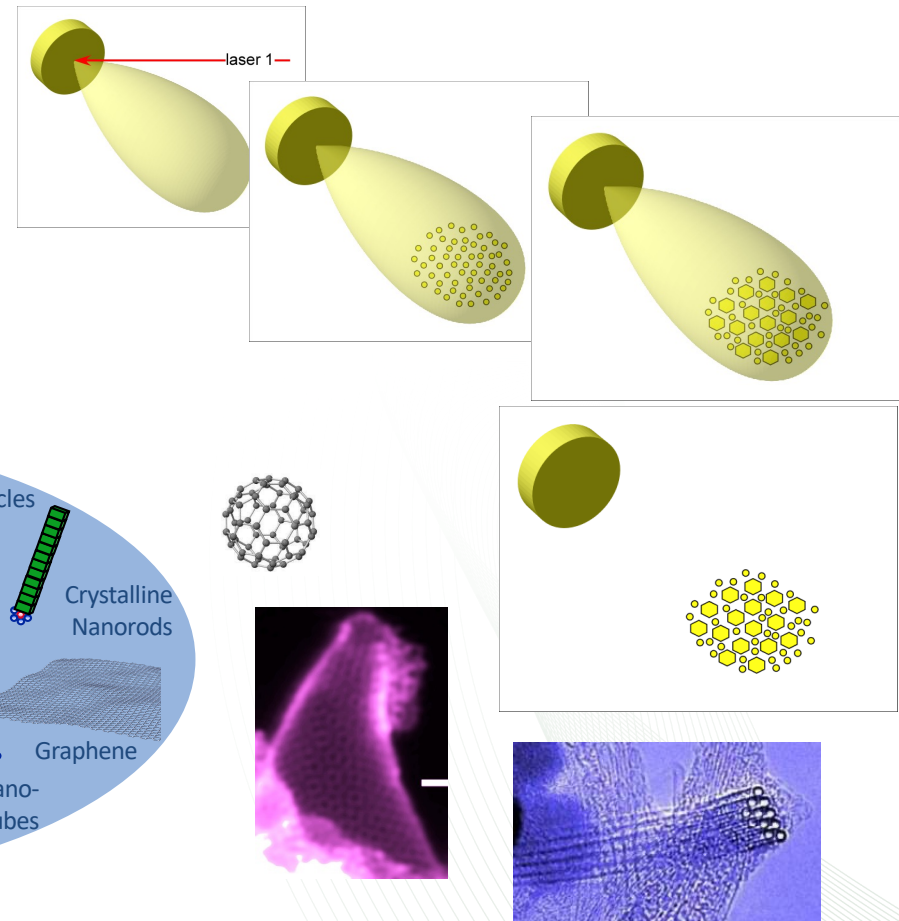
Graphene

Variety of Carbon Nanostructures from PLA and confinement
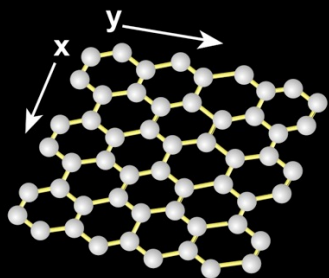
Graphene
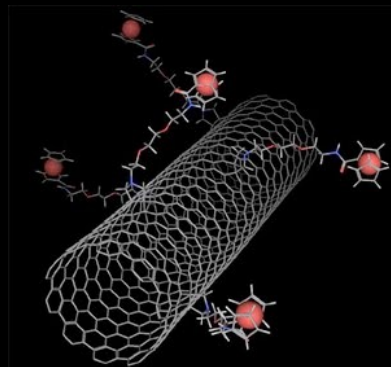
Single-wall nanotube

Multi-wall nanotube
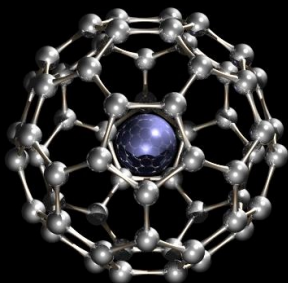
Endohedral fullerene
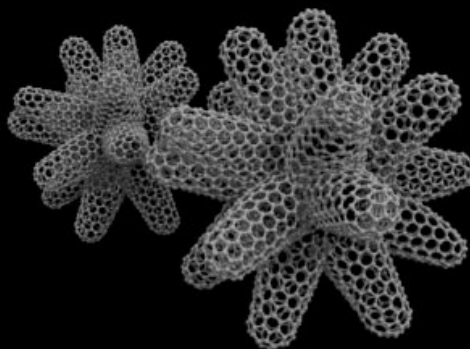
Single-wall nanohorns
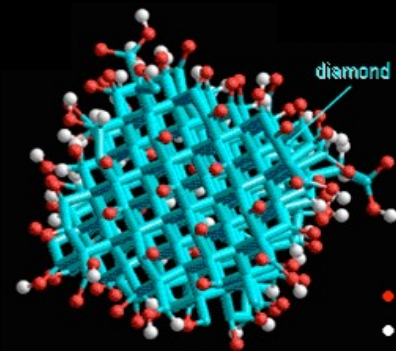
Nanodiamond

Synthesis Pathways in Carbon

R.B. Heimann, Carbon **35**, 1654 (1997)
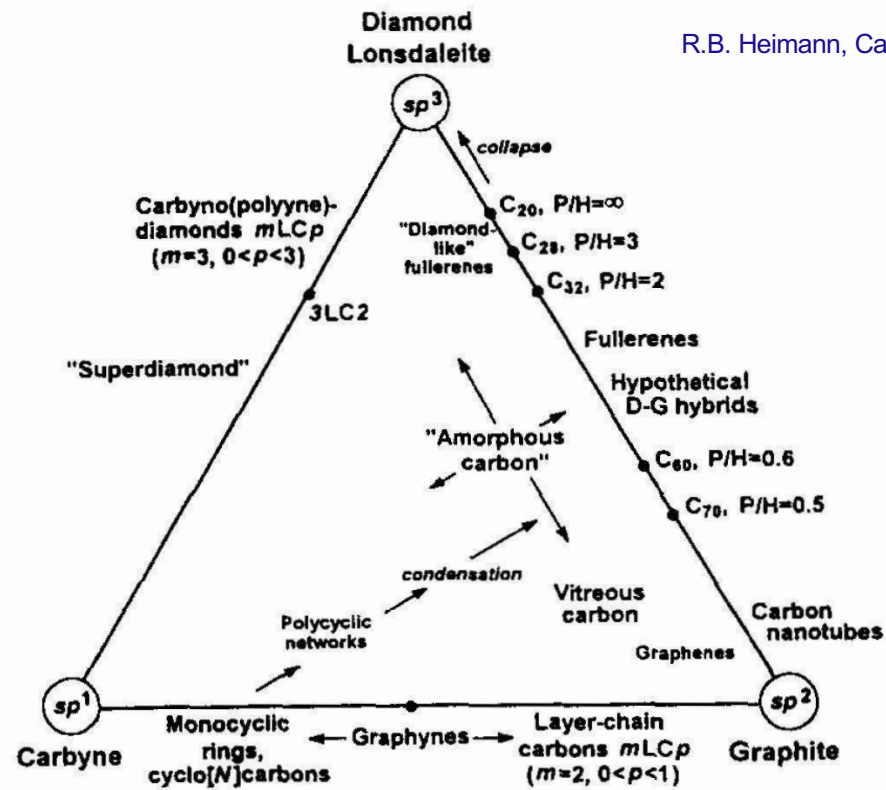
Synthesis typically occurs under extreme conditions with high μ(P,T)
Lasers can provide such non-equilibrium conditions !

'Puretzky Plot' - SWCNT growth by laser vaporization
based on spectroscopic diagnostics of ejected material

SWNT grow over extended periods of time from a feedstock of aggregated clusters and nanoparticles - *condensed phase conversion Growth rates 1-5 μm/s*

Ar flow

cm

Eutectic temp. Ni/C, Co/C

Short tubes < 240 nm

Carb. metal clust.

Carbon clust., atomic Ni, Co
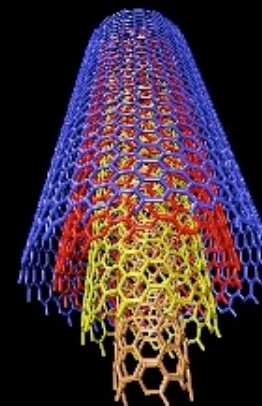
Atomic/molecular vapor: C, C_2, C_3, Ni, Co

Laser

5×10^{16} carbon
10^{14} Ni/Co

onset of SWNT growth

Target

0	1μs	10μs	100μs	1ms	10ms	100ms	1s

Temperature °C   2500   1100   oven temperature

3500 2500 1750 1400 1326 1100

d = 1.2-1.5 nm SWCNT

SLIMS 2
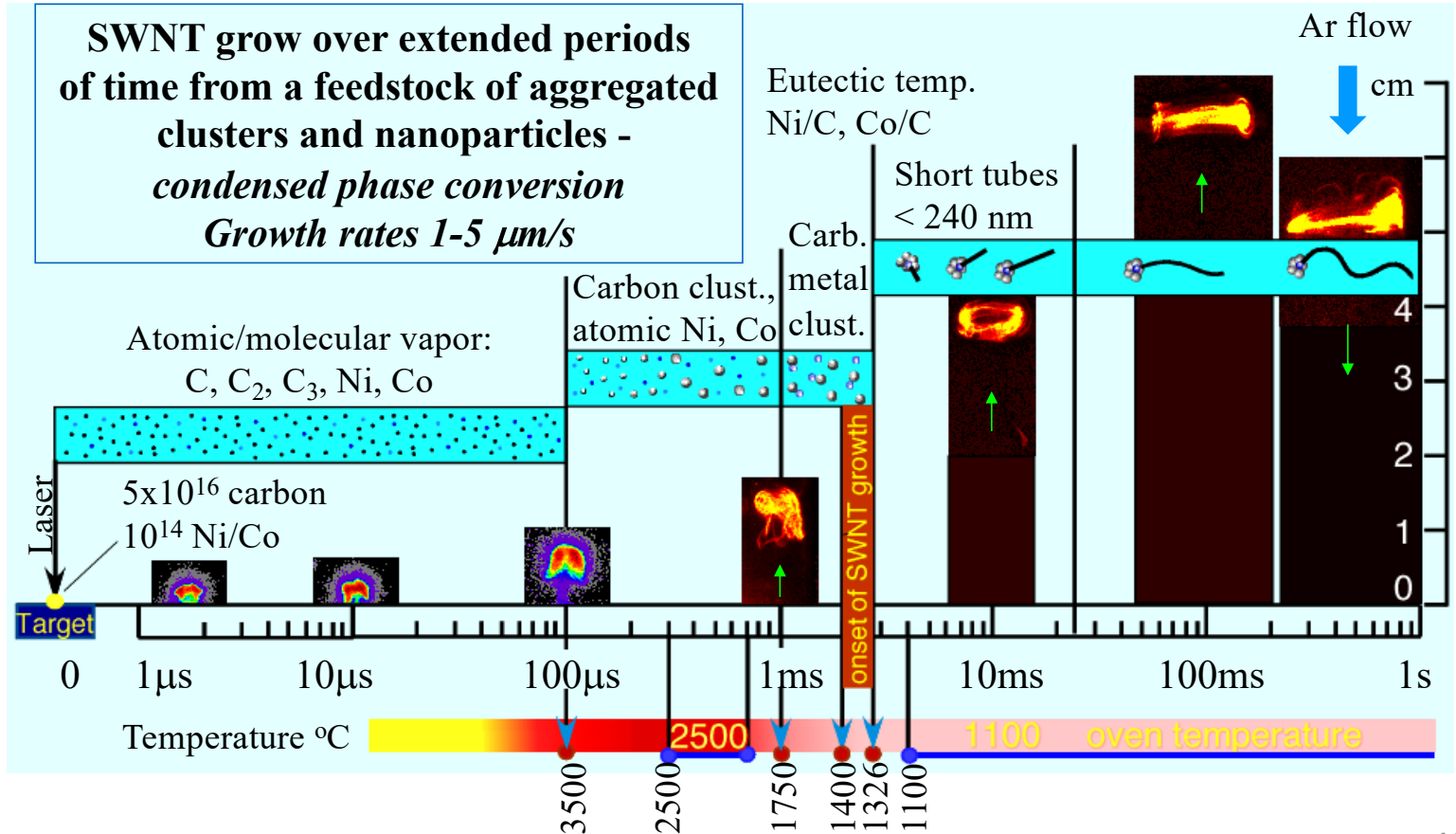
A. A. Puretzky et al, *Phys. Rev. B* **65**, 245525 (2002).

13
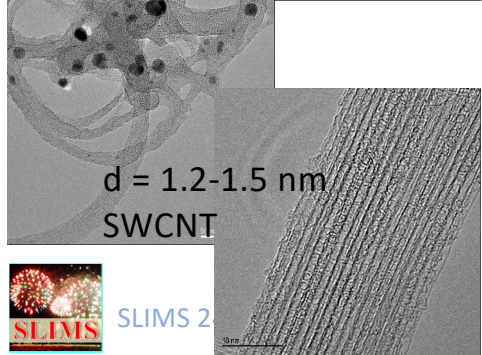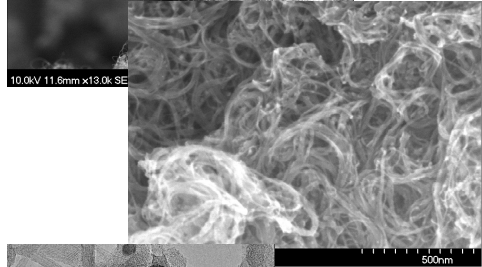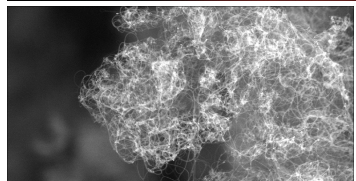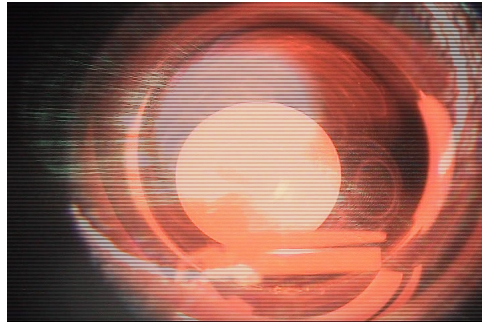
In situ diagnostics in PLD – from atoms/ions to clusters/nanoparticles

- **Plume position and dynamics**
  - Gated ICCD imaging using 2nd laser
  - Ion probe
- **Composition vs. time**
  - Optical emission spectroscopy
  - Laser-induced fluorescence spectroscopy
- **Temperature vs. time**
  - Blackbody emission
  - Laser-induced incandescence
- **Particle sizes**
  - Rayleigh scattering
  - Optical absorption spectroscopy
- **Ultra-small nanoparticles**
  - Photodissociative spectroscopy
  - nano-differential mobility analyzer

100 mTorr
1cm

10 nm

target
plume
Dissociation beam sheet
To spectrometer
laser
To ICCD
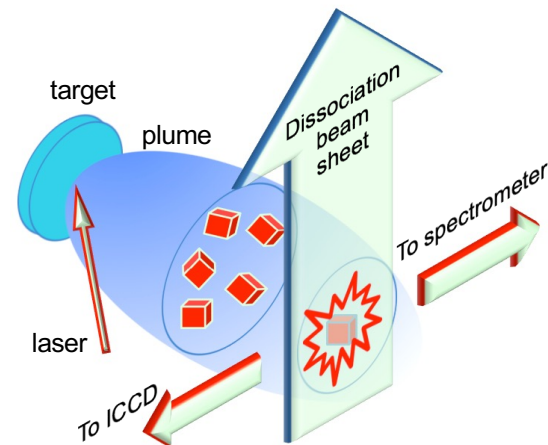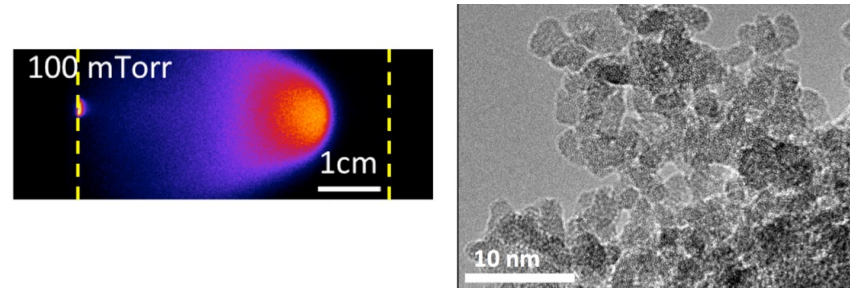
Single−Wall Carbon Nanotube
Production by Laser Vaporization

Vortex Rings

Web Formation
Conditions
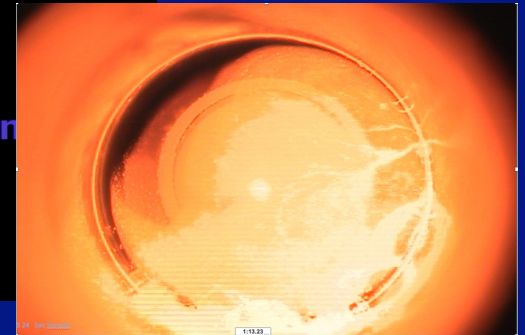
Material Anneals . . .
. . . as it Floats in the Oven

Movie showed a simple laser-oven growth of SWCNTs from LV of carbon with 1%Ni and 1%Co target, 10Hz, in Argon, at 1200°C. As shown in the "Puretzky Plot", the laser vaporized material condenses and gets trapped in vortex rings where it anneals for several seconds in the oven. During this time the SWCNTs grow at ~ 1 micron / second from a feedstock of clusters, particles, and graphenic sheets (i.e., condensed phase (not gaseous). SWCNTs aggregate into webs and bundles and flow out of the oven.

D. Geohegan
A. Puretzky
H. Schittenhelm
Solid State Division
Oak Ridge Nat'l. Lab.
Music by 3rd Force
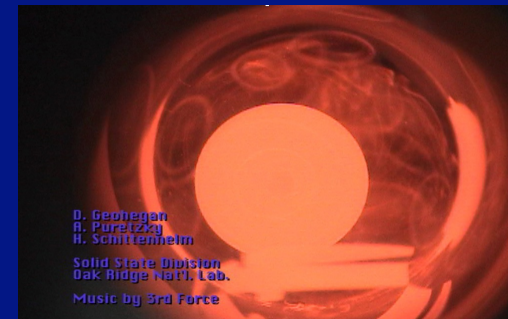
For single-wall carbon nanohorns which are grown from pure carbon targets without the metal catalyst used for carbon nanotubes, longer laser pulse widths are necessary to provide time for carbon to self-assemble into tube-like "nanohorn" units. Laser pulses of 20 ms were used. Individual nanohorn 'bottles' that form the aggregate balls of ~100-200nm diameter, grow at ~ 1 nm/ms, which is equivalent to 1μm/s, which is considered a fast growth rate for carbon nanotubes grown by catalyst. Both nanotubes and nanohorns grown in the gas-phase by laser vaporization, are limited in production by how fast lasers can vaporize carbon.

High-Power Laser Vaporization Synthesis of Carbon Nanohorns and Nanotubes at ORNL

- Exploration of Laser Synthesis of Nanomaterials
  - Tunable Pulse Width (> 0.5 ms)
  - Variable Energy (1-100 J/pulse)
  - High Average Power (<600W)
  - High Temperature
  - High Volume (10 g/hour)

10 nm

1 μm
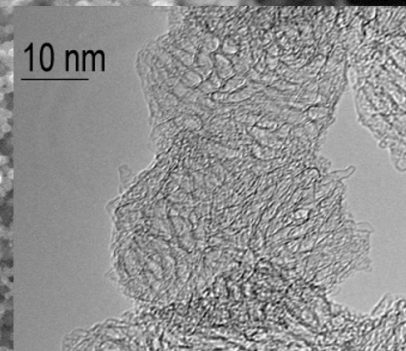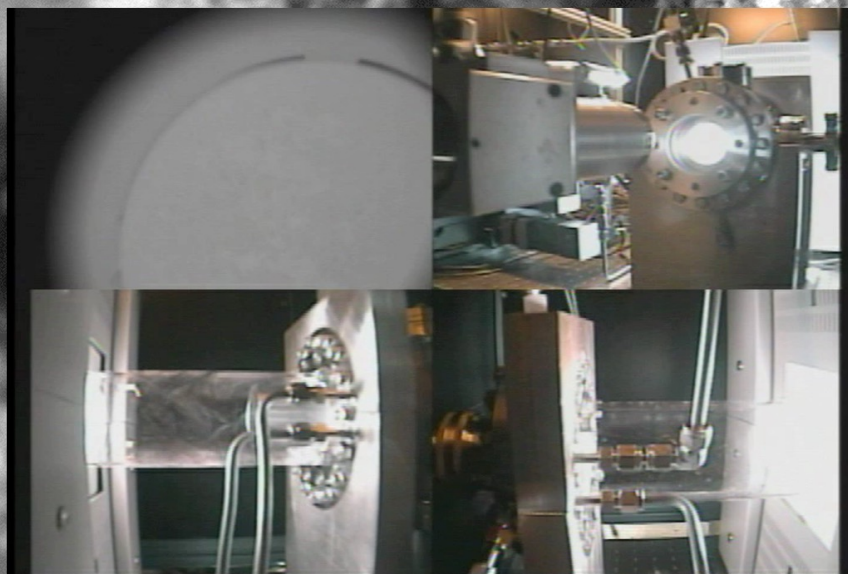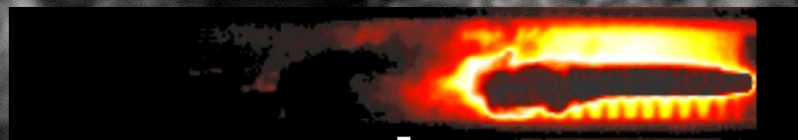
Amorphous Diamond *(ta-C)* deposition by PLD from pure C target in vacuum at RT

90 eV C⁺
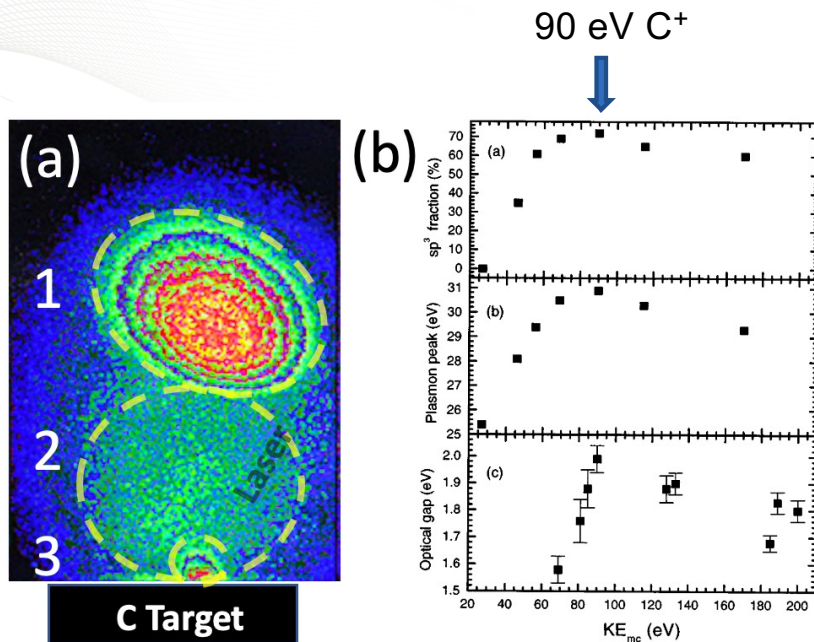
Bright ball of C+ ions traveling 4 cm/µs captured by gated ICCD imaging of plasma fluorescence

PLD with high KE (90 eV/atom) can form ''amorphous' diamond films
- Tetragonally coordinated amorphous carbon with 70% sp^3 bonding
- Hyperthermal implantation densifies sp^2 carbon, converting into new metastable phases
- Ultrahard, transparent coatings – now commercialized for razor blades, eyeglasses, hard drives, etc.
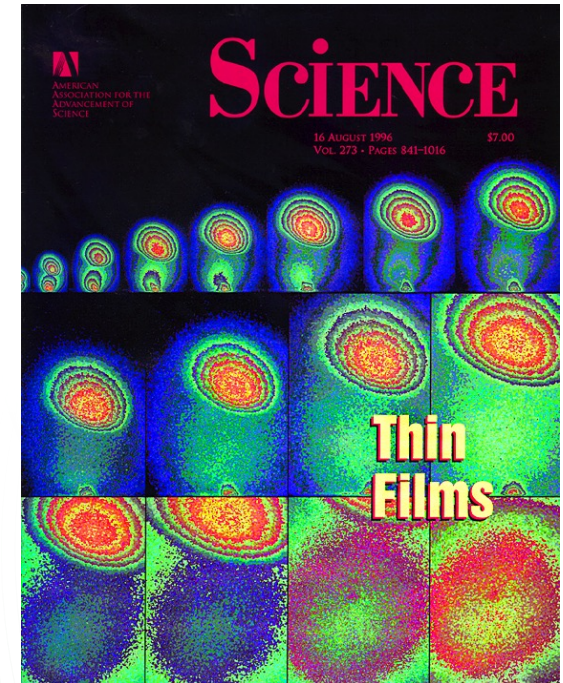
D.H. Lowndes, et al., Science **273**, 898 (1996)

In situ Diagnostics of *ta-C (tetragonally coordinated amorphous carbon)* Diamond-Like Carbon (DLC) Film Growth by Laser Ablation: Role of Kinetic Energy

Calculated structure of DLC film confirmed by neutron scattering
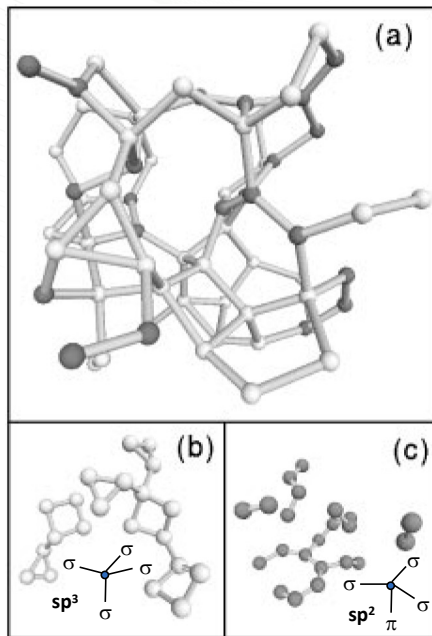
N.A. Marks et al., *Phys. Rev. Lett.* **76**, 768 (1996)

DLC film parameters vs. C+ kin. energy

sp³ fraction

plasmon peak

optical gap
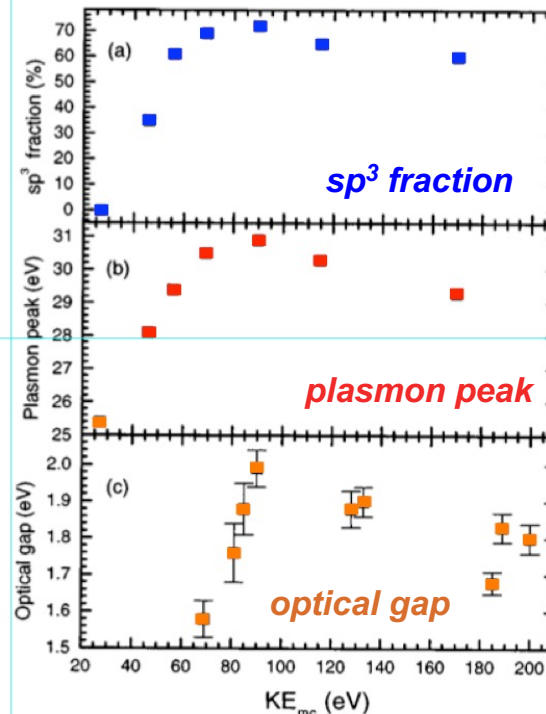
V.I. Merkulov et al., *Appl.Phys. Lett.* **73**, 2591 (1998)

1792   J. ROBERTSON

ion subplantation   relaxation during thermal spike

direct entry

knock-on
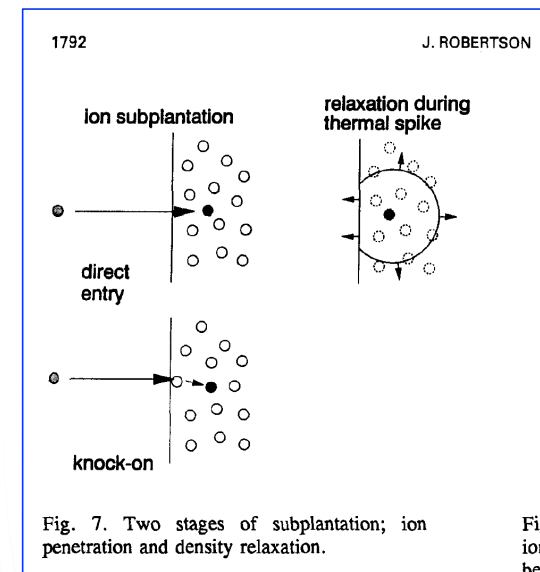
Fig. 7. Two stages of subplantation; ion penetration and density relaxation.

T_d > 25 eV to displace C atom in graphene – then implantation

The sp³/sp² ratio varies depending on kinetic energy of carbon species.

Deposition of *ta*-C (amorphous diamond) in vacuum

- Gas dynamic plume interactions in vacuum at a substrate

- Species resolved imaging shows C_2 forms from C^+ plume component interactions with substrate in vacuum
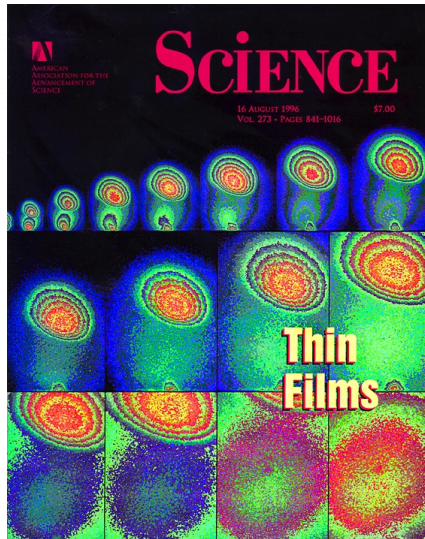
"Synthesis of Novel Thin-Film Materials by Pulsed Laser Deposition", D. H. Lowndes, D. B. Geohegan, A. A. Puretzky, D. P. Norton, and C. M. Rouleau, *Science* **273**, 898 (1996)

KrF-laser
Si-substrate →
← graphite target
0   1   2   3   4 cm

- Different plasma components: origin, time evolution and propagation
- Near-target carbon plume dynamics
- Near-substrate processes

427 nm C+

470 nm C2

575 ns

Fast Carbon Ions (leading edge. 8 cm/μs)

Near-target C2 dynamics and propagation

575 ns

775 ns

Deposition and Collisions near Substrate Surface - Shock heating

Cluster formation from near-surface collisions

775 ns

10 μs

10 μs

Broadband emission (cluster and blackbody emission to ~ 1ms)

KE in eV = 0.52 M v^2

M: Atomic mass
v: in cm/μs

e.g. 0.5 (12) 8^2

= 376 eV

This is a handy formula to get the kinetic energy of an atom or ion of mass M, with velocity v, as measured from the plasma plume images time-of-flight.

Acceleration of the Plume – ArF vs. KrF – Effects on ta-C Band gap

- The fast C^+ ions in the carbon plume are produced through the photoinduced breakdown in the C, C_2, C_3 vapor plume

- The threshold of this breakdown is very sensitive to wavelength

- The properties of DLC films are defined **not only** by the kinetic energy of C^+ <u>but also by</u> the degree of the photoinduced conversion of C_2, C_3, into C+
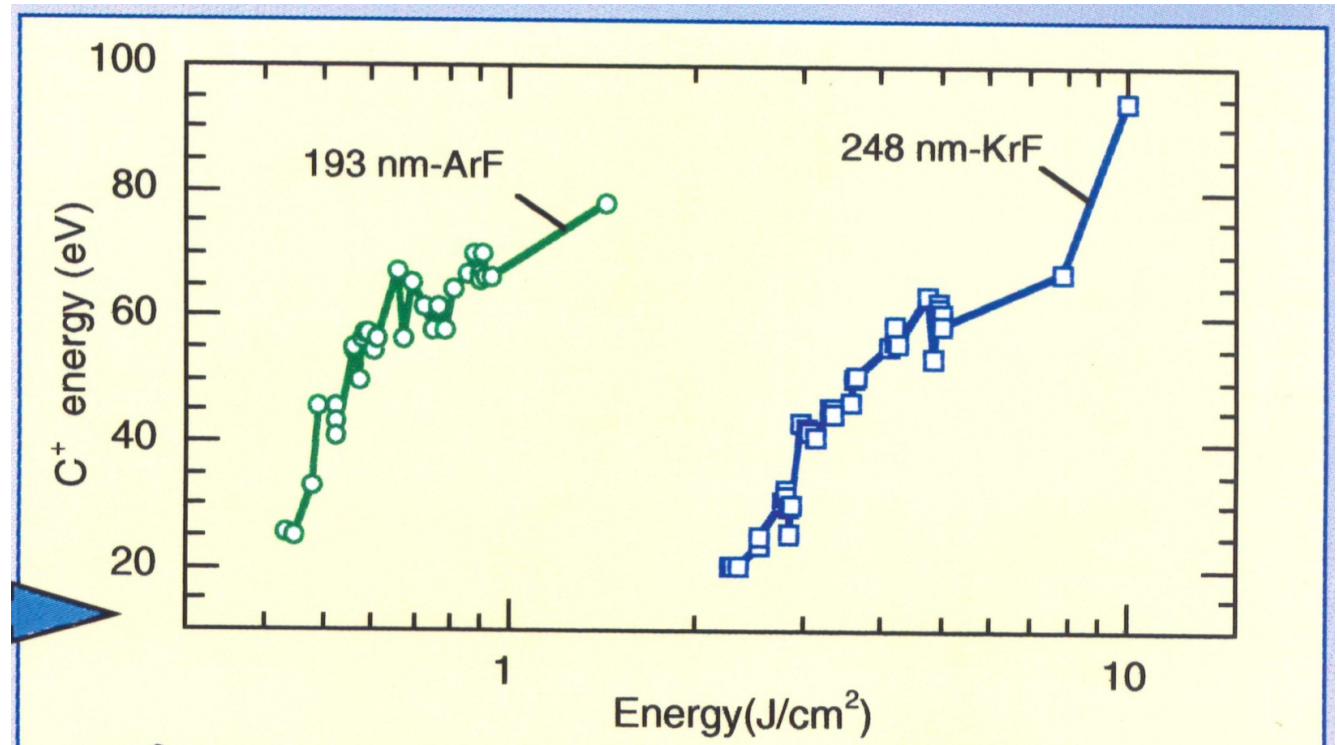
Why does ArF accelerate the plume at much lower fluiences than KrF?

Laser Interactions with the ejecta within the laser pulse

- Multiphoton ionization (resonant two-photon) of C

- More effective for ArF

- Yields higher C+ kinetic energies
  - More effective for amorphous diamond film growth
  - Less effective for nanotube growth

- Wavelength-dependent laser-ejecta interactions can play a major role in subsequent cluster and nanoparticle formation

Answer: The plasma is accelerated by the laser interacting with the initial ejecta, which ionizes the C atoms produced by photodissociation of C_2 and C_3. ArF resonates much better with the intermediate state of carbon atom, making it much more effective.

Restricted Energy Level Diagram of Carbon ArF and KrF Near-Resonances

eV		
12		
11	11.26 ///////// I.P.	
10	ArF	KrF
9		
8		$3s\,(^1P_1{}^O)$
7		
6	—	
5	ArF	KrF
4		
3		
2	2.68	$2p^2\,(^1S_0)$
1	1.26	$2p^2\,(^1D_2)$
0		3p

C
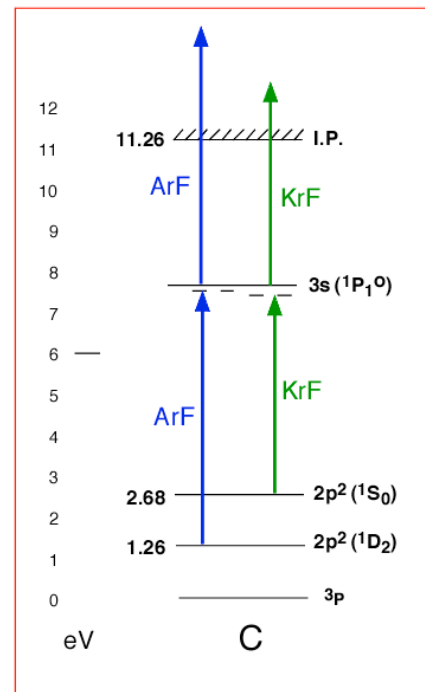
193.09 nm and 247.93 nm

est. 90% and 15% I_{peak}, resp.

Acceleration of the plume in vacuum – laser interactions with primary ejecta

- Initial ejecta C_2 and C_3 at low fluence

- Dissociation of C_2 to form atomic C

- Speedup of plume

- N.B. Gas dynamic effects on C_2 and C_3 at target surface

ArF-laser ablation of graphite in vacuum: gasdynamic interaction within the plume
ICCD imaging (600-620 ns)

ArF-laser fluence (J/cm^2)

| 0.4 | 0.45 | 0.50 | 0.55 | 0.60 | 0.70 | 0.96 |
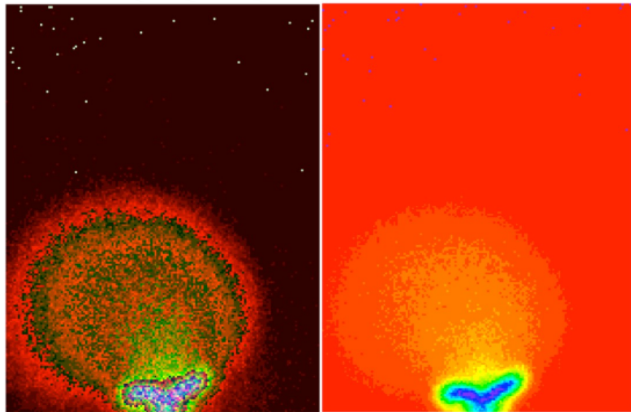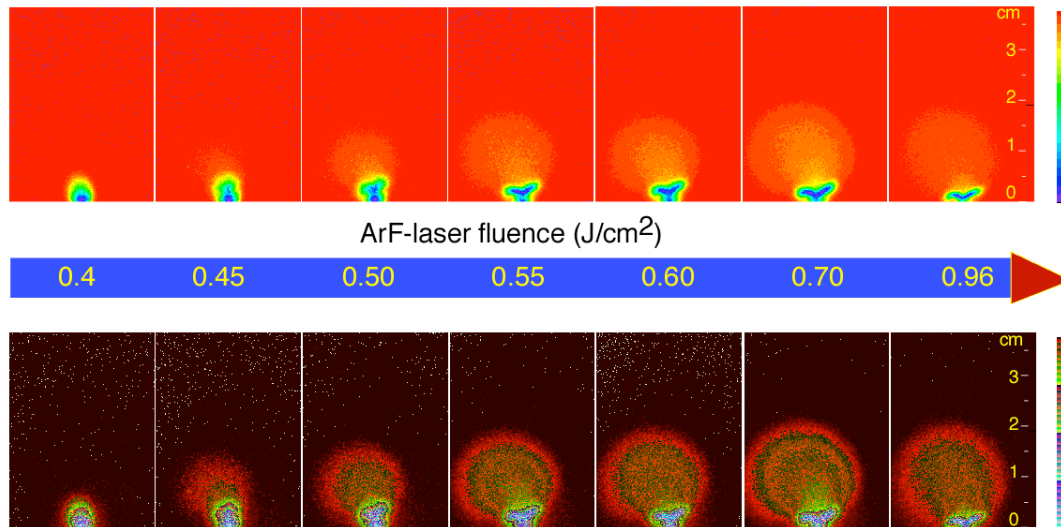
"Comparative diagnostics of ArF- and KrF-laser generated carbon plumes used for amorphous diamond-like carbon film deposition"
Puretzky, A.A.; Geohegan, D.B.; Jellison, G.E.J.; McGibbon, M.M. Applied Surface Science, Vol: 96-98, pp. 859-865, (1996)

Acceleration of the plume in vacuum – photoionization to make the fast ions

- Formation of the third (fast ion component)

- Gas dynamic

- interactions during high-pressure period of plume expansion lead to clustering and changes in angular distributions of ejecta

KrF-Laser Ablation of High-Purity Graphite
(delay 600-650 ns, unfiltered images)

1.9 J/cm² · 2.3 J/cm² · 2.7 J/cm² · 3.2 J/cm² · 3.8 J/cm² · 3.8 J/cm²
4.5 J/cm² · 5.4 J/cm² · 7.5 J/cm² · 9.7 J/cm² · 14.3 J/cm² · 17 J/cm²
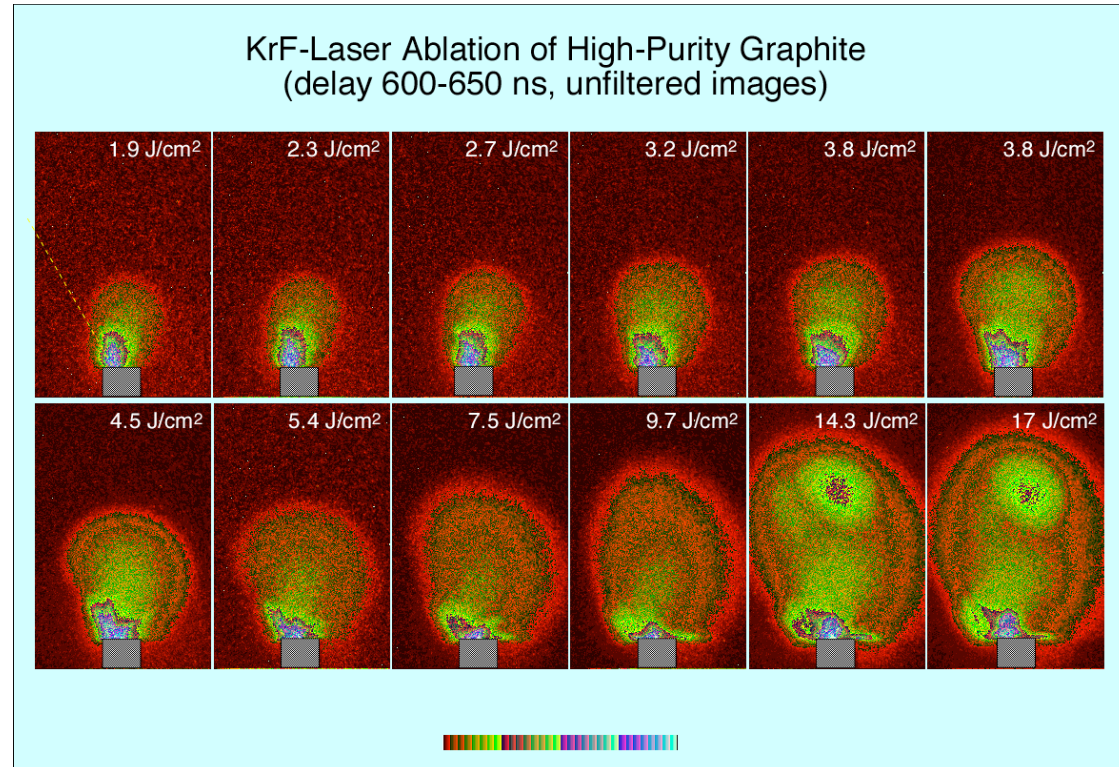
Details of Thermalization of the Plume

slowing and plume splitting

Plume Thermalization
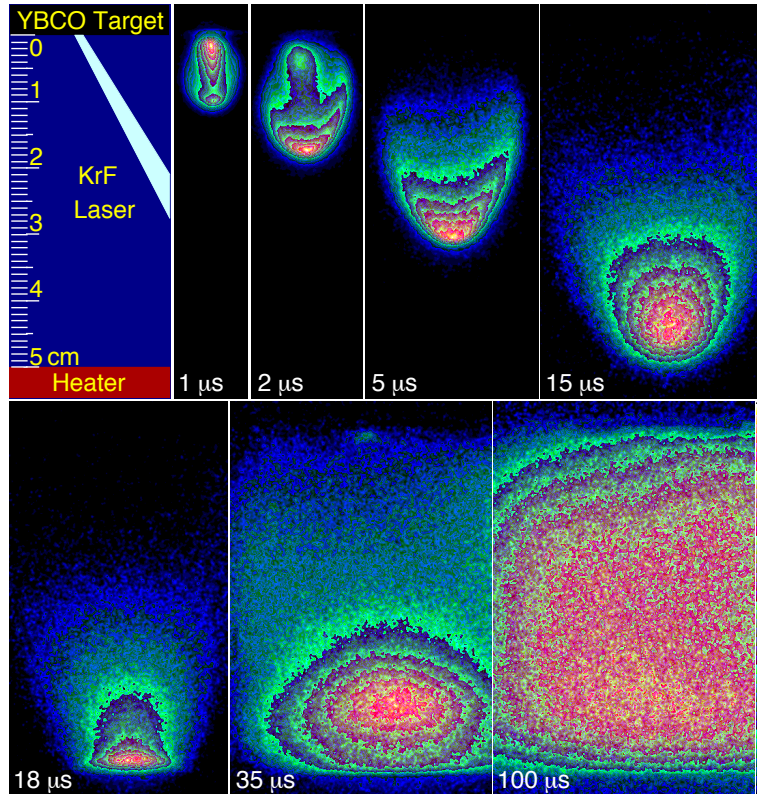
- ICCD images and ion probe currents for YBCO ablation at 248 nm, d = 5 cm
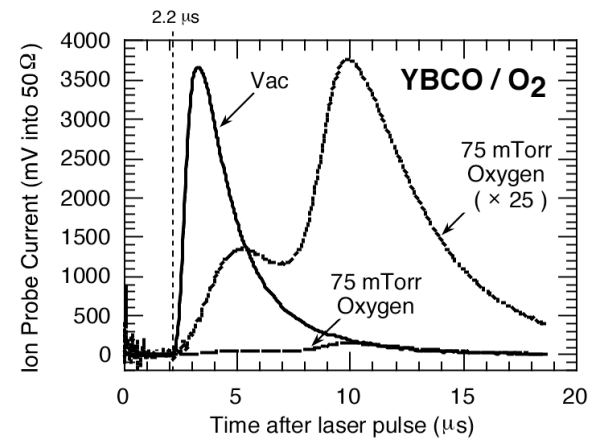 - Exponential attenuation of ions with d
  - "slowing" of original plume
  - Second component of plume observed

8. D. H. Lowndes, D. B. Geohegan, A. A. Puretzky, D. P. Norton, and C. M. Rouleau, *Science* **273** *(5277), 898-903 (1996).*

Shock and Drag Models - Plume Thermalization
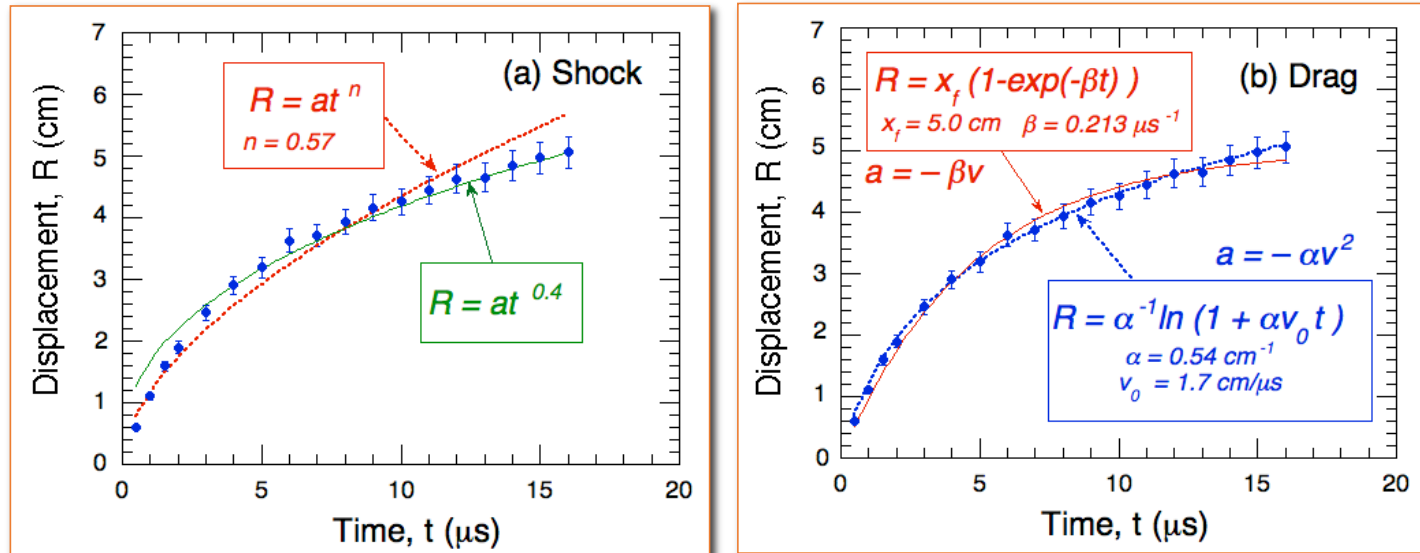
Several phenomenological models have been applied to describe plume propagation in background gases

D. B. Geohegan et al., NATO-ASI on Excimer Lasers (1993) (available online www.ornl.gov/~odg)

Drag Models

$$a = -\alpha v^n$$

R = x_f (1-exp(-βt))

$x_f = 5.0$ cm $\beta = 0.213$ μs^{-1}

$a = -\beta v$

(b) Drag

$a = -\alpha v^2$

$R = \alpha^{-1} \ln(1 + \alpha v_0 t)$

$\alpha = 0.54$ cm^{-1}

$v_0 = 1.7$ cm/μs
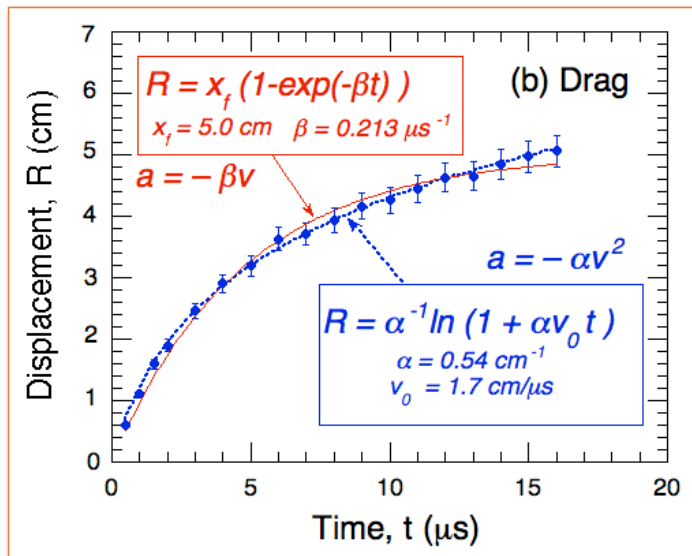
| n = 1 | $a = -\beta v$ | $[\beta] \sim s^{-1}$ |

$$v = v_0 e^{-\beta t}$$

$$x = \frac{v_0}{\beta}(1 - e^{-\beta t})$$

| n = 2 | $a = -\alpha v^2$ | $[\alpha] \sim m^{-1}$ |

$$v = \frac{v_0}{1 + \alpha v_0 t}$$

$$x = \frac{1}{\alpha} \ln(1 + \alpha v_0 t)$$

D. B. Geohegan et al., NATO-ASI on Excimer Lasers (1993) (available online www.ornl.gov/~odg)

Plume Imaging - Scaling the images equally (please be careful !)

- Images are normally scaled to their peak values, however for comparison with other images, they should be scaled equally

- Equally scaled images show the unscattered plume atoms ahead of the brightest part of the shock front
    - of equal intensity as the "vacuum" plume.
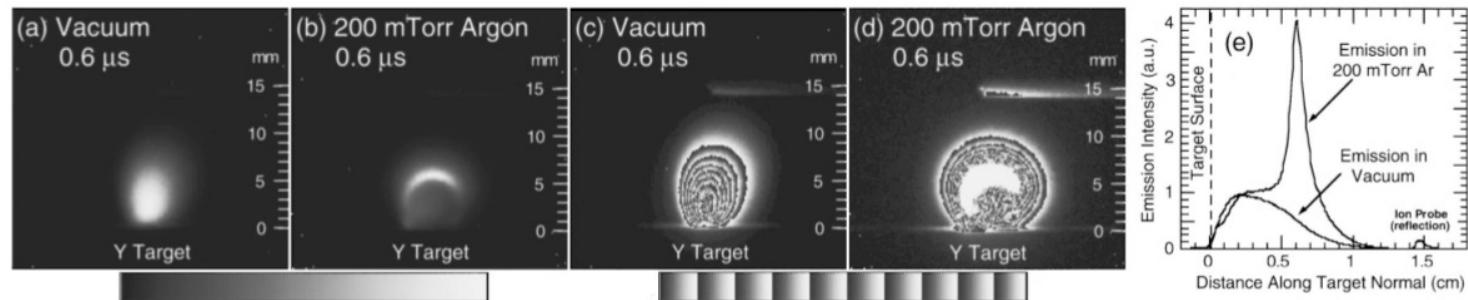
With proper scaling, the comparatively weak emission of the fast component is revealed

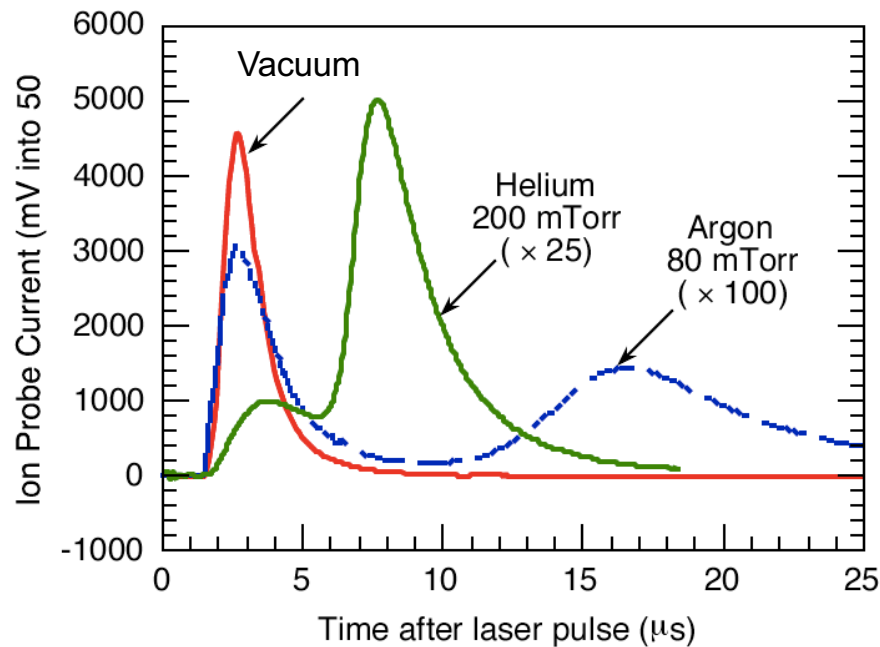# Plume Splitting – Si/Ar vs Si/He – Experimental results


- The primary peak contains unscattered plume atoms / ions

- The delayed peaks contain flux distributions from the various scattering events (I.e. one collision, two collisions, …) with the background gas.

- Both the relative peak heights, and the peak time delays, can be simultaneously fit over all distances with the choice of a single scattering cross section.

Plume Splitting
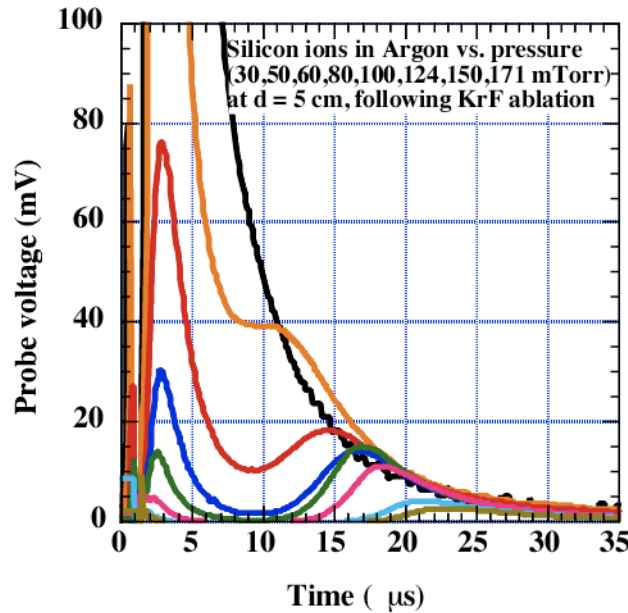
Silicon in Argon background **Silicon in Helium background**
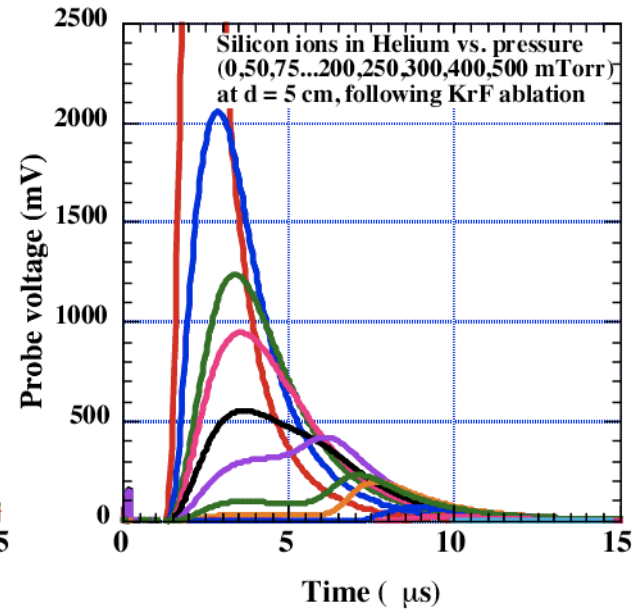
- Ion probe currents measured at d = 5 cm as the gas pressure is raised.
- Exponential attenuation of plume ions (integrated areas of curves)
- Behavior is different for He, vs. Ar

Elastic Scattering – Si/Ar vs. Si/He

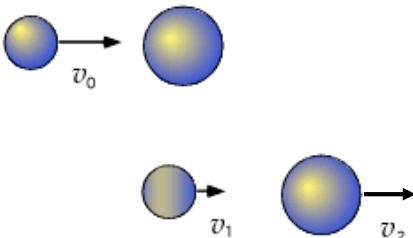- Si/Ar shows a fast transmitted distribution identical to the 'vacuum' distribution. Si/He is noticeably slowed.

- In both cases, material is lost exponentially with distance and pressure, in accordance with scattering corresponding to mean-free-paths ~ 1 cm.

Elastic Collisions

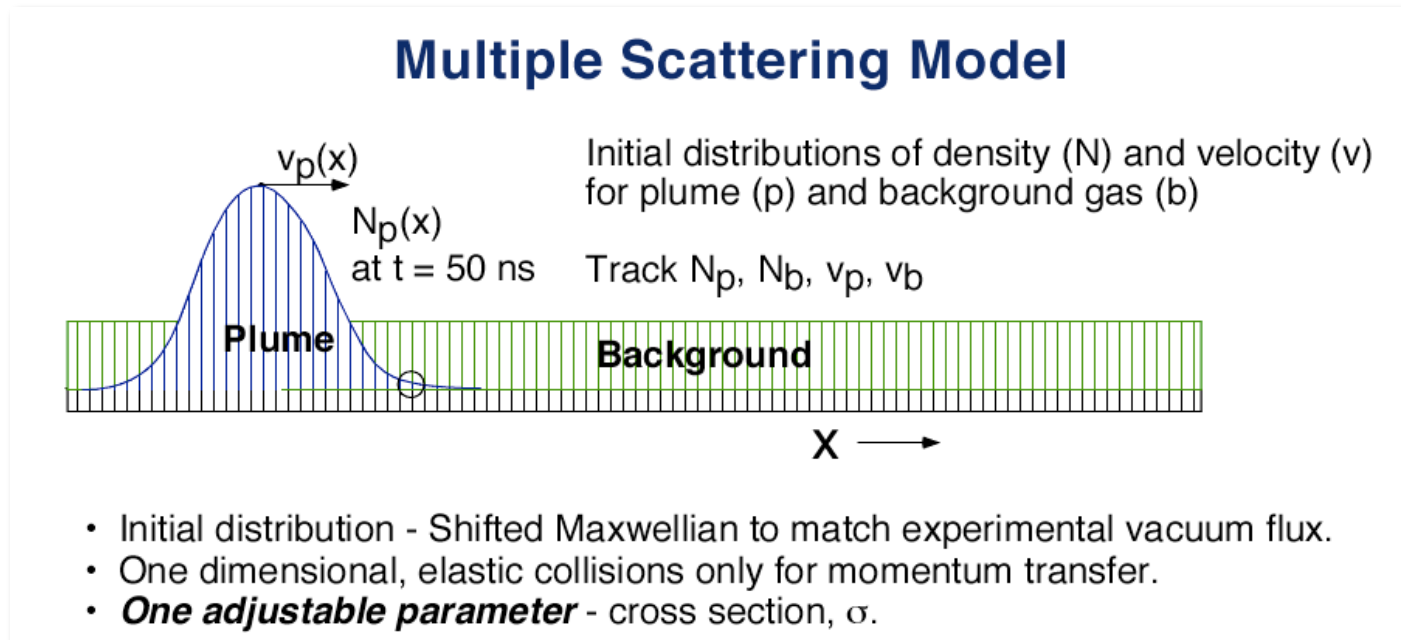$$I = I_0 \ \exp(-N\sigma x)$$

$$\sigma \sim 3 \times 10^{-16} \ cm^2$$

	Si/Ar (28/40)	Si/He (28/4)
$v_1 = \dfrac{m_1-m_2}{m_1+m_2} v_0$	$-0.18v_0$	$0.75v_0$
$v_2 = \dfrac{2m_1}{m_1+m_2} v_0$	$0.82v_0$	$1.75v_0$

Plume Splitting – Multiple Scattering Model

Multiple Scattering Model

$v_p(x)$

$N_p(x)$

at t = 50 ns

Initial distributions of density (N) and velocity (v) for plume (p) and background gas (b)

Track N_p, N_b, v_p, v_b

Plume

Background

X ⟶

- Initial distribution - Shifted Maxwellian to match experimental vacuum flux.
- One dimensional, elastic collisions only for momentum transfer.
- *One adjustable parameter* - cross section, σ.

Plume Splitting – Multiple Scattering Model

Time: $t = t_n$

order

0

1

2

3

$\vdots$

target

x

x_D
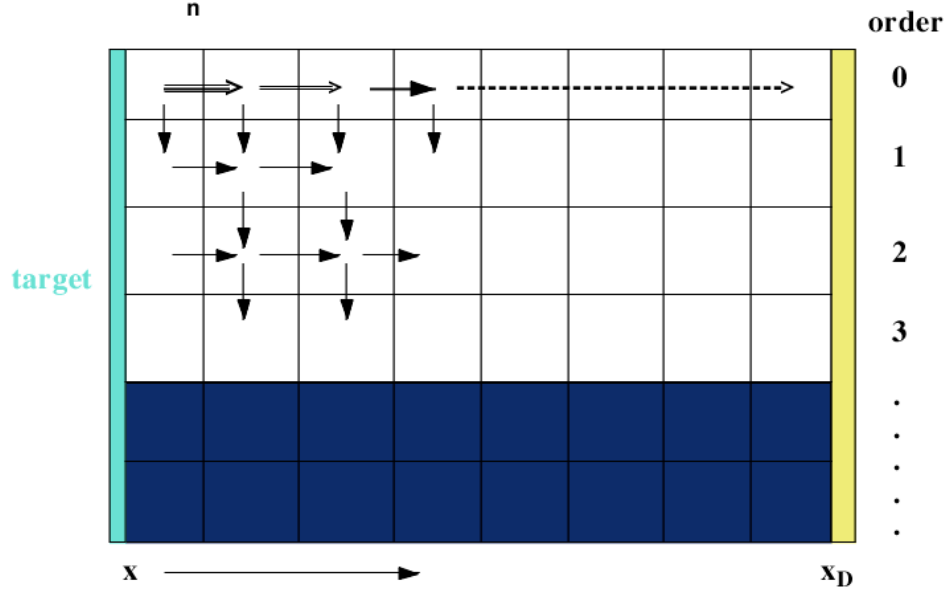
- Distributions separately tracked ("orders") according to how many collisions with the background gas.
- Collision rate (each time step)

$$\frac{dN_p}{dt} = N_p \, N_b \, \sigma \, v_{rel} \qquad v_{rel} = v_{p_j} - v_{b_{j+1}}$$

gives number scattered from traveling plume into cell (j + 1)

$$N_{p_{scatt}} = N_{p_0} \left(1 - \exp\left[-N_b \, \sigma_{p\text{-}b} \, v_{rel} \, \Delta t \right] \right)$$

R. F. Wood, K. R. Chen, J. N. Leboeuf, A. A. Puretzky, and D. B. Geohegan, *Physical Review Letters 79 (8), 1571-1574 (1997).*

R. F. Wood, J. N. Leboeuf, D. B. Geohegan, A. A. Puretzky, and K. R. Chen, *Physical Review B 58 (3), 1533-1543 (1998).*
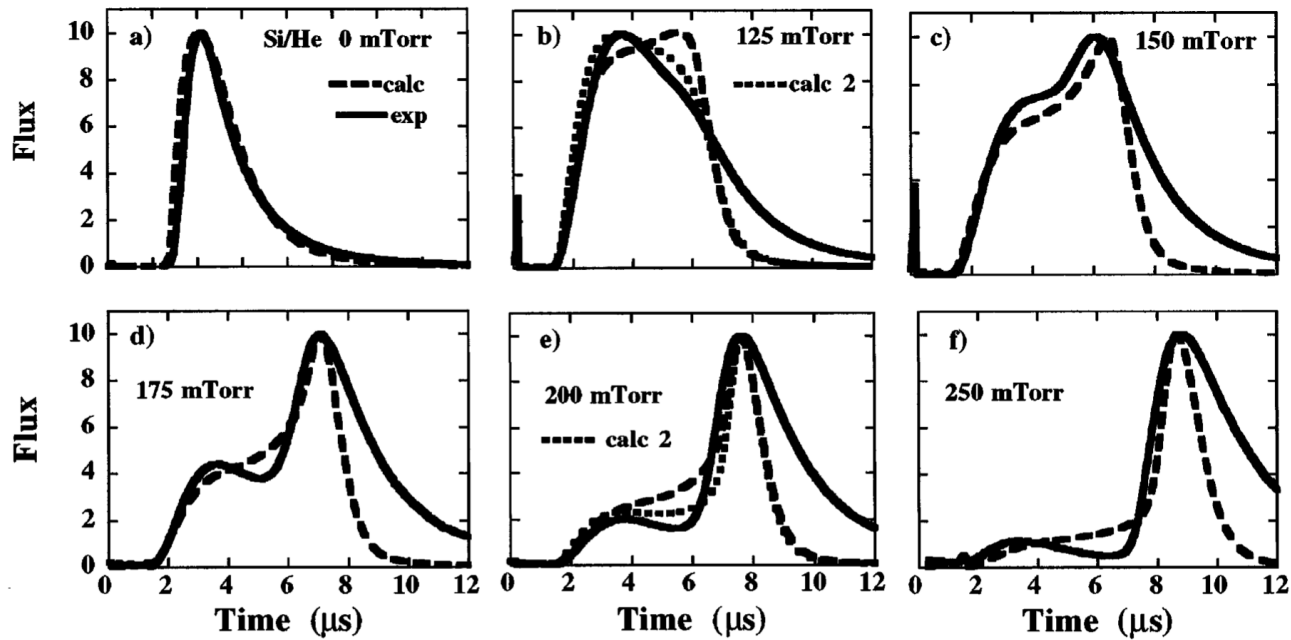
Si Plume Splitting – Experiment vs. Theory – 1

FIG. 2. Detailed comparison of the experimental and calculated results for Si/He. N_K and σ_{pb} were varied to obtain a satisfactory fit at 200 mTorr after which only the pressure was assigned the other experimental values. The various panels are discussed in the text.

R. F. Wood, K.R. Chen, J. N. Leboeuf, A. A. Puretzky and D. B. Geohegan, "Dynamics of Plume Propagation and Splitting during Pulsed Laser Deposition" *Phys. Rev. Letters 79(8), 1551 (1997).*

Si Plume Splitting – Experiment vs. Theory – 2

Understanding the Ion Probe Flux
as the sum of scattering "orders"
(for clarity only a few are shown)
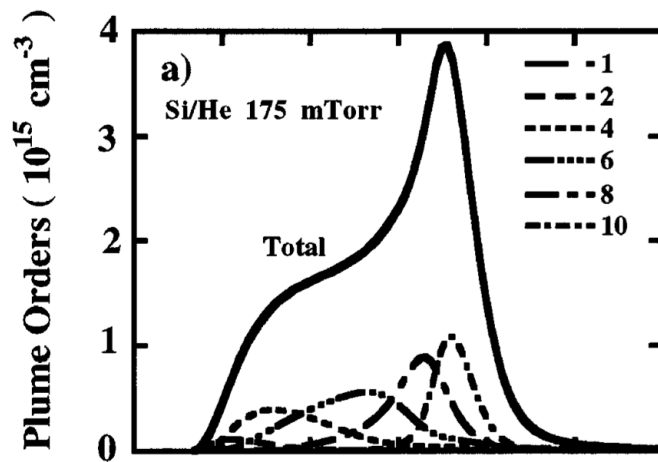
"Snowplowing" of background gas
– Si and He densities passing different
distances through 175 mTorr He
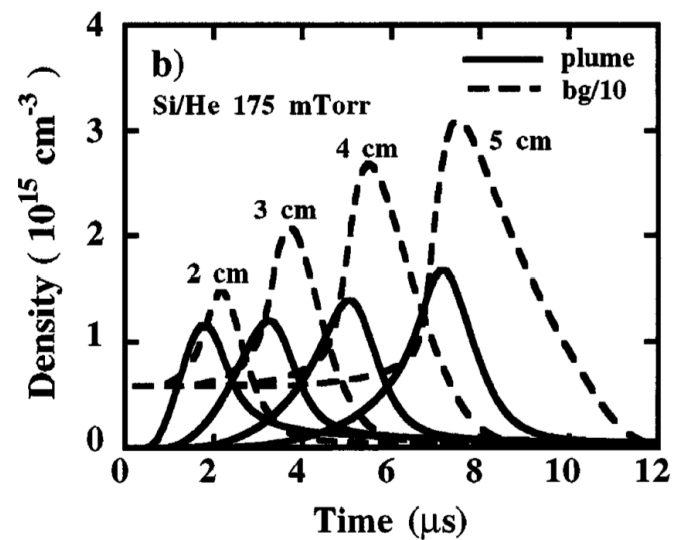
The entire model only relies upon one fit parameter, the scattering cross section, which is on the order of $\sigma \sim 3 \times 10^{-16}$ cm², which is ~ the atomic diameter.

R. F. Wood, K.R. Chen, J. N. Leboeuf, A. A. Puretzky and D. B. Geohegan, "Dynamics of Plume Propagation and Splitting during Pulsed Laser Deposition" *Phys. Rev. Letters 79(8), 1551 (1997).*
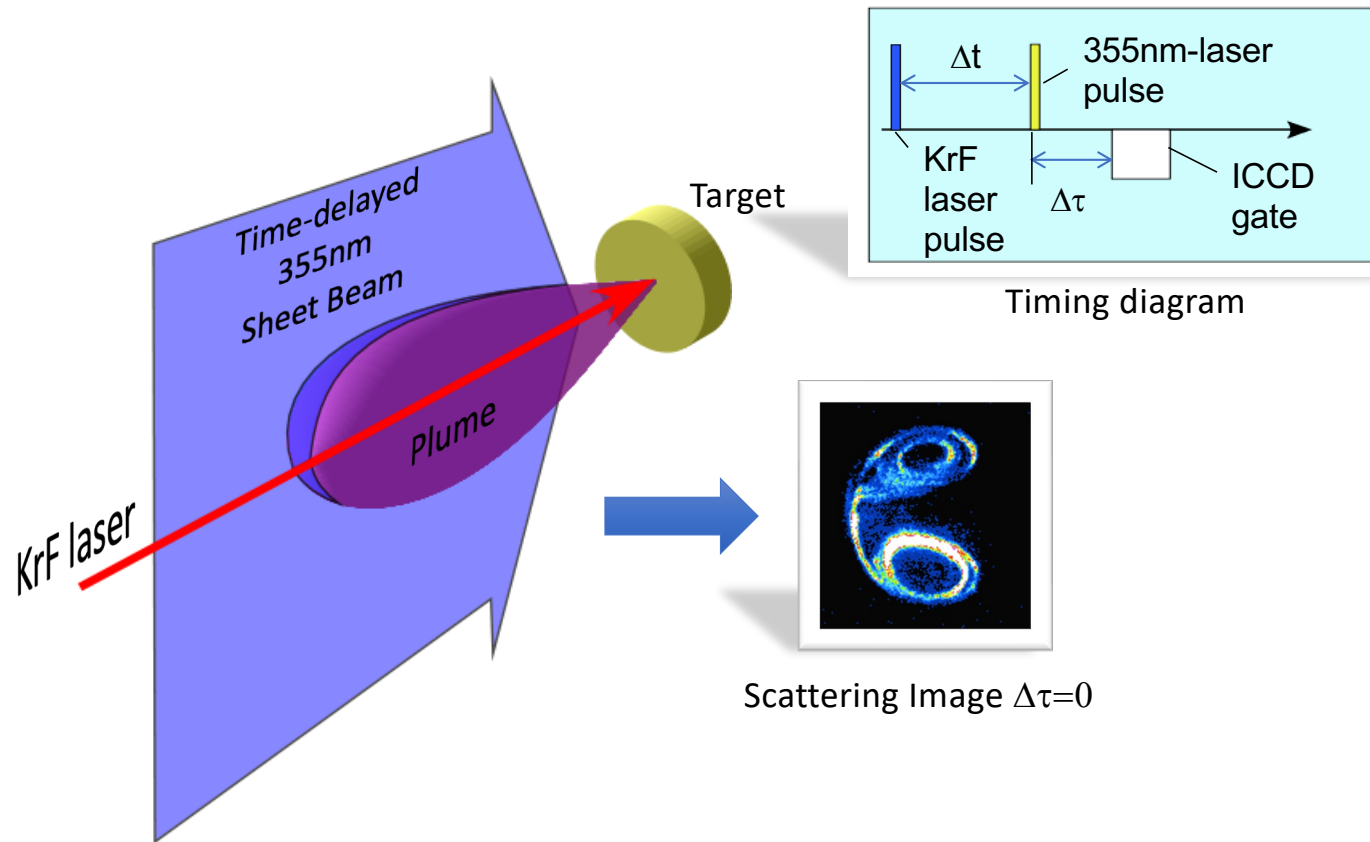
SLIMS 24   San Servolo

Imaging nanoparticle formation and propagation

via in situ photoluminescence and Rayleigh scattering

Beam Configuration for LIF/Rayleigh Scattering

Target

Time-delayed 355nm Sheet Beam

Plume

KrF laser

Δt 355nm-laser pulse

KrF laser pulse $\Delta\tau$ ICCD gate

Timing diagram

Scattering Image $\Delta\tau=0$

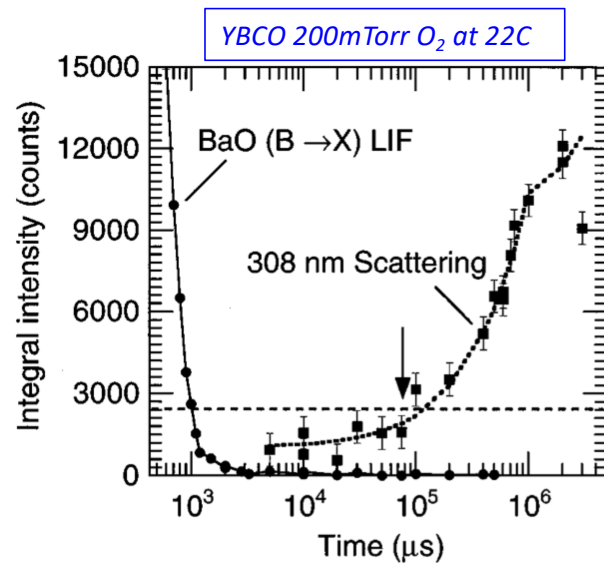# Nanoparticle Growth Under PLD Conditions: YBCO

Plasma luminescence, LIF from diatomic oxides, and Rayleigh Scattering from Nanoparticles
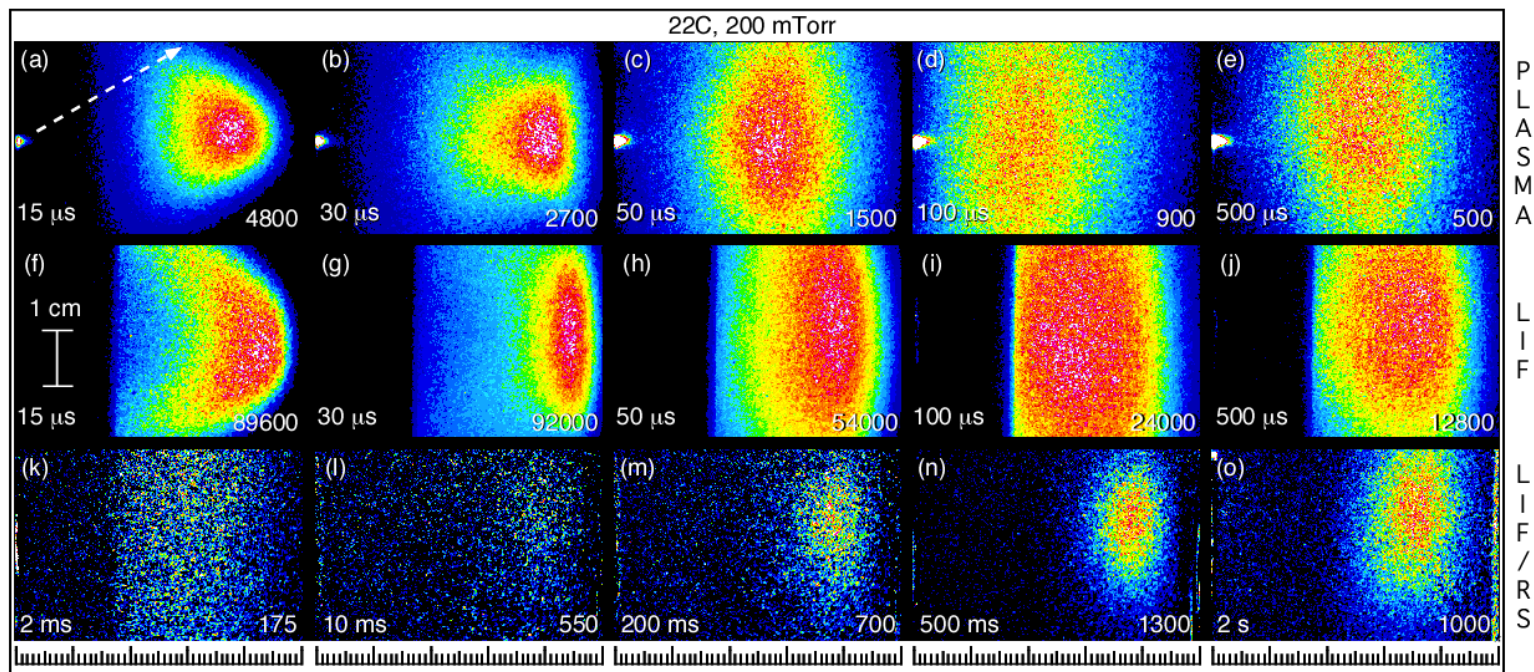
*D. B. Geohegan, A. A. Puretzky, and D. A. Rader, Appl. Phys. Lett. **74**, 3788 (1999).*

Timescales for Nanoparticle Growth from Oxide LIF and RS

YBCO 200mTorr O₂ at 22C

- Disappearance of oxide molecular bands from one to tens of milliseconds at 200mTorr O_2

- Emergence of scattering from aggregates of nanoparticles over 10 ms at pressures as low as 175 mTorr O_2

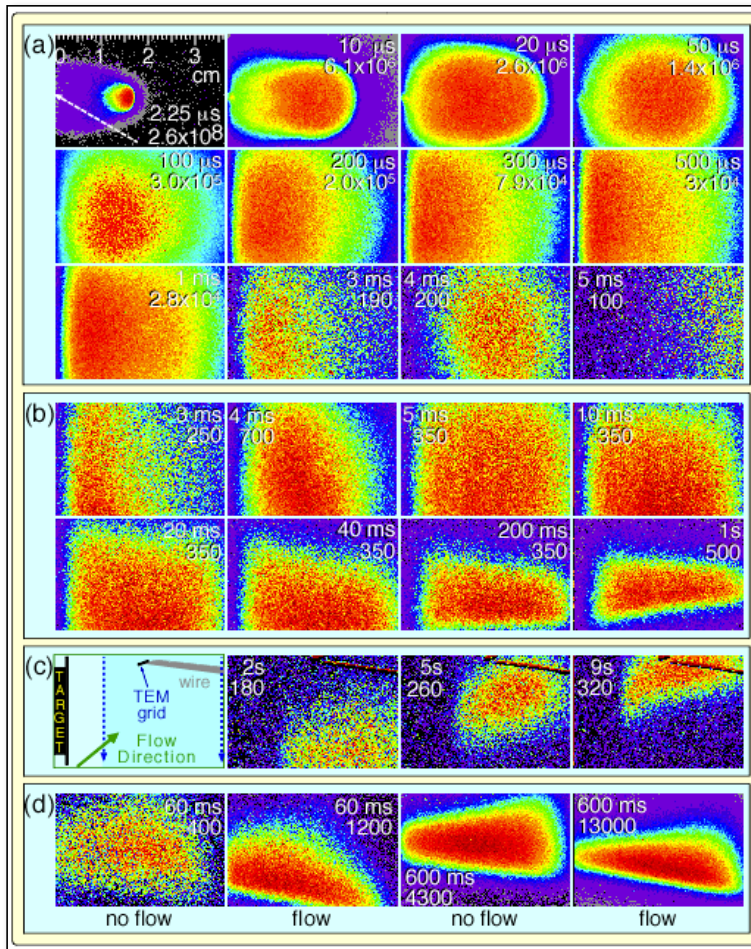- Pressure, fluence, and temperature dependent !

Can use spatial location and time dependence of oxide molecular bands to locate regions of nanoparticle formation

*D. B. Geohegan, A. A. Puretzky, and D. A. Rader, Appl. Phys. Lett. **74**, 3788 (1999).*

Photoluminescent Nanoparticles formed in Si/Ar (1 Torr)

(a) Plasma recombination-fed fluorescence (up to 5 ms)

(b) Laser-induced photoluminescence from SiO_x nanoparticles

(c) PL with weak flow

(d) RS w/ and w/o flow

Photoluminescent Nanoparticles formed in Si/He (10 Torr)

- Completely different dynamics with Si/He and Si/Ar

- $m_{Ar} > m_{Si} > m_{He}$

- 40 > 28 > 4

- Scattering from the beam stops Si in Ar, but leaves it moving turbulently forward in He

- The turbulence stirs in fresh gas to the nanoparticles in He, leading to oxidation of Si in He but not Ar

- External gas flow must be introduced in Ar to bring in background oxygen impurities

- Nanoparticles do not stick to the Si substrate.
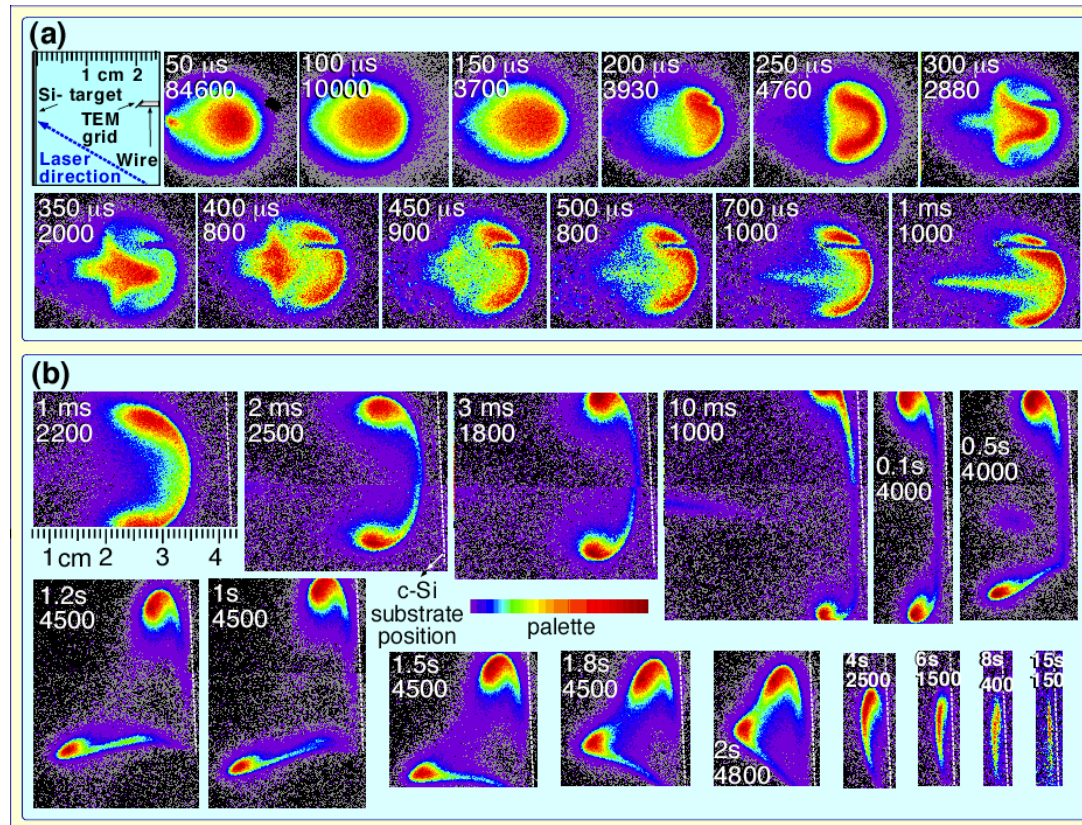
D. B. Geohegan, A. A. Puretzky, G. Duscher, and S. J. Pennycook, *Applied Physics Letters 72 (23), 2987-2989 (1998)* and *Applied Physics Letters* 73 (4), 438-440 (1998) .
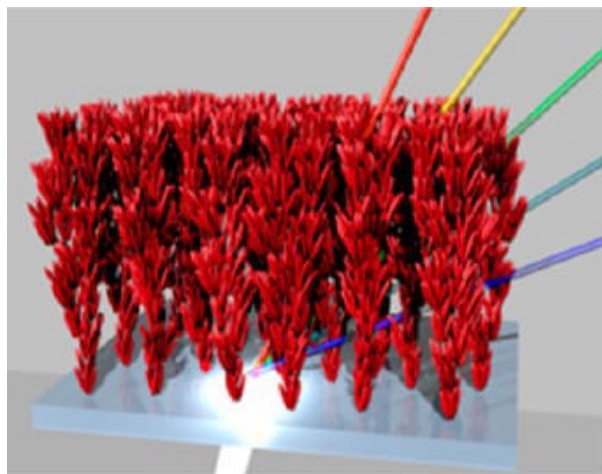
Hyperbranched or Hierarchical Nanostructures for Dye Sensitized Solar Cells

❖ Deposition of hierarchical UNP architectures at room temperature are being employed for a variety of applications
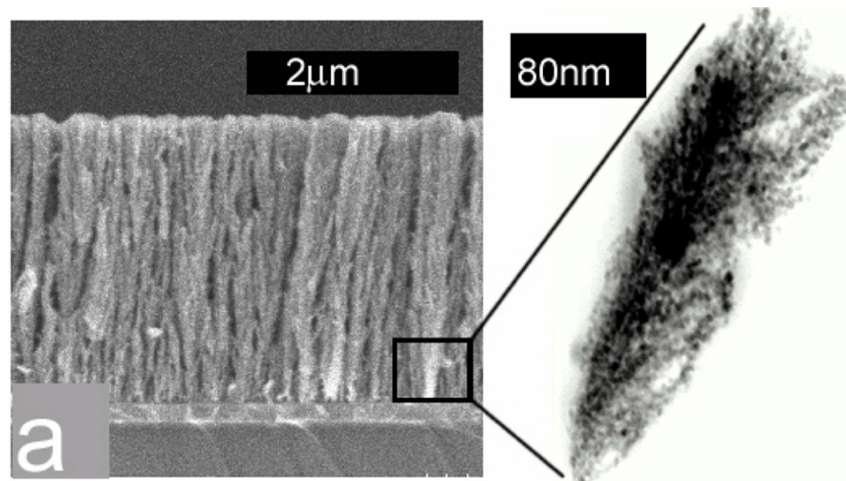
L. Passoni, F. Di Fonzo
PoliMi Istituto Italiano di Tecnologia, Milan

Rene Lopez
University of North Carolina

Al₂O₃: *Appl. Phys. A*, **93**, 765 (2008).
TiO2: *ACS Nano*, (2013, 2014).; *Nano Lett.* (2010).; *ACS App. Mat. Int.* (2015)
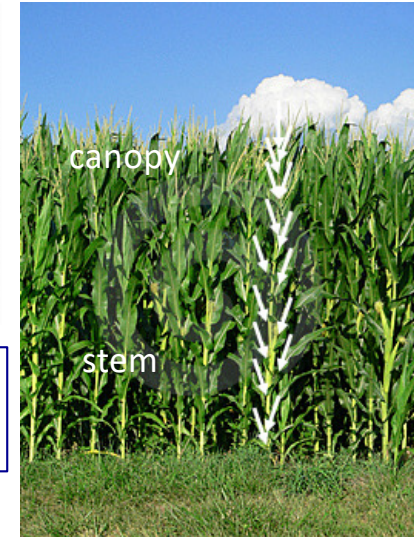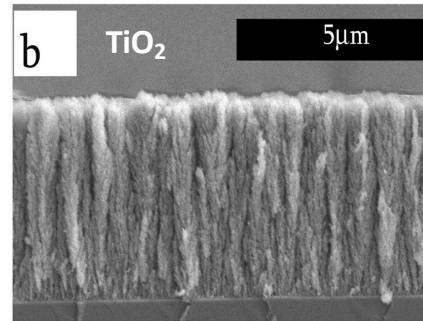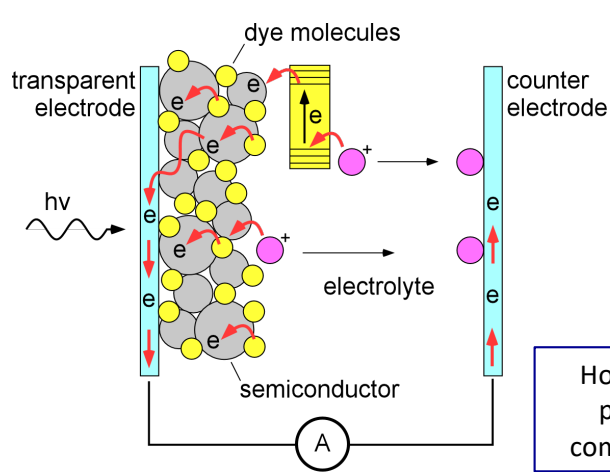**WO₃**: *J. Mat. Chem. A* (2015).

Ta:TiO2: *ACS Appl. Mater. Int.s* 4, 4566 (2012)
Nb2O5: *ACS Appl. Mater. Int.s* 3, 3929 (2011).

Understanding the synthesis of mesoporous nanoparticle architectures

dye molecules

transparent electrode

counter electrode

hv

electrolyte

semiconductor

A

b   TiO₂   5μm

How do nanoparticles formed in the plume deposit and sinter to form complex architectures on substrates ?

(courtesy Rene Lopez)

canopy

stem

- Their porosity, sintering, and architectures are sensitively dependent on the plume spatial confinement, kinetic energy, deposition distance and rate.

b
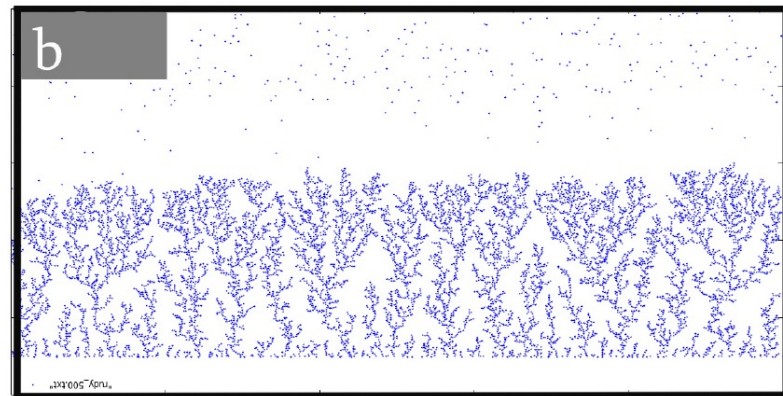
Sintering of as-deposited nanoparticles to form crystalline, hyperbranched anatase TiO$_2$ anodes for dye sensitized solar cells with higher efficiency
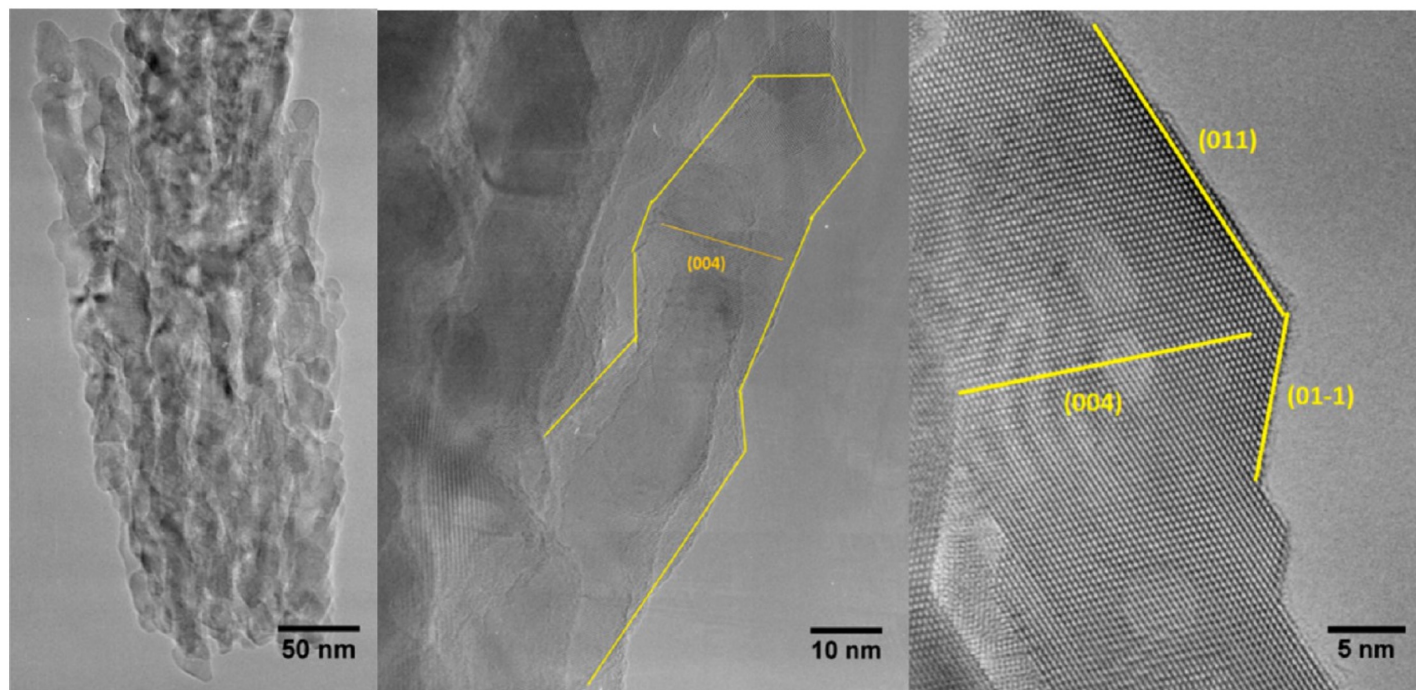

Figure 3. High-resolution TEM images of PLD deposited film at 7 Pa. Here it is possible to appreciate the hyperbranced structures (left-hand side and center), the single crystals with (011)-type surface terminations, and sets of (004) planes running perpendicular to the branch (right-hand side) seen along the [100] zone axis.

L. Passoni,…, F. Di Fonzo "Hyperbranched Quasi-1D Nanostructures for Solid State Dye Sensitized Solar Cells, *ACS Nano* **7**, 10023 (2013).*
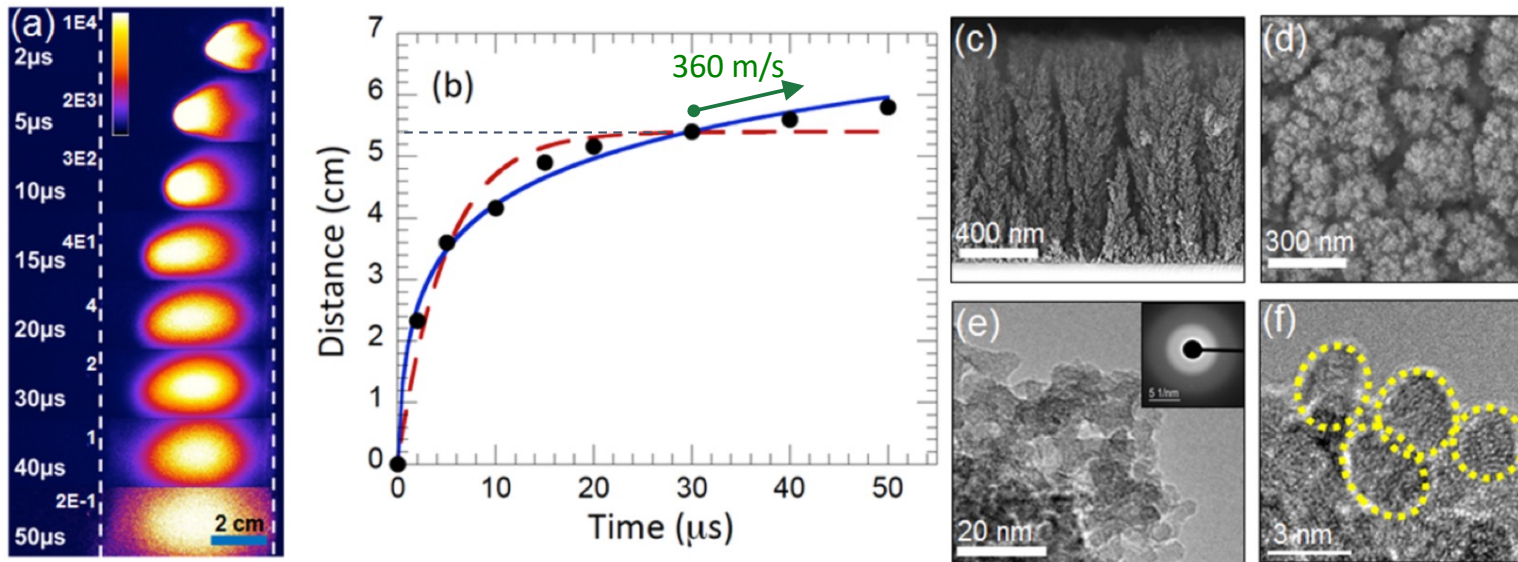
Emergence of "pure" nanoparticle architectures in PLD – *signaled by ion probe flux "plume splitting"*
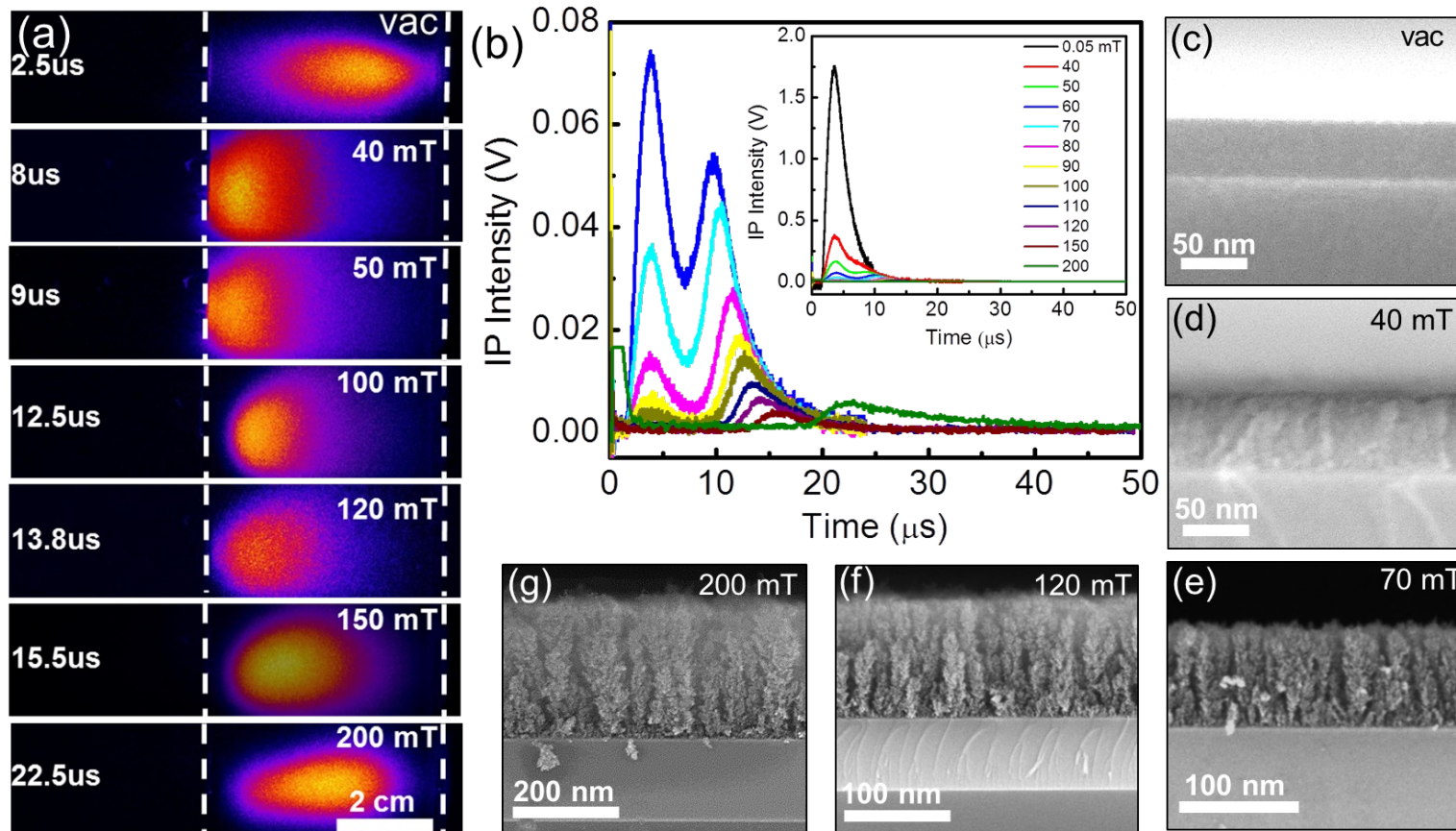
M. Mahjouri-Samani, et al., *Nano Letters* **17**(8) 4264 (2017).

Deposition of nanoparticle architectures in PLD –
– beyond the plume "range"

360 m/s

n = 1: linear drag

$a = -\beta v$

$R = (v_0 / \beta)(1 - \exp(-\beta t))$

Predicts plume stops at d = 5.4 cm

N = 2: quadratic drag

$a = -\alpha v^2$

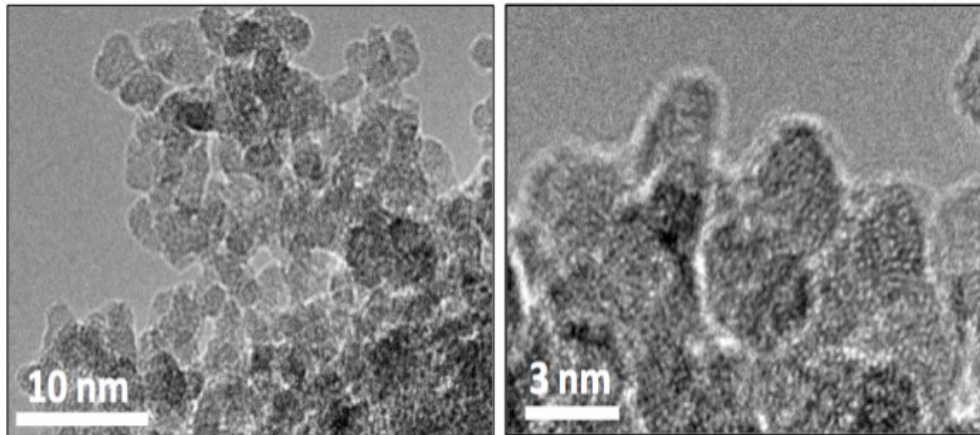$R = \alpha^{-1} \ln(1 + \alpha v_0 t)$

Plume velocity at d = 5.4 cm is 360 m/s

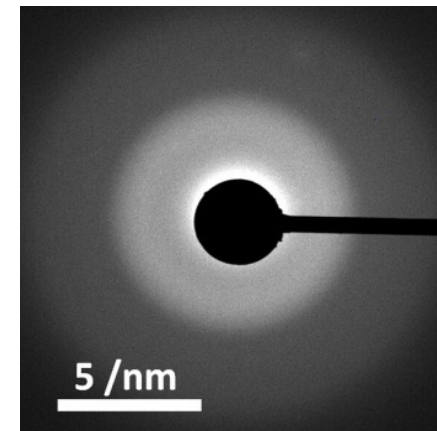Nanoparticle films deposited within diffusive transport region

M. Mahjouri-Samani, et al., *Nano Letters* **17**(8) 4264 (2017).
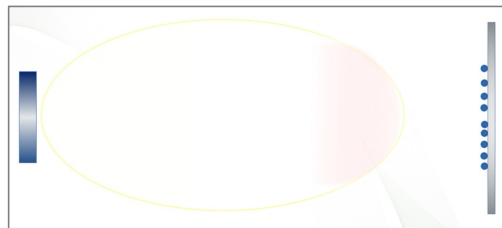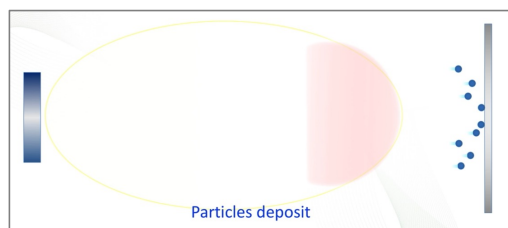
TiO₂ Ultrasmall Nanoparticles

High resolution TEM

Selected-area electron diffraction (SAED)
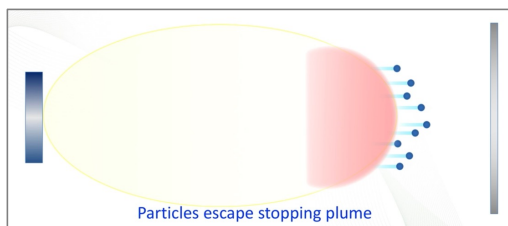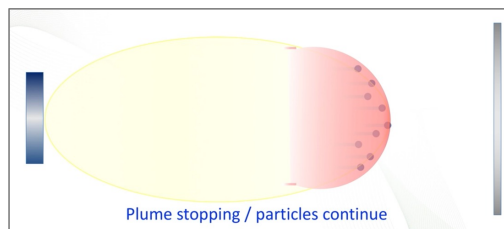

3-5 nm UNPs formed in 200 mTorr oxygen by ablation of TiO₂ targets are stoichiometric according to EELS but amorphous according to SAED

Animation: Nanoparticle PLD (NPLD) Dynamics

Laser Ablation

Background gas interactions / shock formation / nucleation

Particles form as plume slows

Plume stopping / particles continue

Particles escape stopping plume

Particles slow at extended range
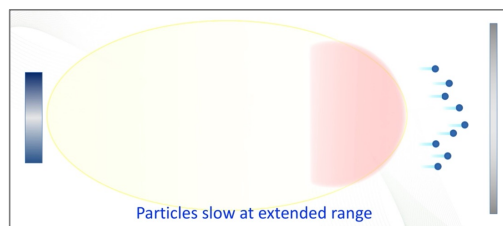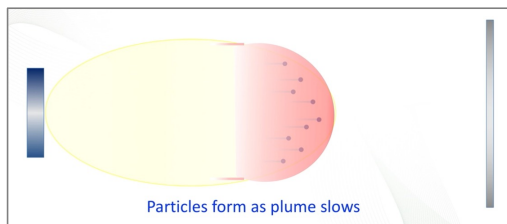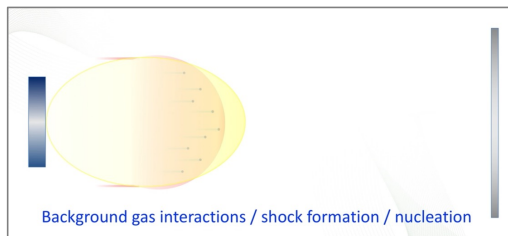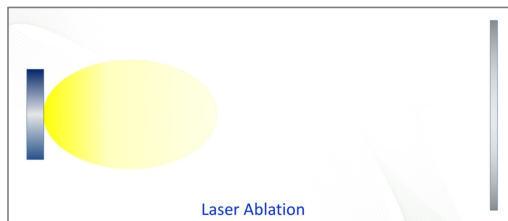
Particles deposit

Ultrasmall 'amorphous' oxide UNPs as 'building blocks' of crystalline nanostructures
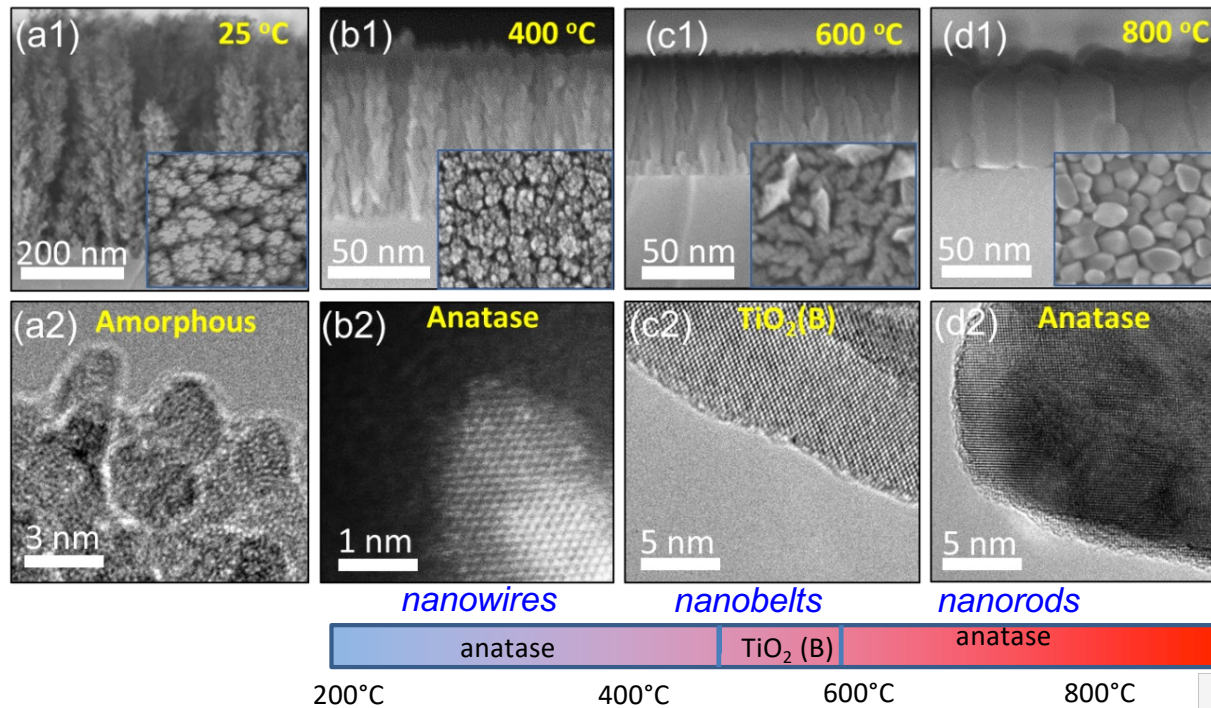
Ultrasmall 'amorphous' TiO_2 nanoparticles transform into metastable phases and different morphologies at different deposition rates and substrate temperatures.

- Catalyst-free
- Similar phenomena for other oxides (e.g., MgO, PZT, ...)

M. Mahjouri-Samani, et al., *Nano Letters* **17**(8) 4264 (2017).

Metastability of UNPs

Ostwald's Rule of Stages
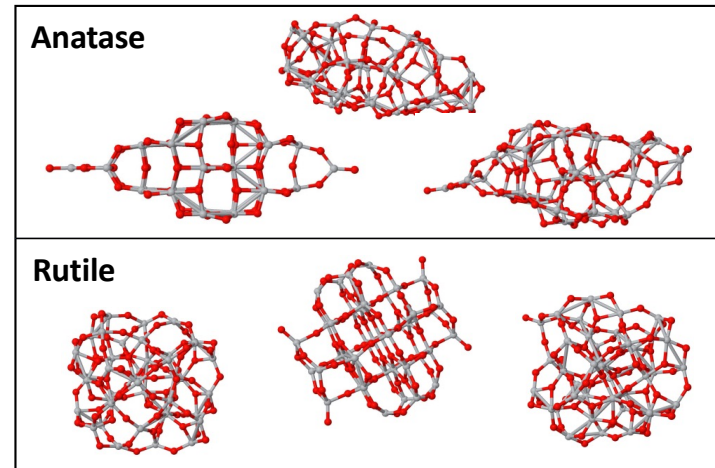
ΔG_1^* ΔG_2^* ΔG_3^* ΔG_4^*

Amorphous

A

B

C

Free energy

ΔG

Stable crystal

Nature Physics, **5**, 68 (2009).

Structure (or reaction time)

Anatase

Rutile
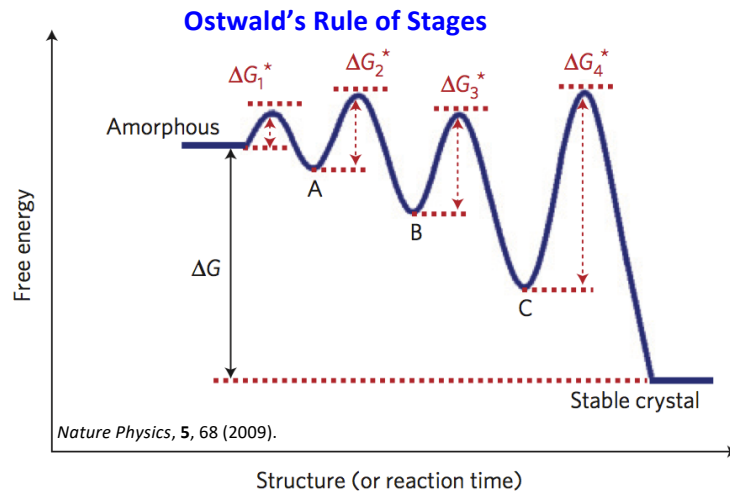
Hypothesis

- Ultrasmall amorphous nanoparticles are metastable
- Crystallization occurs through a series of intermediate (metastable) states separated by small changes in free energy.

Oriented Attachment – *or Templating*
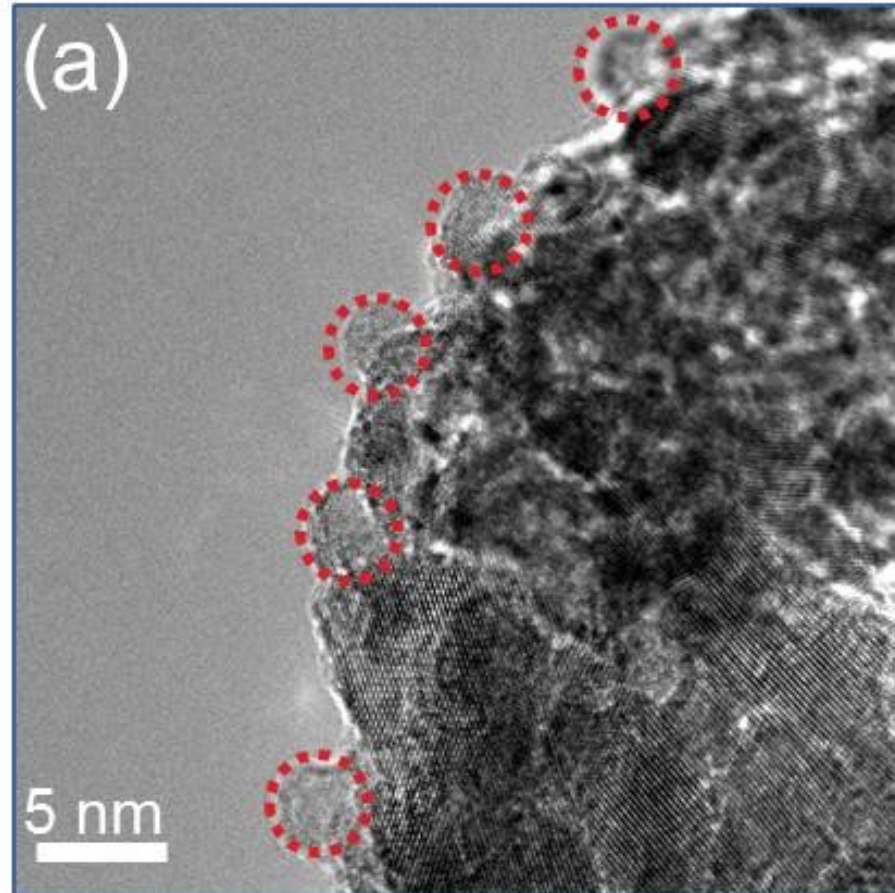
Oriented Attachment – *or Templating*

Z-STEM - aberration corrected Z-contrast scanning transmission electron microscopy

Anatase view in [100]
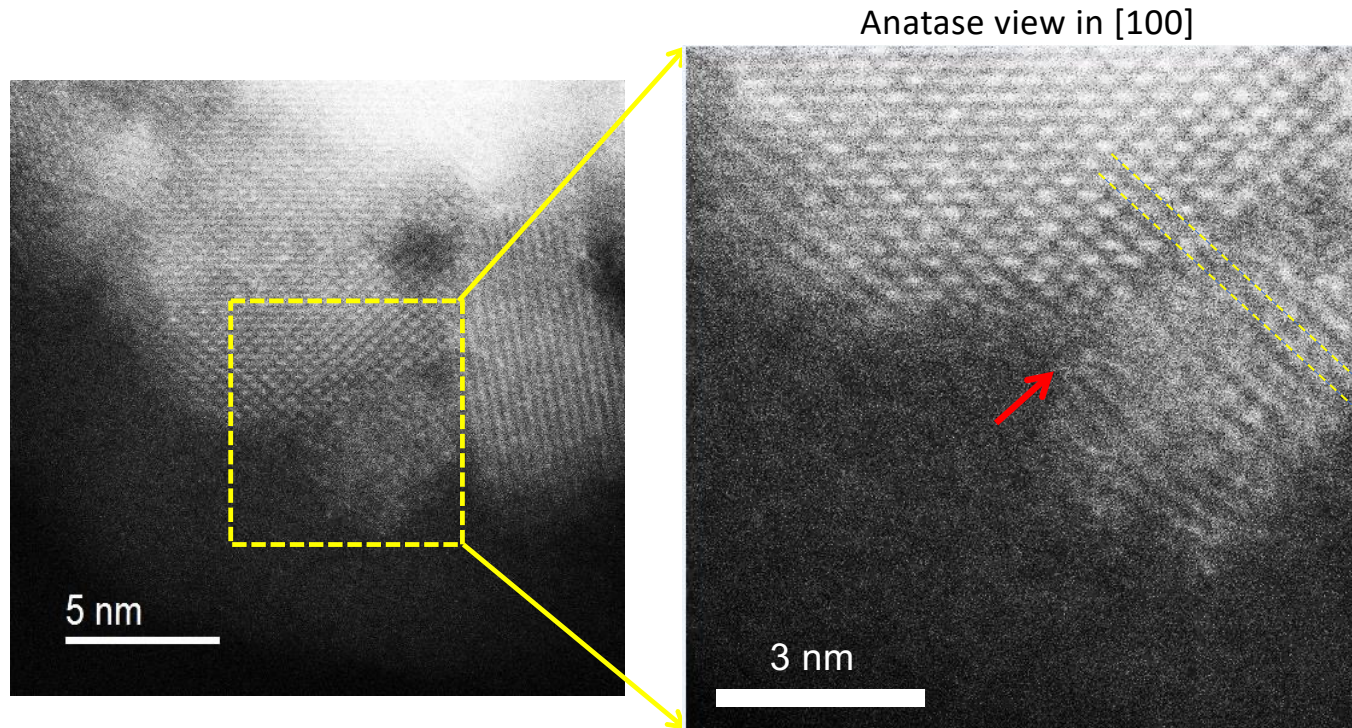
Nanoparticle crystal axis alignment appears to be templating from, or aligning with, base crystal.

Crystallization by Particle Attachment
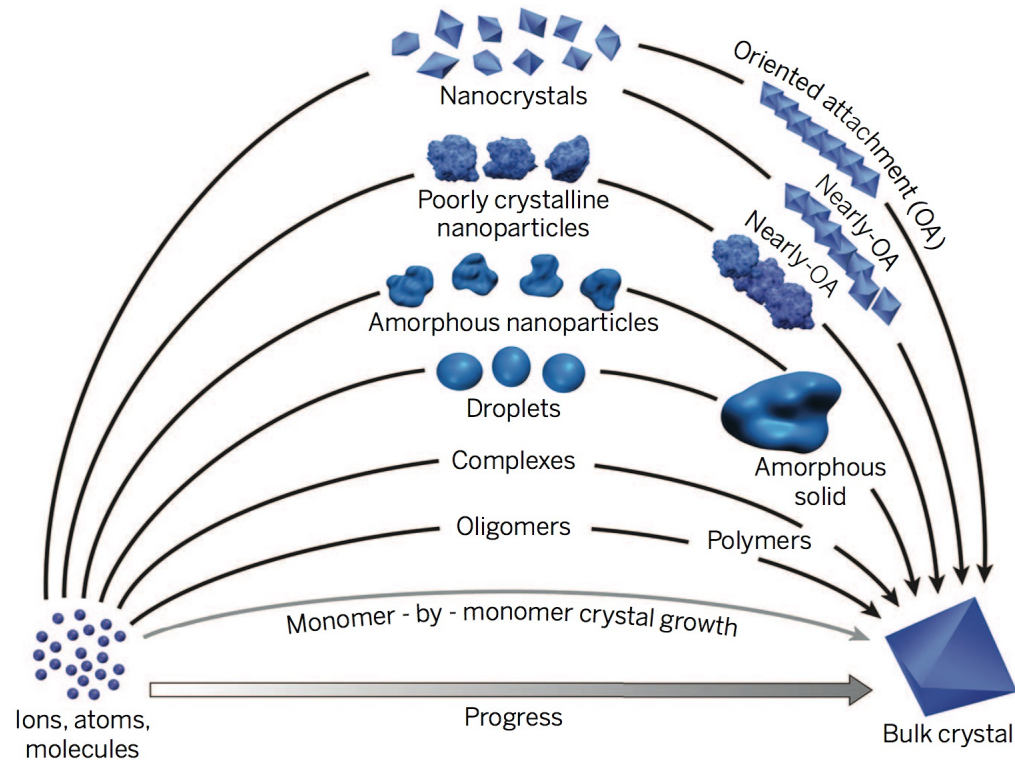
Fig. 1. Pathways to crystallization by particle attachment. In contrast to monomer-by-monomer addition as envisioned in classical models of crystal growth (gray curve), CPA occurs by the addition of higher-order species ranging from multi-ion complexes to fully formed nanocrystals. (The final faceted bulk crystal is a schematic representation of a final single-crystal state. As Figs. 2 and 3 show, the final crystal can have more complex morphologies, including spheroidal.)

J. J. De Yoreo et al., *Science* **349** (6247) (2015).

Dry Printing and Additive Manufacturing of Flexible Hybrid Electronics and Sensors

Z. Ahmani, …, **M. Mahjouri-Samani**, *Adv. Mater. Interfaces, 9, 2012569 (2022).*

Figure 1. a) Schematic illustration of ANM process for dry printing Ag and ITO on flexible substrates. b,c) A 2 × 2 cm² printed Ag NFC tag antenna (four loops with a total length of ≈32 cm and ≈1.38 Ω cm resistance) connected to a self-power M24LR04E IC enabling communication with a phone device. d) Printed FHEs circuit on the polyimide substrate.
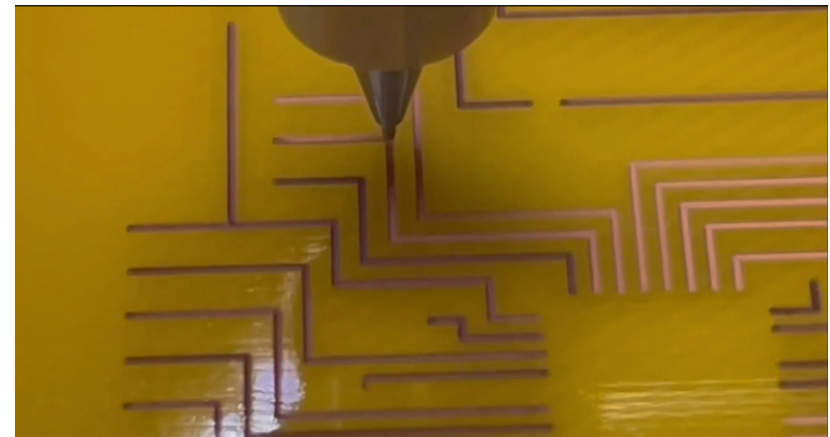
- Gas-phase nanoparticle synthesis

- Extraction through nozzle / printing head / X-Y

- Laser Sintered directly on paper, polymers, etc.

  - Clean, surfactant-free, dry, for interconnects, sensors, antennas, etc.

The ultimate PLD challenge: Atomically-thin 2D materials

Assembling and ion/laser interactions with
'van der Waals' monolayers

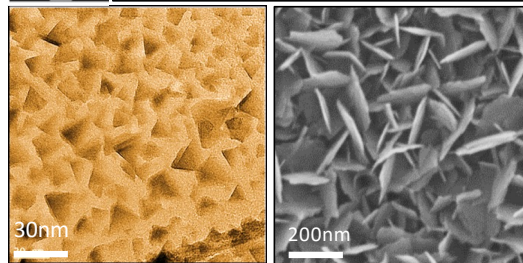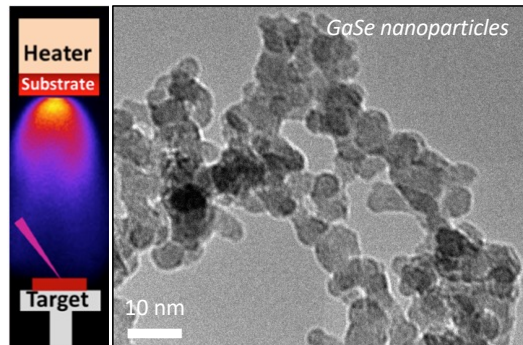### *Controlling KE ~ 10 eV - A very difficult regime*

Ultrasmall amorphous nanoparticles as building blocks of 2D metal chalcogenide crystals – *bottom up*
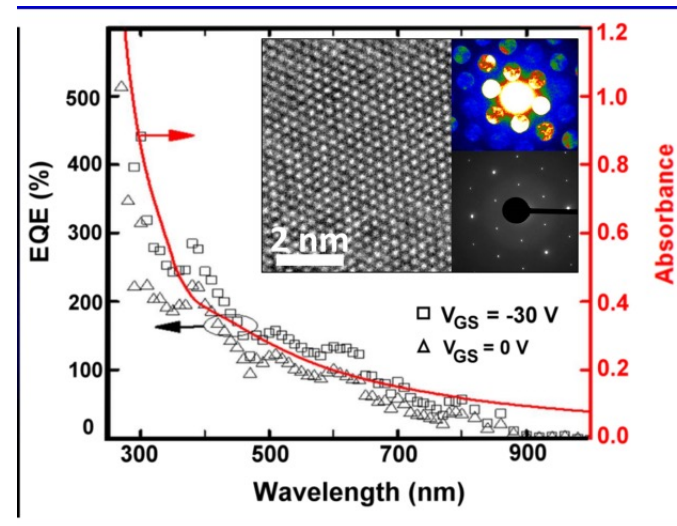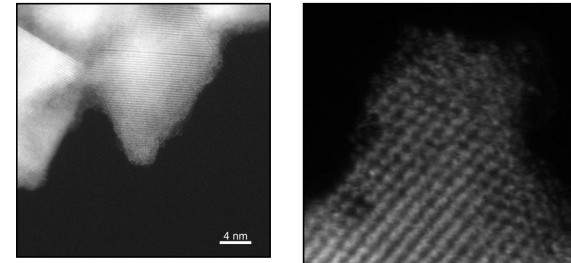
stoichiometric transfer due to nanoparticle 'building blocks'

GaSe and MoSe$_2$

orientation controlled by deposition rate and substrate temperature

First direct PLD of 2D materials as nanosheets -surprisingly under conditions for nanoparticle formation
*3D -> 2D growth process ?*

Stoichiometry – direct deposition

Mahjouri-Samani, et al., *Adv. Func. Mat.* **24**, 6365 (2014).

Digital Transfer Growth of Patterned 2D Metal Chalcogenides
– *bottom up*

- These same nanoparticles can be used as feedstock to grow much larger 2D single crystals in a novel "digital transfer growth" technique

- Room temperature PLD of nanoparticles onto *source* substrate

- Heated between two substrates, 2D crystals grow in prepatterned locations on a nearby *receiver* substrate
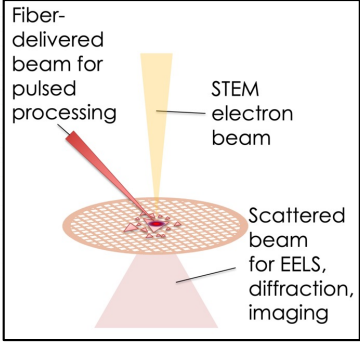
- "Digital" control of layer number via PLD
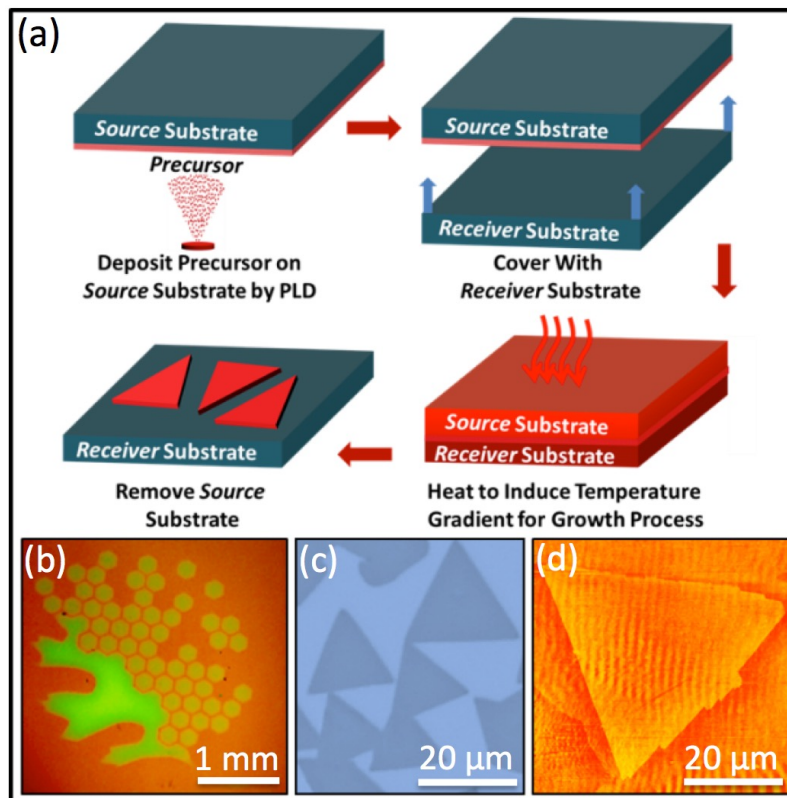
Stoichiometry – pre-patterning, thermal annealing, and transfer process

Mahjouri-Samani, et al., *ACS Nano 8(11),* 11567 (2014).

3 *in situ* diagnostic-based setups can be used to 'watch' materials assemble, at 3 different length scales

Atomistic/nanoscale

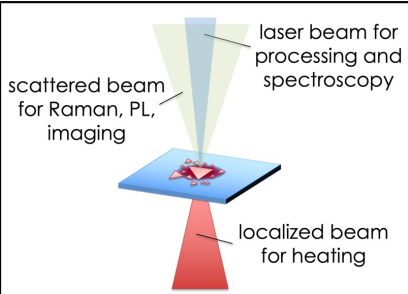Fiber-delivered beam for pulsed processing

STEM electron beam

Scattered beam for EELS, diffraction, imaging

Electron microscopy w/laser/optical

Nucleation, and early stages of crystal growth

Microscale

laser beam for processing and spectroscopy

scattered beam for Raman, PL, imaging
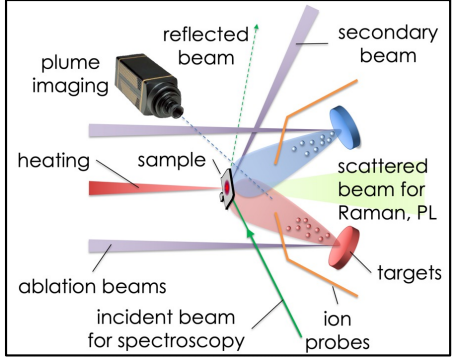
localized beam for heating

Optical spectroscopy microchamber

Large domain single crystal growth and defects

Macroscale

reflected beam

secondary beam

plume imaging

heating

sample

scattered beam for Raman, PL

ablation beams

incident beam for spectroscopy

ion probes

targets

Optical spectroscopy PLD

Wafer scale single crystal growth, and vdW heterostructures

PLD of 2D Heterostructures and van der Waals Epitaxy
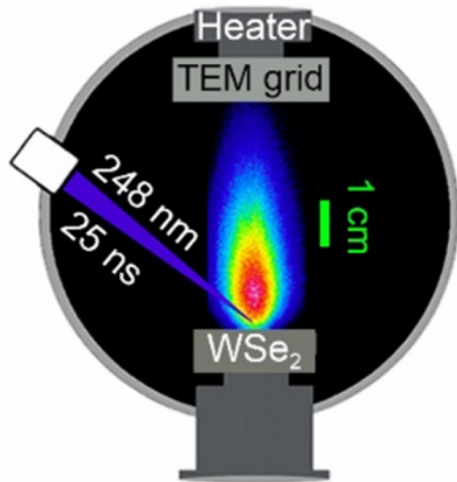
PLD of WSe$_2$ onto 2D monolayer substrates at 600°C to grow 2D heterostructures

Graphene: Lattice mismatched – polycrystalline small domain

Lattice matched – large aligned grains

- Crystallization despite the vdW gap = vdW epitaxy

- Works despite a large variation in the size of precursors

- Domain matching to form large grains – how?
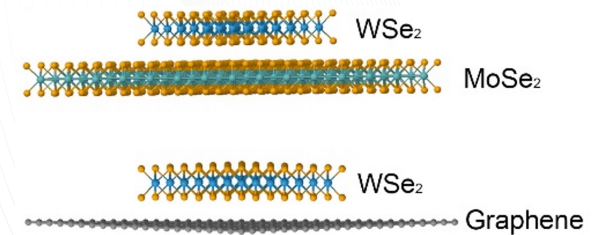
Laser processing within the TEM to watch PLD "building blocks" assemble via pulsed heating

Using the same precursors deposited by PLD, we can rapidly explore different crystallization pathways. Can we understand how films assemble in PLD?

- Precursors: Amorphous for ~ 1-2 ML quantity, various sizes
- Pulsed heating
- Stoichiometry measured by EELS
- Crystallinity from HAADF imaging and SAED
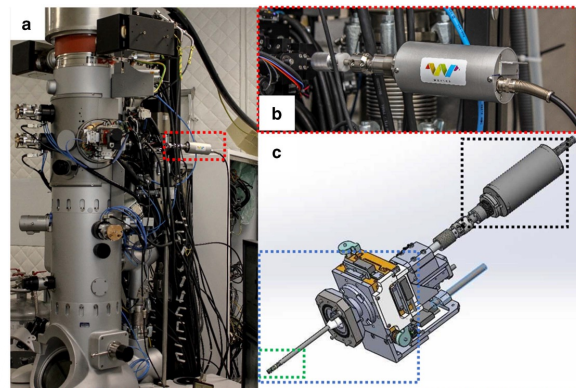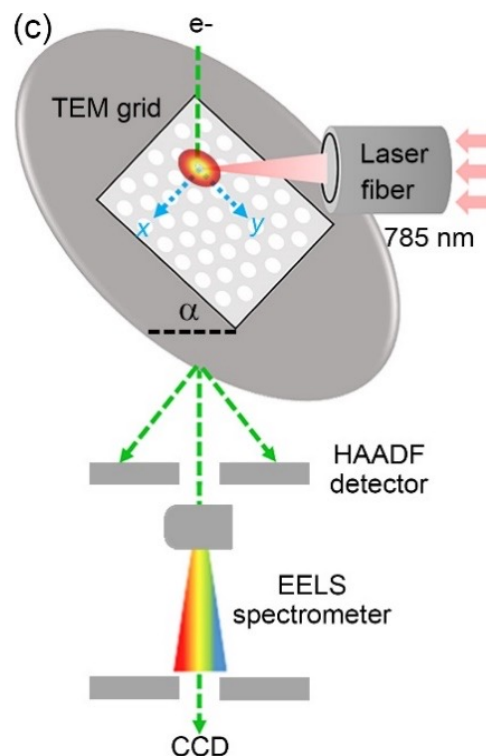
Laser wavelengths: 785nm and 450 nm
Peak power: >200mW
Fiber diameter: 5 µm
laser pulse width: from a few ns to CW
repetition rates: up to 16 MHz.

Crystallization of WSe$_2$ precursor on MoSe$_2$

as deposited   9.2mW   13.5 mW

SAED

STEM

(a)

CA

MA

R

GBM

(b)
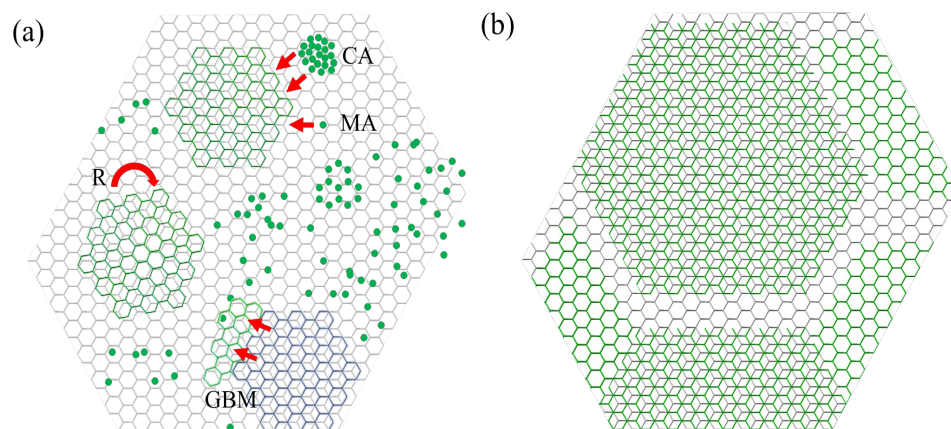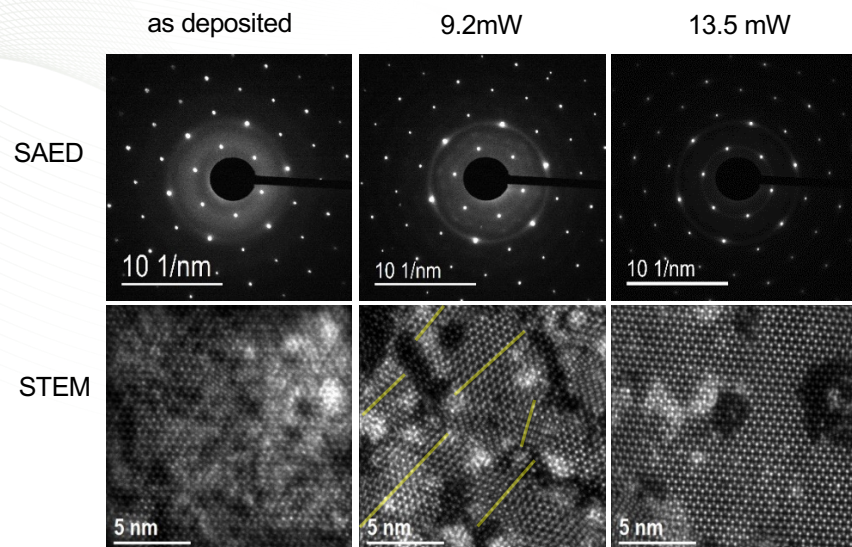
Crystallization by particle attachment in 2D

- Crystallizes into 2D flakes as stoichiometry evolves
- Flakes rotate to align with substrates !
- …facilitating sintering to form large aligned crystals
- Crystallization by particle attachment in 2D.

- First principles calculations reveal a strong driving force for alignment

- In situ laser crystallization in the TEM allows a variety of phenomena and processing conditions to be revealed and optimized

Pulsed laser deposition of S to replace Se in $MoSe_2$ to form MoS_2

Using the kinetic energy and digital control of pulsed laser plasmas to dope, alloy, and convert 2D crystals
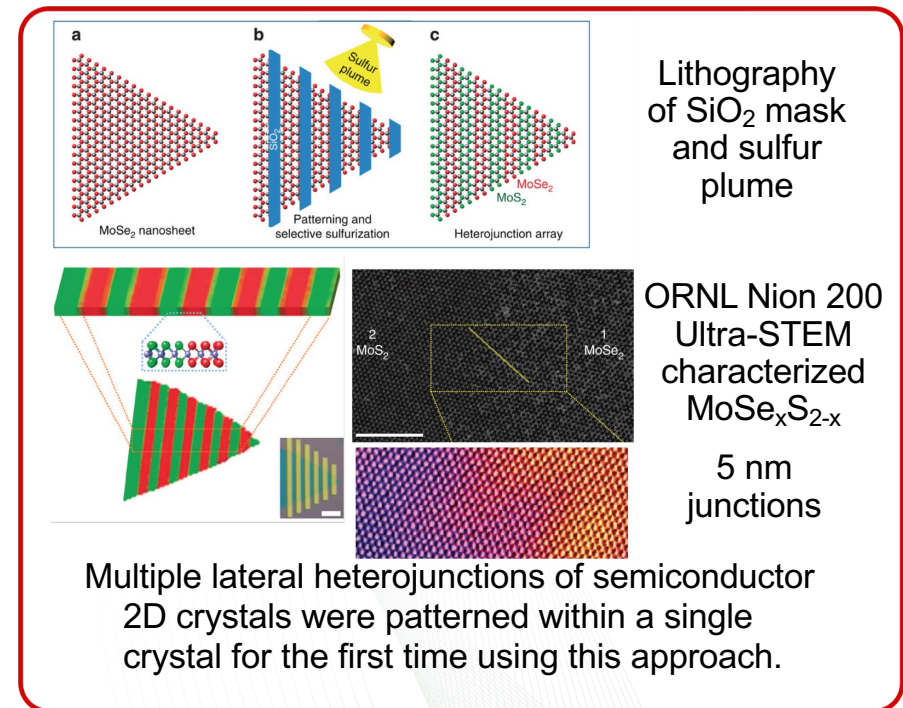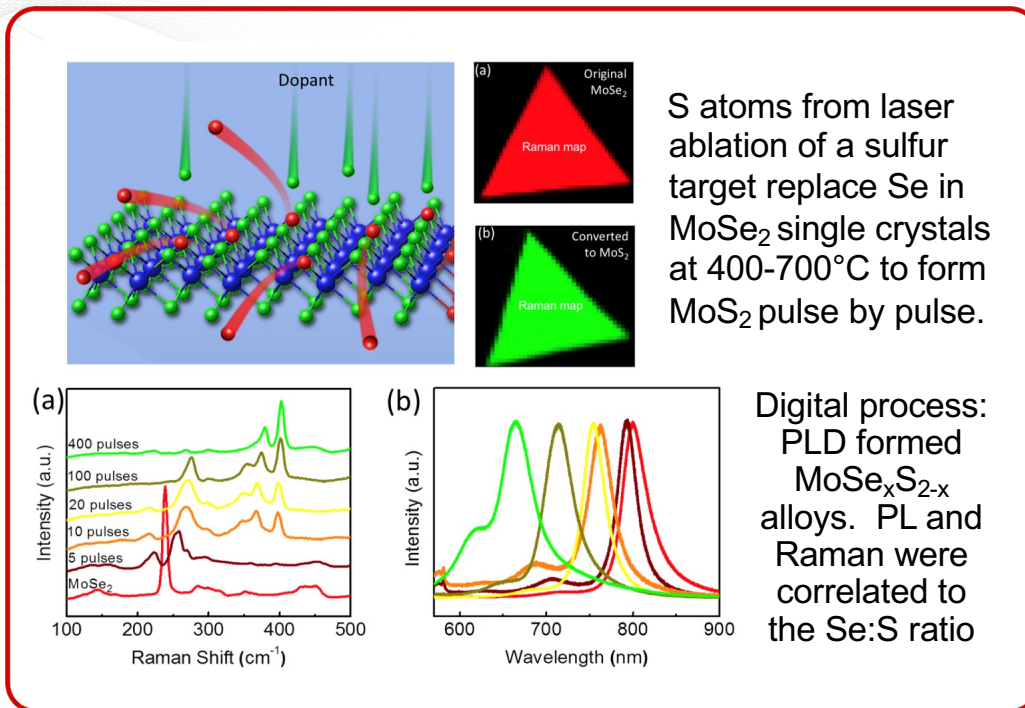

S atoms from laser ablation of a sulfur target replace Se in $MoSe_2$ single crystals at 400-700°C to form MoS_2 pulse by pulse.

Digital process: PLD formed $MoSe_xS_{2-x}$ alloys. PL and Raman were correlated to the Se:S ratio

Lithography of SiO_2 mask and sulfur plume

ORNL Nion 200 Ultra-STEM characterized $MoSe_xS_{2-x}$

5 nm junctions

Multiple lateral heterojunctions of semiconductor 2D crystals were patterned within a single crystal for the first time using this approach.

Patterned arrays of lateral heterojunctions within monolayer two-dimensional semiconductors M. Mahjouri-Samani, M.-W. Lin, K. Wang, A. R. Lupini, J. Lee, L. Basile, A. Boulesbaa, C. M. Rouleau, A. A Puretzky, I. N. Ivanov, K. Xiao, M. Yoon, D. B Geohegan, *Nature Comm.* **6,** 7749 (2015).

# Pulsed laser deposition of S to replace Se in MoSe$_2$ to form MoS$_2$

Using the kinetic energy and digital control of pulsed laser plasmas to dope, alloy, and convert 2D crystals

Two-Dimensional Heterostructure Materials U.S. Patent 9,964,846 B2 Geohegan, et al., (2018).

Patterned arrays of lateral heterojunctions within monolayer two-dimensional semiconductors M. Mahjouri-Samani, M.-W. Lin, K. Wang, A. R. Lupini, J. Lee, L. Basile, A. Boulesbaa, C. M. Rouleau, A. A Puretzky, I. N. Ivanov, K. Xiao, M. Yoon, D. B Geohegan, *Nature Comm.* **6,** 7749 (2015).

Janus monolayers of transition metal dichalcogenides
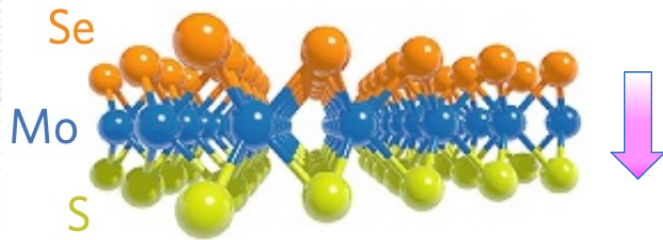
Janus Monolayers of Transition Metal Dichalcogenides
Lu et al., *Nat. Nanotechnol.* **12**(8), 744 (2017).

- Different chalcogens on either side of metal
  - Broken inversion symmetry
  - Built-in dipole fields
    - Rashba spin-orbit splitting for spintronics and quantum devices.
    - High optical absorption

- Wide range of predicted electronic, mechanical, structural properties in over 260 structures calculated:
  - Piezoelectricity
  - Ferromagnetism at RT (e.g., VSSe)

PLD is a highly effective, single-step method to form Janus monolayers at low temperatures

- Faster exciton formation
- Radiative recombination lifetime extended

Excitonic Dynamics in Janus MoSSe and WSSe Monolayers, T. Zheng, Y.C. Lin, P. Valencia-Acuna, A. Puretzky, R. Torsi, C. Liu, I.N. Ivanov, G. Duscher, D. B. Geohegan, Z. Ni, K. Xiao, H. Zhao, *Nano Lett.* **21**, 937 (2021)

- Janus heterojunctions are type II
- Directional interlayer excitons / charge transfer !
- Important for photovoltaics, and photocatalysis

Janus Monolayers for Ultrafast and Directional Charge Transfer in Transition Metal Dichalcogenide Heterostructures T. Zheng, Y-C. Lin, N. Rafizadeh, D. B. Geohegan, Z. Ni, K. Xiao, and H. Zhao, *ACS Nano* **16**, 4197 (2022).
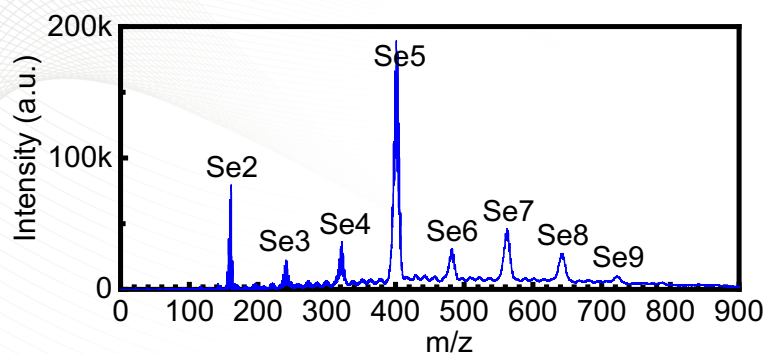
Exploring the unique advantages of laser plasmas for doping 2D materials –
Submonolayer implantation of WS_2 to form Janus WSSe monolayers

- Highly-forward directed beam of Se onto suspended ML WS_2 at low 250 - 500°C temperatures (evaporating excess Se)
  - $Se_2...Se_9$ clusters

- KE/Se atom tuned with background gas collisions via imaging and ion probe diagnostics
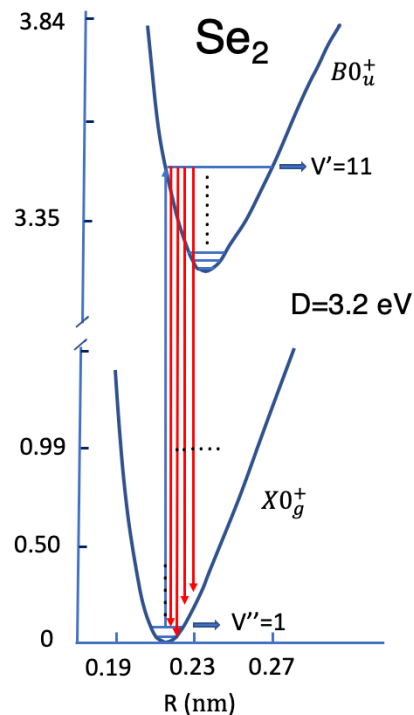 - A unique sub-10eV range with ease.

The typical KE's in PLD are perfectly tailored for controllable doping of 2D materials
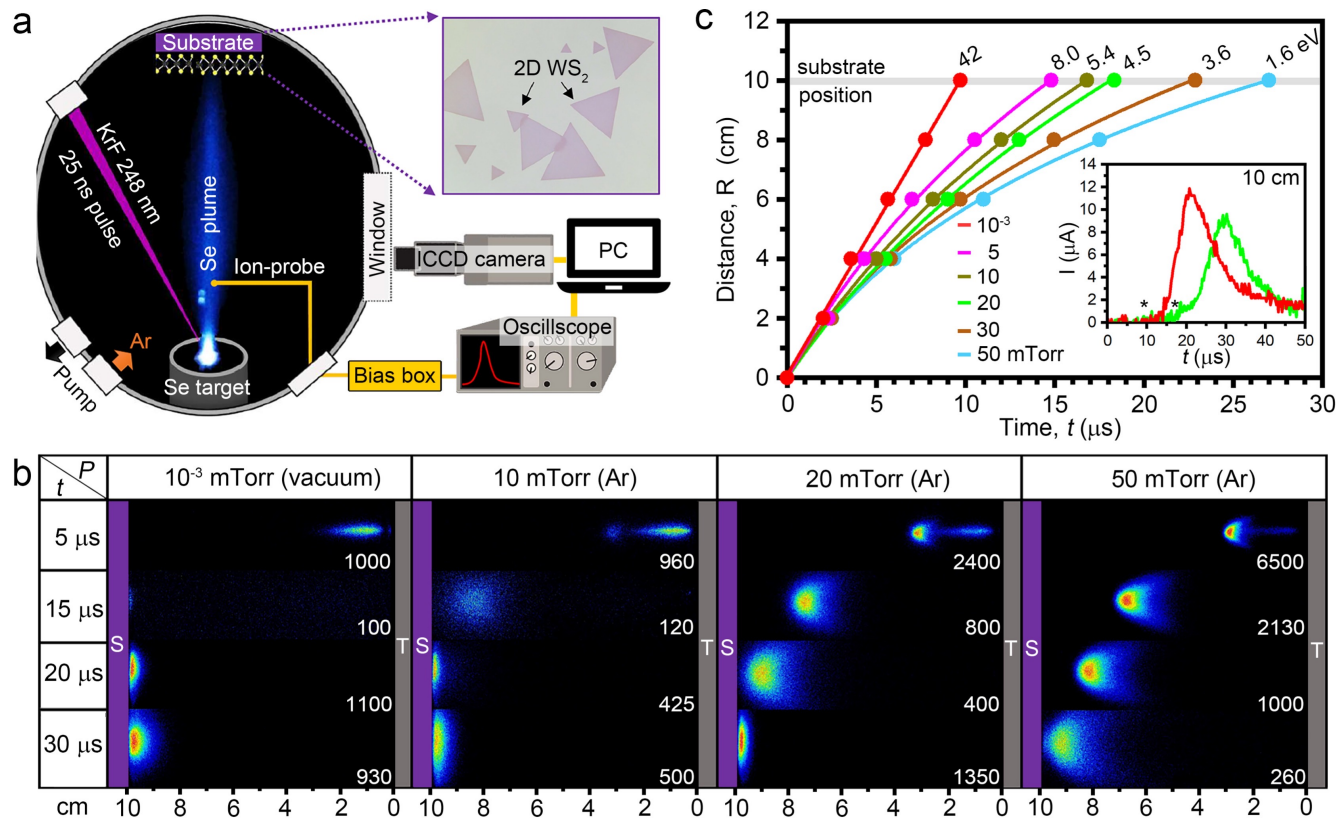
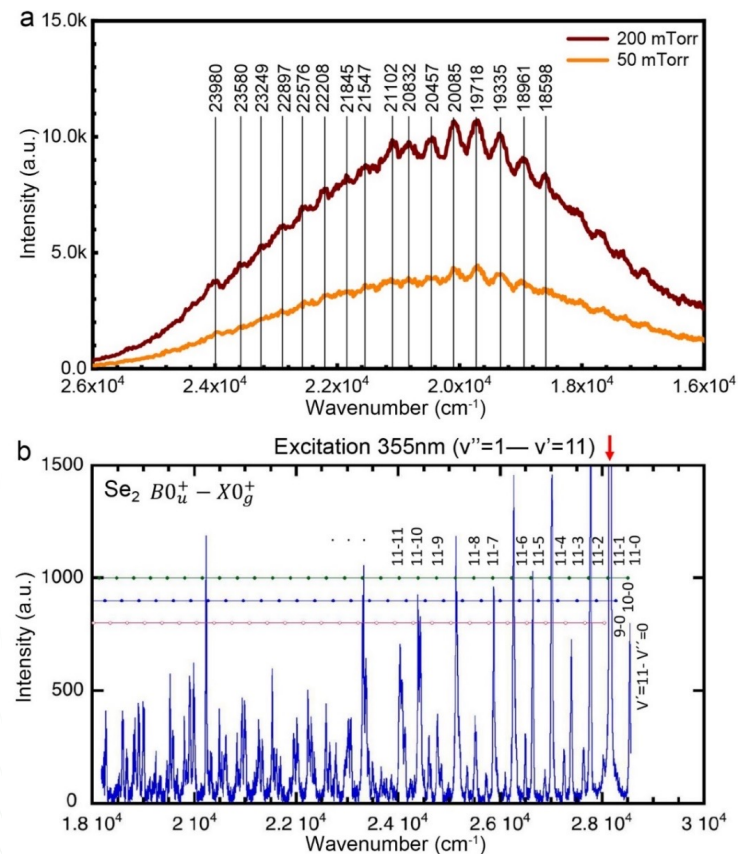# Se ablation – A most unusual plume of clusters – *MALDI, PL, and LIF*

Photoluminescence of Se plume in Ar (bright ball region)

- MALDI : principal ejecta are Se clusters

- Broad PL band exhibits vibronic peaks of Se_2 spaced ~ 50 meV apart.

- LIF of Se_2 ground state at 355nm selectively excites v' = 11 in $B0_u^+$ to confirm origin.

Se_n clusters comprise the bulk of the plume, and collisionally dissociate in Ar to form Se_2^* in the plasma

Y. C. Lin, C. Liu, et al., **Low Energy Implantation into Transition-Metal Dichalcogenide Monolayers to Form Janus Structures** *ACS Nano* **14**, 3896-3906 (2020)
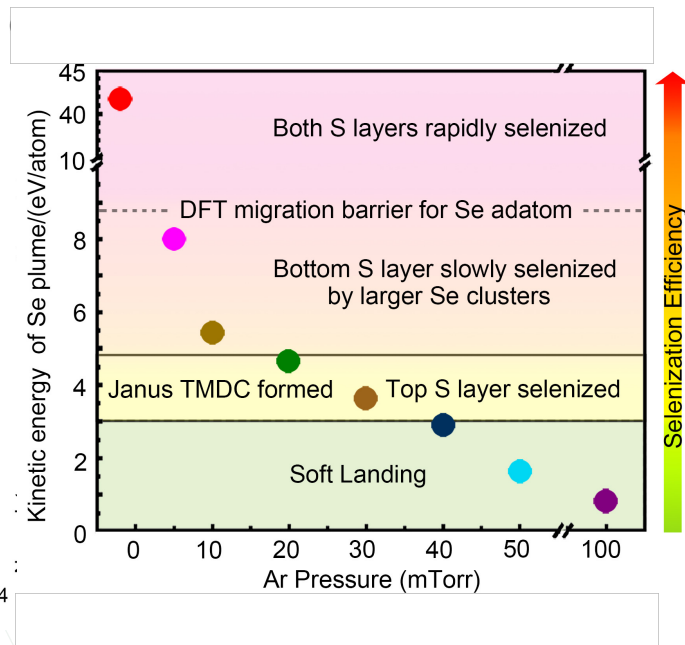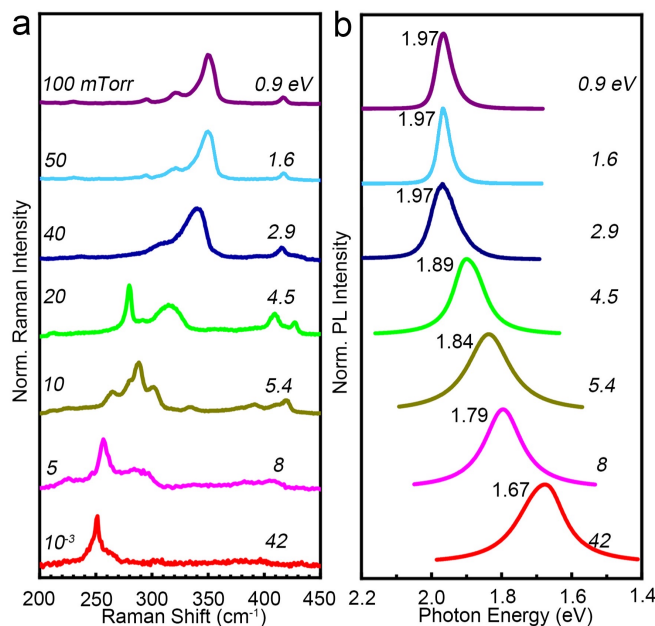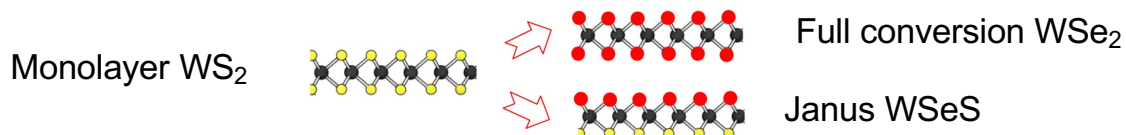
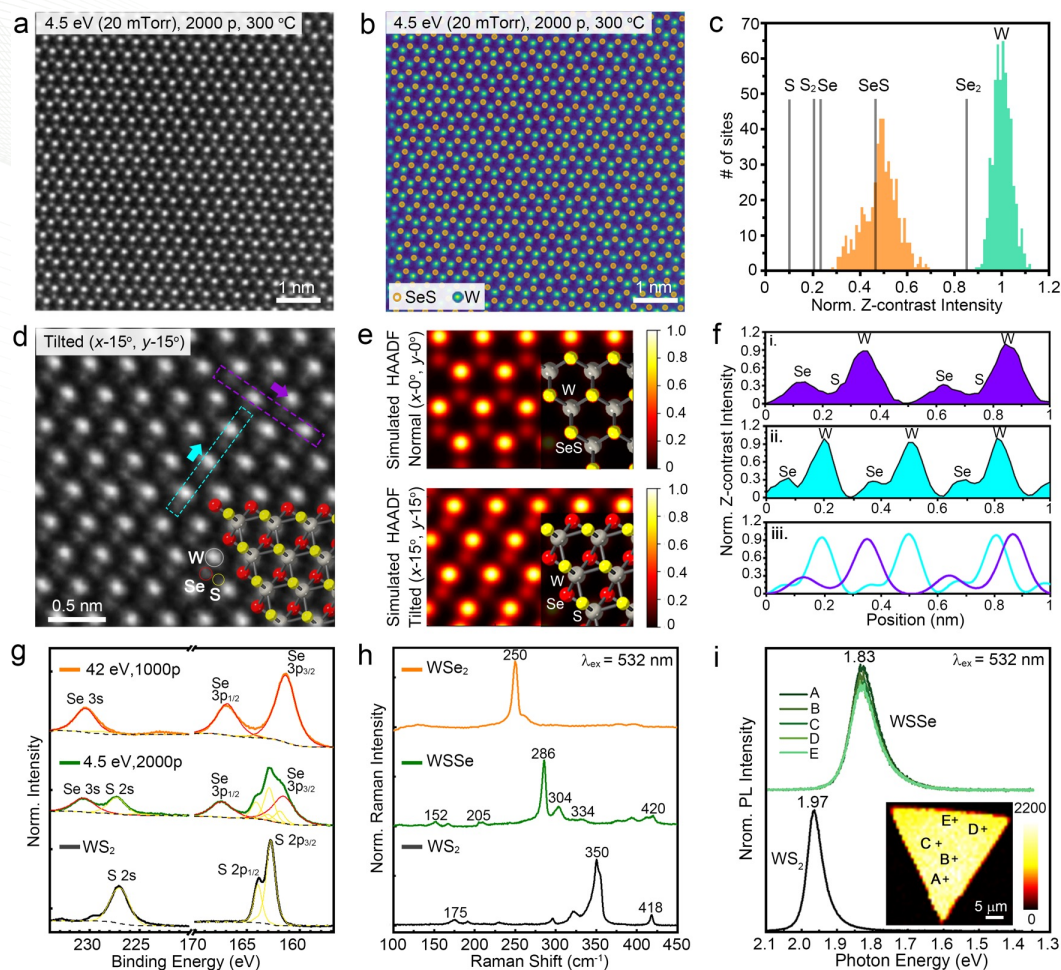# Exploring the unique advantages of laser plasmas for doping 2D materials
– *Submonolayer implantation of WS$_2$ to form Janus WSSe monolayers*

- Raman spectra, photoluminescence, and structure/composition compared after irradiation at different KE

- KE regimes found for:
  - Soft-landing (no damage)
  - Half conversion (Janus ?)
  - Full conversion

A narrow window of 3-5 eV/atom effectively selenizes only the topmost S atoms in WS$_2$ to form Janus WSSe

Monolayer WS$_2$

Full conversion WSe$_2$

Janus WSeS

Y. C. Lin, C. Liu, et al., **Low Energy Implantation into Transition-Metal Dichalcogenide Monolayers to Form Janus Structures** *ACS Nano* **14**, 3896-3906 (2020)

Janus WSSe monolayer converted from WS$_2$ by PLD at 4.5 eV/Se atom

- Atomic-resolution Z-STEM imaging analysis shows uniform columns of Se-S

- Tilting the sample allows the Se atoms to be distinguished from the S atoms, showing the perfect Janus structure

- XPS confirms the 1:1 ratio of S:Se

- Raman confirms the Janus modes

- Photoluminescence is strong and uniform over large areas

- Conversion works on supported samples

Kinetic energy dependent Se-S exchange on 1L WS_2 – DFT calculations and MD simulations

Our DFT calculations[1,2] (M. Yoon)

(a) ~3.35 eV to remove a S on the top of WS_2.

(b) ~9 eV to diffuse Se from top to bottom of WS_2 monolayer

This explains our ability to create Janus monolayers, and is consistent with the second, higher threshold to selenize both top and bottom layers.

Also see
1. Komsa, et al., *PRL*, **109**, 035503 (2012).
2. Li, et al., *ACS Nano* **12**, 4853 (2018).

4 eV per atom
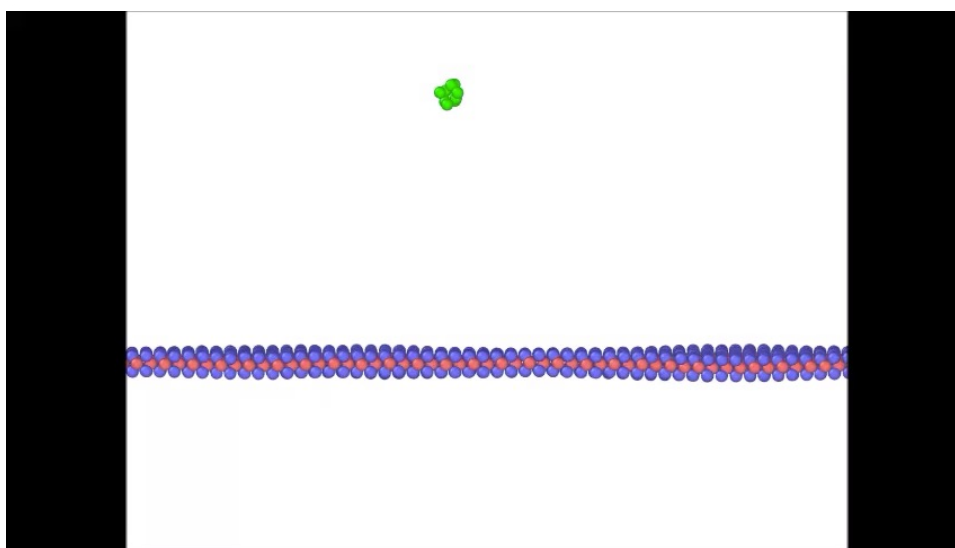
MD Simulations by
Eva Zarkadoula, ORNL

LAMMPs code
Stillinger-Weber potential
+ ZBL potential
(for very short distances)
T = 300K
Relaxed 300ps
Runtime 50 ps

Raman spectra, photoluminescence, and Z-STEM analysis indicate thresholds for top and bottom-layer S replacement in WS_2 monolayers consistent with theoretical energy thresholds

Kinetic energy dependent Se-S exchange on 1L WS$_2$ – DFT calculations and MD simulations

Our DFT c

(a) ~3.3

(b) ~9 eV

This expla

G: Alignment-of-Recording-of-SuperScan-HAADF_2019-09-06T163759.547101_8x512x512_2
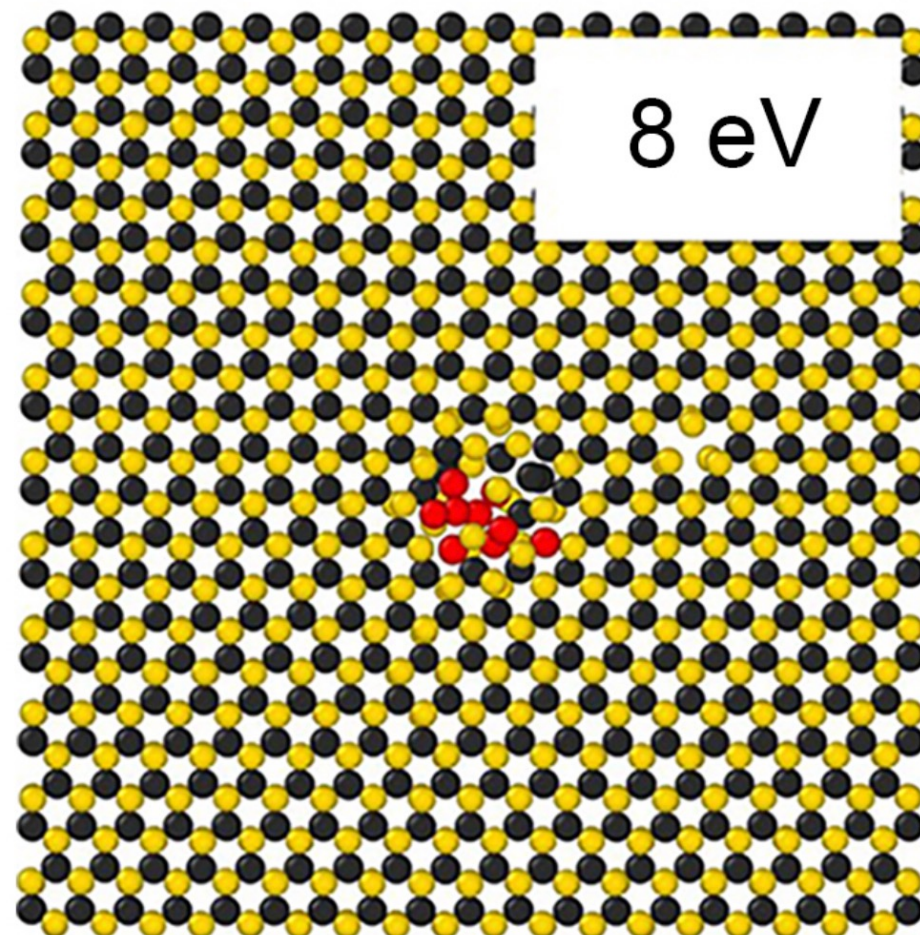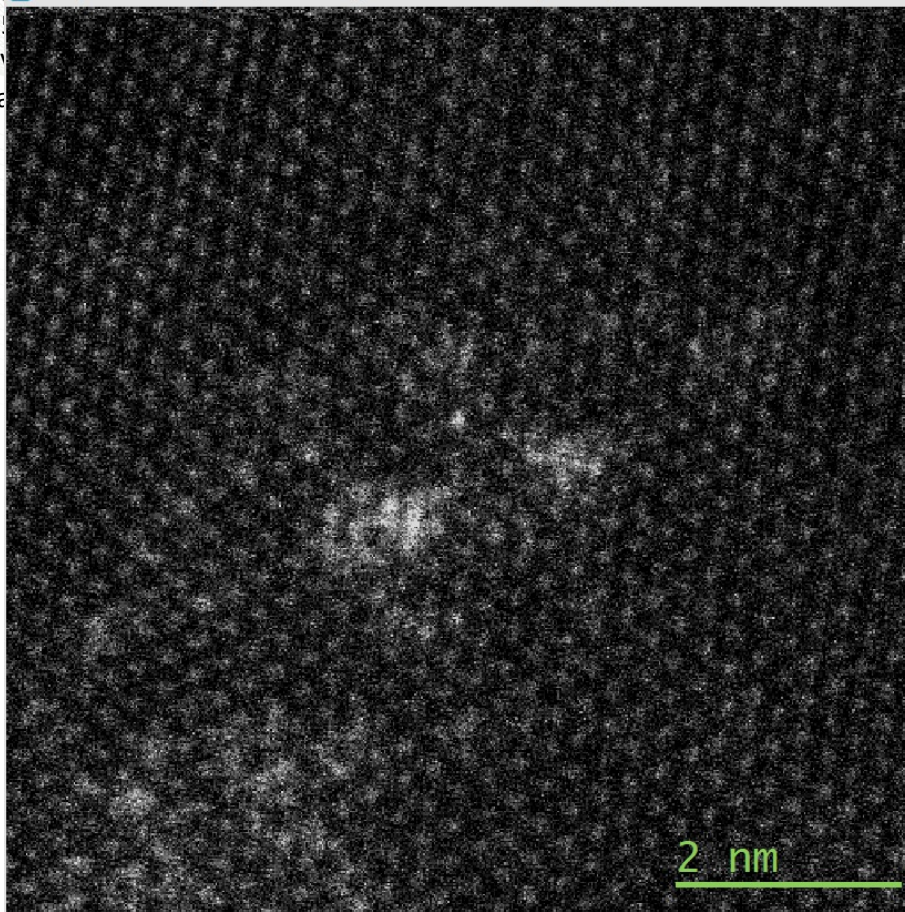
2 nm

8 eV

Y. C. Lin, C. Liu, et al., **Low Energy Implantation into Transition-Metal Dichalcogenide Monolayers to Form Janus Structures** *ACS Nano* **14**, 3896-3906 (2020)

SLIMS

Kinetic energy dependent Se-S exchange on 1L WS$_2$ – DFT calculations and MD simulations

Our DFT calculations[1,2] (M. Yoon)

(a) ~3.35 eV to remove a S on the top of WS$_2$.

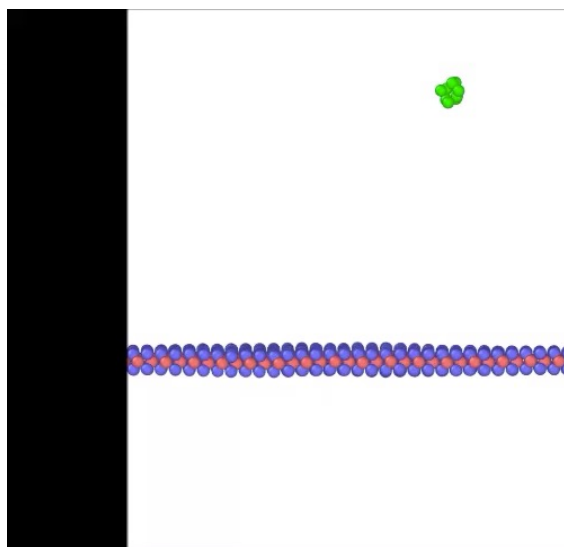(b) ~9 eV to diffuse Se from top to bottom of WS$_2$ monolayer

This explains our ability to create Janus monolayers, and is consistent with the seco
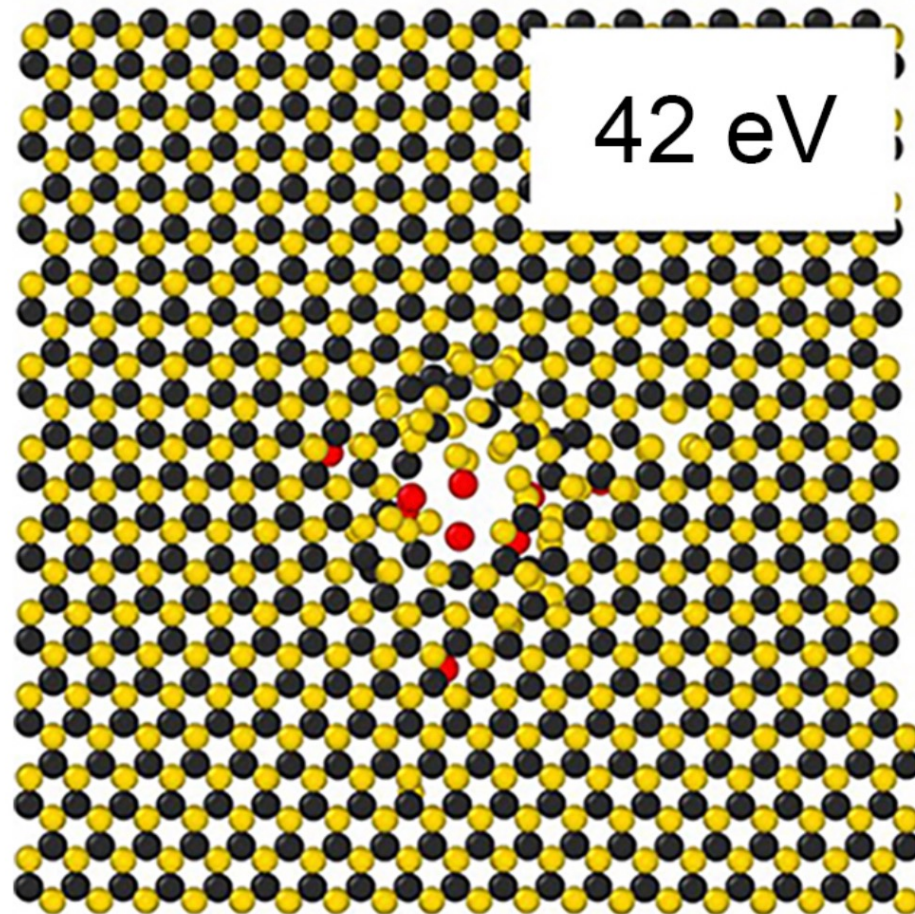
Als

1.

2.

16 eV per atom

42 eV

Raman spectra, photoluminescence, and Z-STEM analysis
replacement in WS$_2$ monolayers consistent

Y. C. Lin, C. Liu, et al., **Low Energy Implantation into Transition-Metal Dichalcogenide Monolayers to Form Janus Structures** *ACS Nano* **14**, 3896-3906 (2020)

Z-STEM of 1L WS$_2$ converted on TEM grids

c — 4.5 eV (20 mTorr), 800 pulses, 200 °C

Legend: S$_2$, SeS

d — 8 eV (5 mTorr), 30 pulses, 200 °C

Legend: S$_2$, SeS, Se$_2$, Se$_W$, Vac$_W$

e — 20 eV (HV), 600 pulses, 600 °C

Legend: S$_2$, SeS, Se$_2$

Y. C. Lin, C. Liu, et al., **Low Energy Implantation into Transition-Metal Dichalcogenide Monolayers to Form Janus Structures** *ACS Nano* **14**, 3896-3906 (2020)
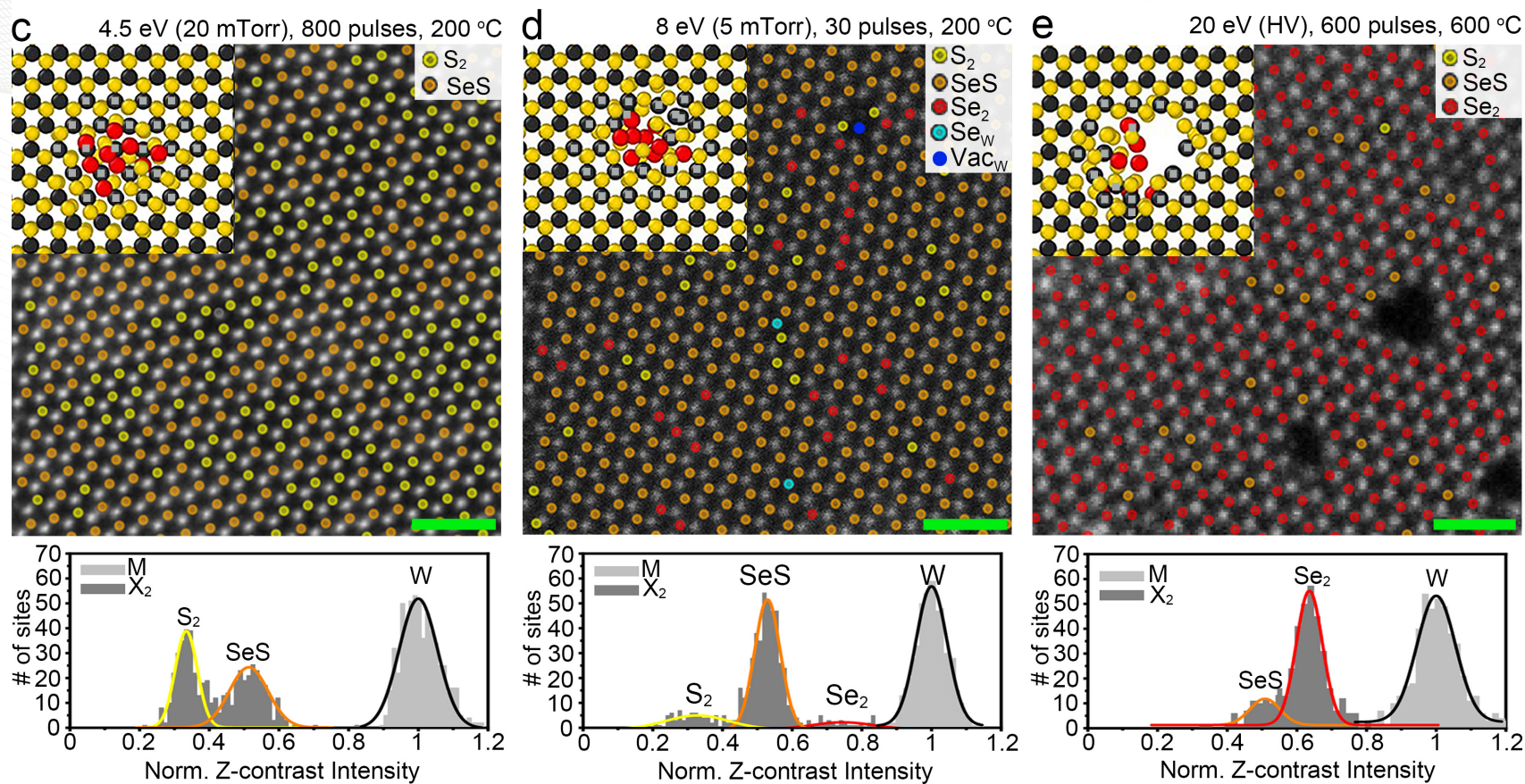
Enabling Auto-PLD – Autonomous PLD – Coupling *in situ* diagnostics with AI/ML decision making and high throughput techniques

Chamber schematic
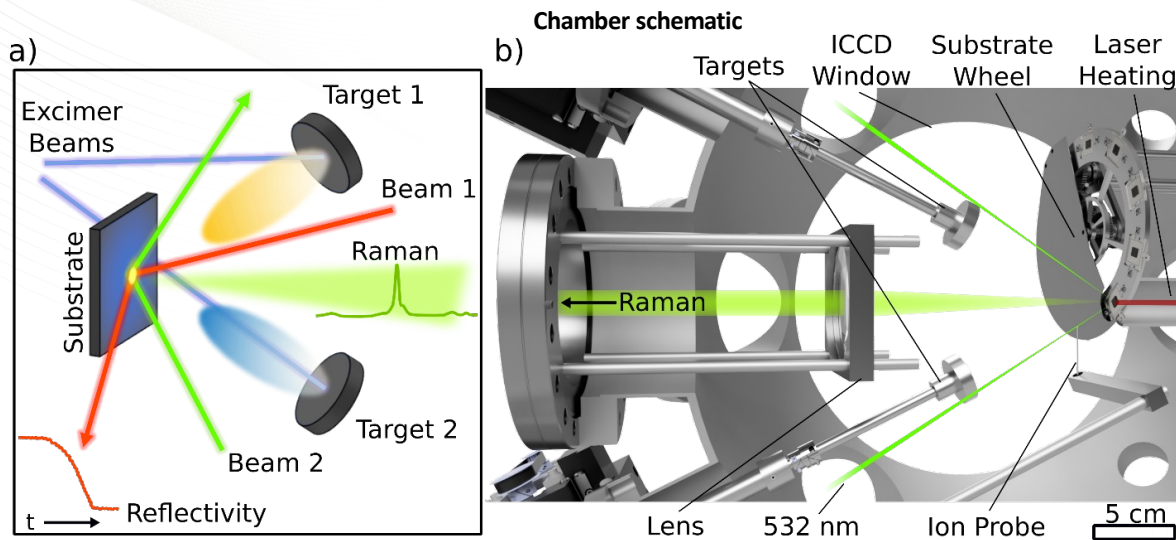
Sumner B. Harris, et al., *Small Methods*
https://doi.org/10.1002/smtd.202301763 (2024).

In situ film diagnostics

- Reflectivity (for film thickness)
- Raman (structure / quality)

In situ processing parameters

- Pressure, Temperature,
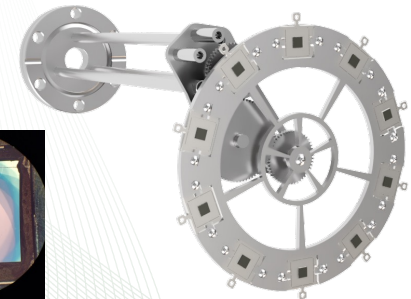- KE and fluxes from 2 targets
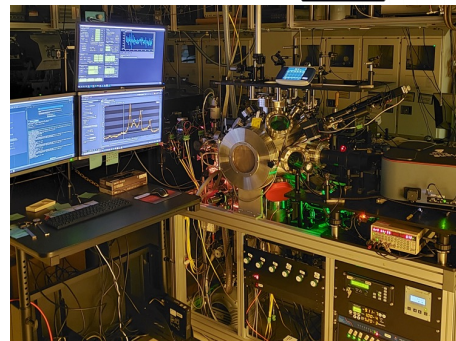
In situ plasma dynamics

- Gated imaging, ion probe, spectroscopy

High throughput techniques
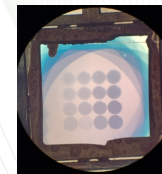
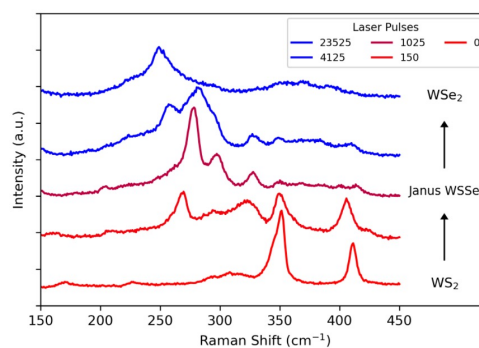*Laser crystallization 50X*

Sample wheel 10X

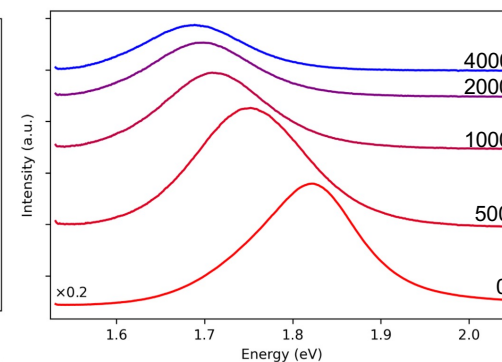# Diagnostics enabling AI/ML driven synthesis

Ion probe
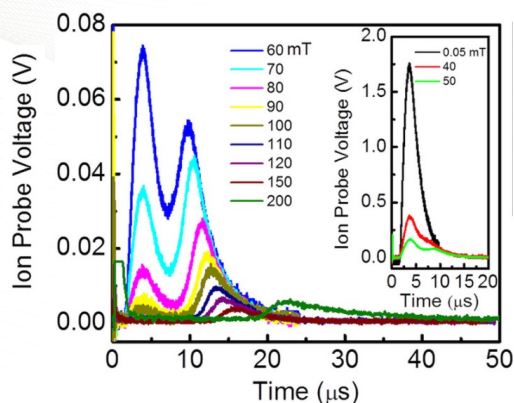
Ion probe measurements to determine plume
kinetic energy and structure
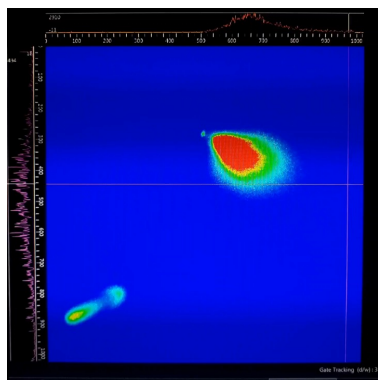M. Mahjouri-Samani, et al., Nano Lett. **17**, 4624–4633 (2017)

Raman

In situ Raman/PL reveals structural and stoichiometric information
for $WS_2 \rightarrow$ Janus WSSe $\rightarrow WSe_2$ conversion.
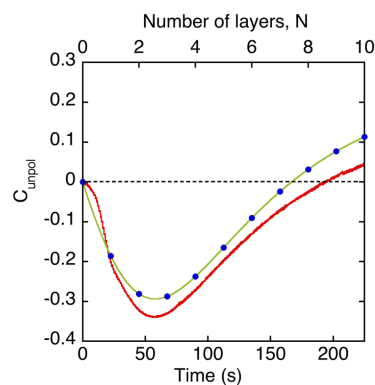
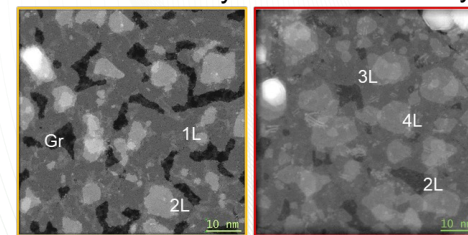**Photoluminescence**

ICCD plume photography

Co-deposition of $PdSe_2$ and Se

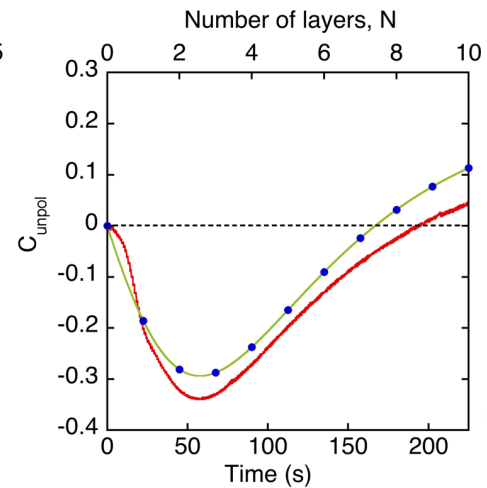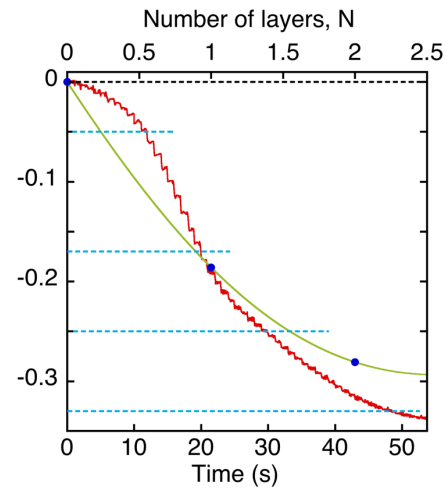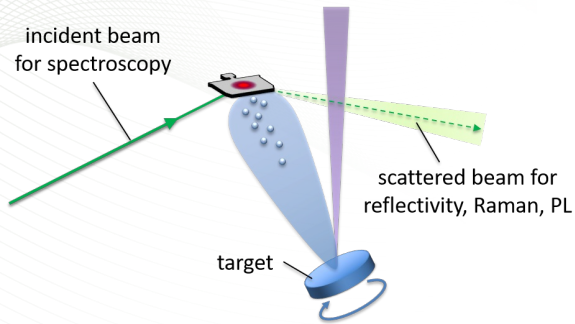**Optical Reflectivity**

17% Δ reflectivity   *33% Δ reflectivity*

Laser reflectivity for thickness and kinetics for $MoSe_2$
A. Puretzky, et al., 2D Mater. **7**, 025048 (2020)

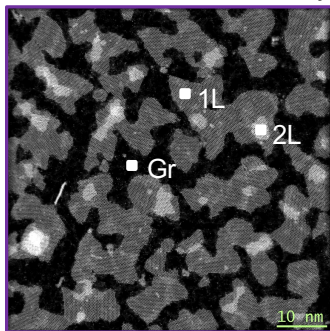# *In situ* diagnostics of MoSe$_2$ growth in PLD with TRR

incident beam for spectroscopy

scattered beam for reflectivity, Raman, PL

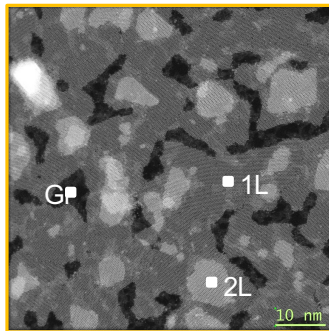target

Number of layers, N

Time (s)

C$_{unpol}$

- Detects nucleation and growth kinetics

- Deposition monitored on SiO$_2$/Si substrates

- Modeling predicts reflectivity changes

- Compared with films grown directly on graphene TEM grids

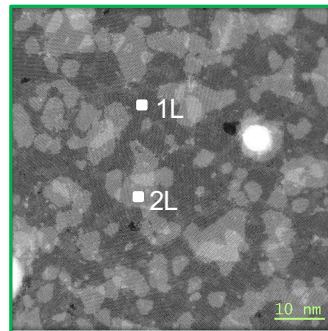- Excellent agreement between predicted reflectivity and layer number
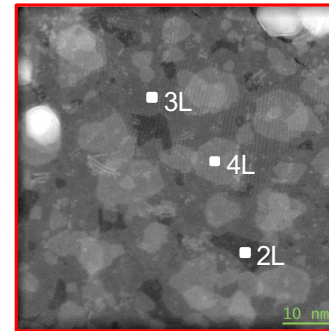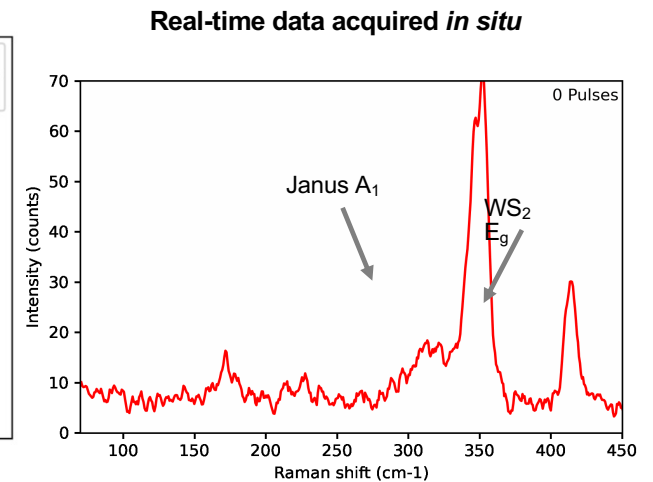
5% Δ reflectivity

1L
2L
Gr
10 nm

17% Δ reflectivity

Gr
1L
2L
10 nm

25% Δ reflectivity

1L
2L
10 nm

33% Δ reflectivity

3L
4L
2L
10 nm

A. Puretzky, et al., 2D Mater. **7**, 025048 (2020*)*

In situ Raman map of $WS_2 \rightarrow WSSe \rightarrow WSe_2$ by PLD of Se
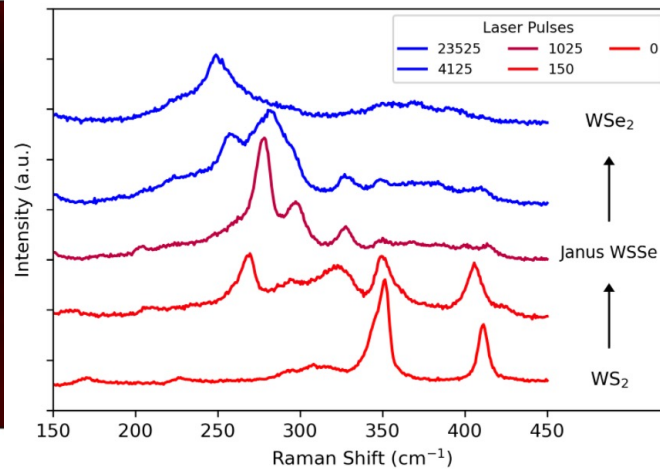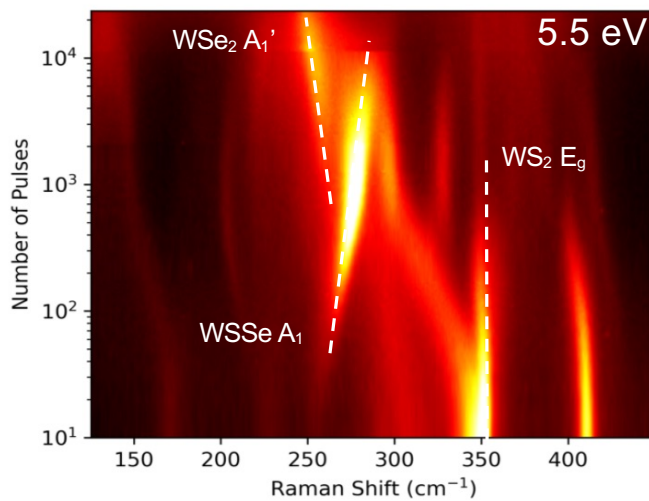
Evolution of Raman spectrum with number of laser pulses at 450°C. WS_2 first converts to Janus WSSe and then continues to WSe_2. Janus WSSe appears as an intermediate state between WS_2 and WSe_2. The mode frequencies shift with as the composition of each layer changes.

Conversion of WS$_2$ monolayers to Janus WSSe – 5.5 eV

- Raman intensity reveals both structure and a **layer-by-layer** conversion mechanism

- *Fractional* Janus TMD's: incomplete layer substitution forms single-sided alloy

Harris et al., *ACS Nano* 17(3), 2472 (**2023**).
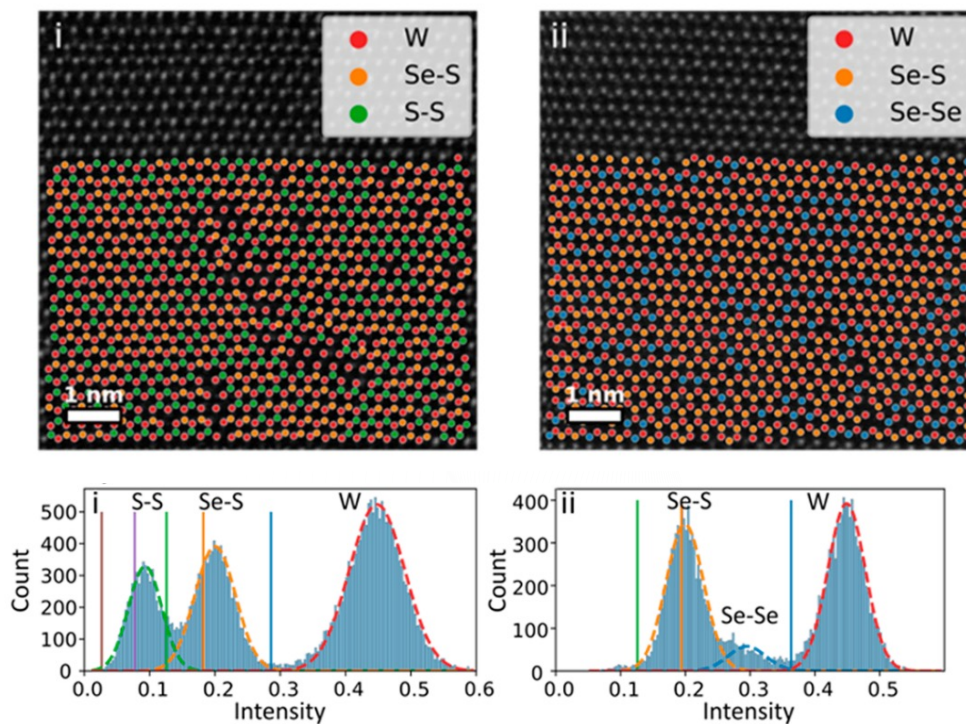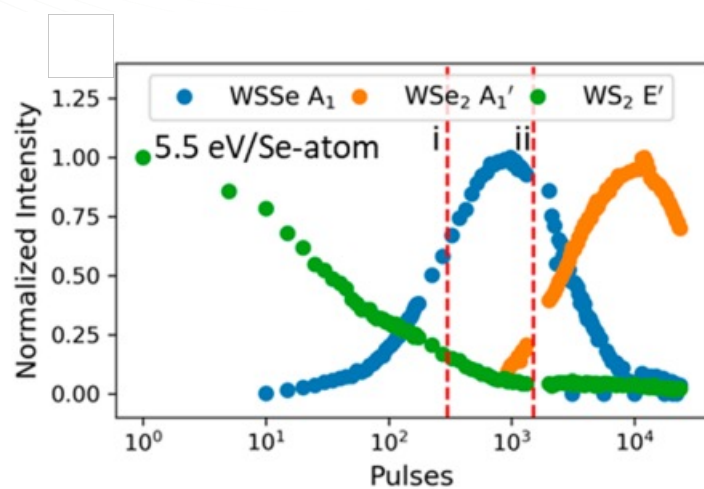
Autonomous Synthesis of Thin Film Materials with Pulsed Laser Deposition Enabled by In Situ Spectroscopy and Automation

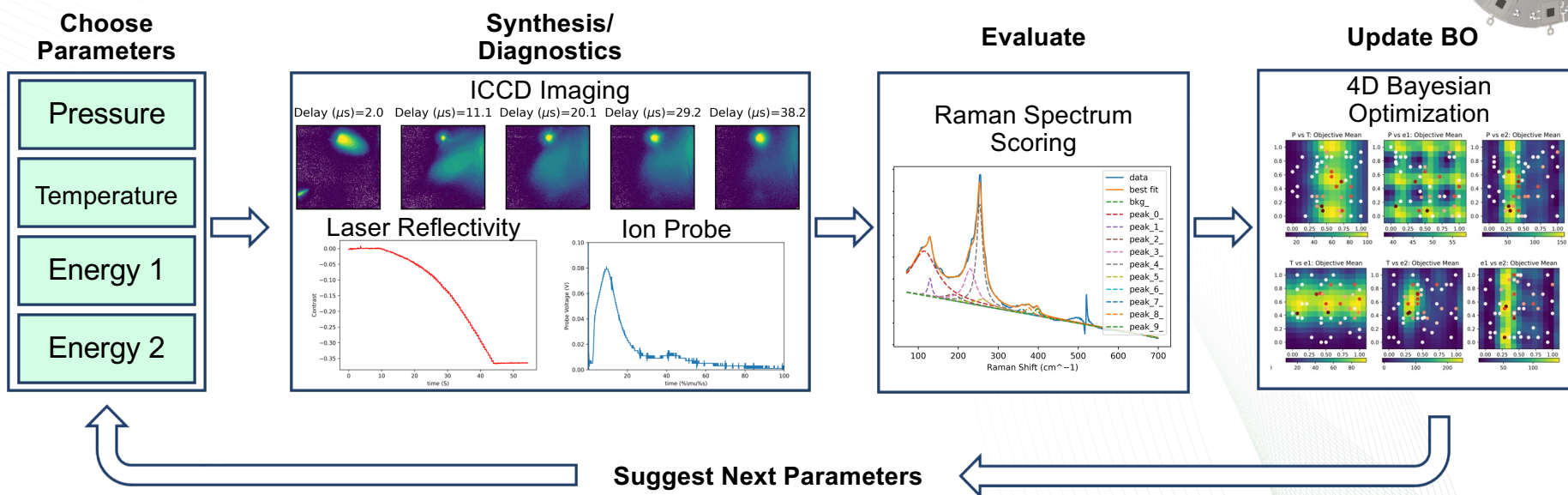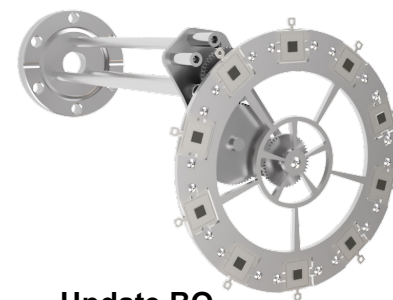**Goal: Autonomously search a broad parameter space to identify good growth conditions for ultrathin (<3 monolayers) WSe$_2$ by PLD.**

Choose Parameters

Pressure

Temperature

Energy 1

Energy 2

Synthesis/ Diagnostics

ICCD Imaging

Delay (μs)=2.0 Delay (μs)=11.1 Delay (μs)=20.1 Delay (μs)=29.2 Delay (μs)=38.2

Laser Reflectivity

Ion Probe

Evaluate

Raman Spectrum Scoring

Update BO

4D Bayesian Optimization

Suggest Next Parameters

Sumner B. Harris, et al., *Small Methods* https://doi.org/10.1002/smtd.202301763 (2024).
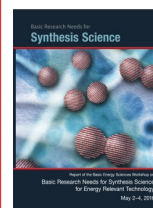
Summary – *in situ* diagnostics enable the controlled laser synthesis of nanomaterials

- Take-home messages

  - Laser ablation naturally provides kinetic energy and different 'building blocks' which can be tuned by background gas confinement for self-assembly in the vapor or on the substrate. (Ex: nanotubes, nanorods, nanohorns, 2D crystal flakes vs. t, T)

  - Plume splitting is important, and ion probes easily measure TOF and flux to the substrate. Background gas collisions can remove the high-KE component (Beer's Law), (e.g., > 20 eV/atom species) is especially important for 2D material growth (implantation at 3-5 eV/atom).

  - 'Nanoparticle PLD' of amorphous nanoparticles is especially important to explore post-processing to achieve different phases by "Crystallization by Particle Attachment".

  - Simple optical diagnostics of the film (optical reflectivity, Raman spectroscopy, PL) during PLD allow deposition rate and phases to be determined in real-time, enabling precision synthesis of quantum materials like Janus monolayers by PLD.

  - Automation, machine learning, and AI can be successfully applied to PLD and laser processing to correlate in situ diagnostics with models.

Processing parameters:
- Pressure, temp.
- Fluence, KE
- Flux, rep. rate
- Pulse duration

Machine Learning Algorithm

In situ diagnostics

Synthesis and Processing

Feedback parameters:
- Raman, Difraction (structure)
- PL (property)
- Reflectivity (kinetics)
- EELS (stoichiometry)
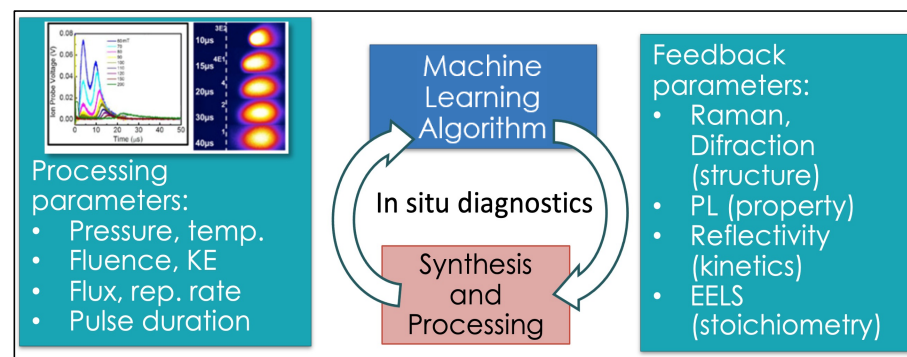
Motivated by U.S. DOE - BES Priority Research directions:

"Integrate emerging theoretical, computational, and in situ characterization tools to achieve directed synthesis with real-time adaptive control"
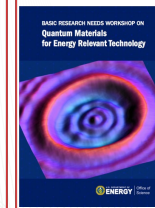
"Design revolutionary tools to accelerate discovery and technological deployment of quantum materials"